Exploring Standard Model Extension Through Neutrinos

Nishat Fiza

A thesis submitted for the partial fulfilment

of

the degree of Doctor of Philosophy

Department of Physical Sciences

Indian Institute of Science Education and Research, Mohali

Knowledge city, Sector 81, SAS Nagar, Manauli PO, Mohali 140306, Punjab, India.

May, 2023

Dedication

My family

Declaration

The work presented in this thesis has been carried out by me under the guidance of Dr. Satyajit Jena at the Indian Institute of Science Education and Research Mohali. This work has not been submitted in part or in full for a degree, a diploma, or a fellowship to any other university or institute. Whenever contributions of others are involved, every effort is made to indicate this clearly, with due acknowledgement of collaborative research and discussions. This thesis is a bona fide record of original work done by me and all sources listed within have been detailed in the bibliography.

Nishat Fiza

In my capacity as the supervisor of the candidate's thesis work, I certify that the above statements by the candidate are true to the best of my knowledge.

Dr. Satyajit Jena

Publications

Nishat Fiza

Published

1. **Exploring the new physics phases in 3+1 scenario in neutrino oscillation experiments.**
   Nishat Fiza, Mehedi Masud, Manimala Mitra.
   JHEP 09 (2021) 162.

2. **Investigating Lorentz Violation with the long baseline experiment P2O.**
   Nishat Fiza, Nafis Rezwan Khan Chowdhury, Mehedi Masud.
   JHEP 01 (2023) 076.

3. **Measurement of $\bar{\nu_\mu}$ charged-current single π^- production on hydrocarbon in the few-GeV region using MINERvA.**
   MINERvA Collaboration. T. le et al.
   DOI: 10.1103/PhysRevD.100.052008

4. **Tuning the GENIE Pion Production Model with MINERvA Data.**
   MINERvA Collaboration. P. Stowell et al.
   DOI: 10.1103/PhysRevD.100.072005

Proceedings

1. **Probing the CP phases in 3+1 scenario at LBL experiments**
   Nishat Fiza, Mehedi Masud, Manimala Mitra
   XXIV DAE-BRNS HEP Symposium

Poster

1. **Investigating the new physics scenario in P2O experiment.**
   Nishat Fiza, Nafis Rezwan Khan Chowdhury, Mehedi Masud
   WIN 2021, Online (hosted by University of Minnesota, USA).

Abstract

Neutrino physics offers us the scope to investigate the physics Beyond Standard Model (BSM). The first and foremost signature of the non-zero mass of neutrinos is given by the theory of neutrino oscillation which has now been established by several pioneering experiments. Extensive studies have been done to understand the phenomenon of neutrino oscillation. There still lie unresolved issues in the domain of neutrino oscillation. In the current thesis, we have addressed a few issues in the context of long-baseline (LBL) neutrino oscillation experiments.

Various global analyses successfully establish the phenomenon of 3-neutrino oscillation (electron, muon, and tau neutrino). However, a few short-baseline anomalies (LSND and MiniBooNE) indicate the existence of a fourth sterile neutrino (mass of the order of eV). Should the fourth neutrino exist in nature, we have investigated how the oscillation parameters, specifically the CP phases, can be bound in case of the ongoing and forthcoming LBL data from DUNE, NOvA, T2K, and T2HK. We have also studied how the parameter space of neutrino-less double-beta decay gets modified due to the inclusion of the sterile neutrino in the oscillation picture. Next, we have focused on one of the neutrino mass generation models, i.e., the left-right symmetric model (LRSM). We have used published data from the ongoing experiments NOvA and T2K to probe the LRSM parameter space in terms of the NSI parameters and explore if we can put a constraint on the lowest neutrino mass. The phenomenon of Lorentz invariance violation (LIV) has also been studied in the context of upcoming LBL experiments P2O and DUNE. The Planck suppressed effect of LIV can be demonstrated in the long-baseline neutrino oscillation data, and that in turn can give us an idea of the bounds on the relevant parameter space. We have done a chi-squared analysis to study the LIV parameters. We have focused on the charged pion production channel and studied how the precision of the measurement can be improved for low-energy pions in MINERvA experimental setups. We will discuss the outcomes of thesis works based on the above proposals.

ACKNOWLEDGMENTS

It is said that writing the acknowledgment is more challenging than writing the thesis itself. Because there is always a risk of omission which can lead to friendly misunderstandings! So, accepting my inability to remember names and instances, I would like to thank all the people I have encountered during this remarkable phase of my life.

First and foremost, I owe a very special gratitude to my thesis advisor Dr. Satyajit Jena who has continued to be an excellent teacher, academically and non-academically, throughout this significant journey of my life. I am indebted to Dr. Jena in a great many ways.

It gives me immense pleasure to thank my collaborators. I would like to give a very special thanks to Dr. Manimala Mitra for all the collaborative work, support, and frequent and fruitful discussions that immensely helped me learn the nitty-gritty of neutrino physics. I will always be grateful to Dr. Ambresh Shivaji for his constant support, endless discussions on physics research, the collaborative work, and also for giving me a chance to mentor a few MS project students which in turn has become a learning opportunity for me. I want to thank Dr. Anushree Ghosh for always providing me with anecdotes about computer programming and the understanding of neutrino physics phenomenology. I must express my deepest gratitude to Prof. Laura Fields, Prof. Kevin McFarland, Prof. Deborah Harris, Prof. Jorge Morfin, and Dr. Deepika Jena for providing me with a learning experience at the MINERvA collaboration.

I would like to thank the members of my thesis committee Dr. Kinjalk Lochan, Dr. Ketan Patel, and Prof. Charanjit Singh Aulakh for motivating me at each stage of this research experience. I sincerely express my gratitude to Dr. Mandeep Sigh, Dr. Sanjeev Kumar, and Prof. Sudeshna Sinha for the excellent teaching and discussions. I am also thankful to Dr. Vishal Bhardwaj, Dr. Harvinder Kaur Jassal, Prof. Jasjeet Singh Bagla, and Dr. Abhishek Chowdhury for the long and patient discussions. I am thankful to Dr. Ritajyoti Bandyopdhyay, Dr. Vaibhav Vaish, Sandipa Baidya, and Dr. Neeraja Sahasrabudhe for substantial discussions on philosophy and mathematics.

Next, the turn for the IISER Mohali campus, where I spent one of the most beautiful times of my life and which thus has become a "Home away from home" for me during the past six years. My wholehearted thanks go to Rohit, Ranbir, and Jasleen for getting me through every possible situation in research and outside! Thanks to Subhadip da,

Ramyani di, Moutushi di, Anweshika, Debapriya (Gupta), Shreyan, Amartya, Rudranil, Mayukh, Mihir, Vineet, Suchetana, Soumya (Pynacha) for making me realize that age is just a number when it comes to friendship. I want to thank Nafis, Vishnu, Manali, Aditi, Triparna, and Aradhita for always being there for me even though we didn't get a chance to meet very often. I want to thank Soumya (Dutta), Debapriya (Das), Shubhra da, Juhi, Sourav, Akash, Swati, Aman, Ashish (Meena), and Suman for enriching my experience at the campus. Now, coming to my lab, which I have experienced being formed from scratch. Here comes a long list of my lab-mates to whom I am thankful for providing me with a healthy working environment and an even more delightful break time over the years: Anjali (Krishnan), Shahina, Tasha, Akhil, Ashish (Moharana), Anjaly (Menon), Neeraj, Shubham, Nilotpal, Vassu, Ojaswi, Paras, Rutik, Deesha, Debanjan, Sveekruth, Sourabh, Bidisha, Deya, Monit, Ivan, Asrith, Aman, Yogesh, Shubhangi, Saurav, Kartik, Kiran di (Dr. Kirandeep Kaur), Bharat, and Supriya. I want to mention the non-academic workers of the campus in this acknowledgment section for considering me their friend and showering me with motherly love in spite of the language barrier. I am also thankful for a huge amount of fiction literature, music, movies, games of badminton, drawings, and paintings that kept me afloat and helped me move through this sometimes difficult journey!

I am grateful to the IISER Mohali library and computer center for providing me with all the necessary tools and references.

Last but not the least, I am forever grateful to my family, especially my partner, Masud for enduring me through the duration of my Ph.D.

Contents

List of Figures

List of Tables

Chapter 1

Introduction

1.1 History of neutrinos

In 1914, Chadwick demonstrated that the β-spectrum was continuous, in contrast to α- and γ-rays which were unique in energy. This led to a doubt regarding the principle of conservation of energy. Meitner later demonstrated that the missing energy could not be ascribed to neutral γ-rays, which led to the idea that the missing energy could be explained by the existence of a new particle. Also, in the case of beta decay the mass number remains unchanged, so, the change in nuclear spin should have been integer. But the electron is a spin-half particle and the question of unaccounted spin arise. In order to propose a solution to the missing-energy problem and also as a remedy to the problem of spin-statistics in β-decay, Wolfgang Pauli presented in his open letter, the idea of the existence of a neutral weakly interacting fermion emitted in β-decay. Thus the history of the neutrinos started with this famous letter by Pauli on 4th December, 1930 [1], addressed to *"Dear Radioactive Ladies and Gentlemen"*! The term *neutrino* was coined later by Enrico Fermi [2]. Later Fermi expanded upon his idea to publish a famous theory on β-decay [3, 4], known as the *Fermi theory*. In the weak interaction according to Fermi, neutrons decay to protons via a non-renormalizable four-fermion interaction, $n \rightarrow p + e^- + \bar{\nu}$ where $\bar{\nu}$ is the electron antineutrino. Fermi's theory predicts that the inverse reaction $p + \bar{\nu} \rightarrow n + e^+$ occurs with the same interaction strength and it could be used to observe neutrino scattering in real life. Fermi's theory was later expanded by Gamow and Teller in 1936 [5] to include axial-vector currents in a way that parity was still conserved since the concept of parity violation was unthinkable at that time. It was later realized that other couplings such as scalar, pseudoscalar, and tensor couplings could also participate in weak interactions. After the discovery of muons, the observation of

muon decay led Pontecorvo to propose in 1947 the universality of Fermi interactions of electrons and muons [6].

Despite of the remarkable success of the Fermi Theory, the neutrino was yet to be observed in experiments, partly due to the very weak strength of interactions as predicted by Bethe and Peierls in1934 when they claimed that it might never be observed [7]. Urged, in particular by Pontecorvo in the early 1950s, Reines and Cowan searched for a way to measure inverse beta decay, in which an antineutrino can produce a positron. After considering several methods, including a nuclear explosion, they settled on using the large flux of antineutrinos from a nuclear reactor and 10 tons of equipment, including 1400 litres of liquid scintillators. This experiment was the first reactor-neutrino experiment and neutrino was observed in 1956 for the first time in history [8]. Reines was awarded the Nobel prize in 1995 for this breakthrough.

In 1956, Lee and Yang interpreted the decays of two species of neutral kaons observed in experiments at BNL as a breakdown of the law of parity (P) conservation (invariance under spatial inversion) [9]. Shortly thereafter, C. S. Wu and colleagues carried out an experiment on the radioactive beta decays of polarized ^{60}Co that confirmed parity violation [10]. This further complicated the situation because parity-violating couplings were now allowed in weak lagrangian. This was immensely simplified in the form of V-A theory, put forward by Feynman & Gell-Mann [11]; Sudarshan & Marshak [12]; and Sakurai [13]. This could easily be incorporated into the lepton sector by using the two-component theory of a massless neutrino, proposed in 1957 by Landau [14], Lee and Yang [15] and Salam [16]. In this theory, neutrinos are left-handed and antineutrinos are right-handed, leading automatically to the V-A couplings. In 1958, Goldhaber, Grodzins and Sunyar [17] measured the polarization of a neutrino in the electron capture $e^- + {}^{152}Eu \rightarrow {}^{152}Sm^* + \nu_e$ and found that the polarization of ν_e was indeed in a direction opposite to its motion, within experimental uncertainties, in agreement with the two-component theory of a massless neutrino.

A new era of neutrino physics began when a second, different kind of neutrino, the muon neutrino (ν_μ) was discovered in 1962 by Lederman, Schwartz and Steinberger [18] in the first-ever accelerator neutrino experiment. This experiment, which utilized an enormous amount of iron shielding plates cut out of the battleship USS Missouri, marked the first serious accelerator neutrino experiment. In 1957 Pontecorvo first conceptualized [19, 20] the possibility of neutrino oscillations by generalizing the notions related to kaon mixing. As only one flavour of neutrino had been discovered at that time, Pontecorvo's hypothesis focused on mixing between ν and $\bar{\nu}$. In 1962, with the knowledge

that multiple flavours of neutrinos existed in nature, Maki, Nakagawa, and Sakata proposed oscillations between ν_e and ν_μ [21]. However, there was only a vague hint of the present understanding of neutrino oscillations in their work. In 1967, Pontecorvo presented the first intuitive understanding of two-neutrino mixing and oscillations [22], which was later completed by Gribov and Pontecorvo in 1969 [23]. The theory of neutrino oscillations was finally developed in 1975-76 by Eliezer and Swift [24], Fritzsch and Minkowski [25], S.M. Bilenky and B. Pontecorvo [26]. This framework was later extended to tau neutrino (ν_τ), which was detected later in 2000 by the direct observation of the Nu-Tau (DONuT) collaboration [27].

In 1967, the Homestake experiment, pioneered by Davis and Bahcall uncovered the first indication that supported the neutrino oscillation theory. They sought to measure the rate at which solar neutrinos were captured by chlorine nuclei. They had observed a deficit between the measurement and the prediction of solar neutrinos, but the source of the discrepancy remained unclear. Many pointed toward an inadequate understanding of the solar model or errors in the neutrino experiments. The deficit phenomenon, however, was not limited to solar neutrino observations. Atmospheric neutrino experiments also reported a deviation from the approximately 2:1 ratio between muon and electron neutrinos that were produced through the $\pi \rightarrow \mu\nu_\mu, \mu \rightarrow e\nu_e\nu_\mu$. IMB [28] experiment, MACRO [29], and Kamiokande collaboration [30] found significant deficits in ν_μ disappearance fluxes. In 1998, Super- Kamiokande [31, 32] explained the shortfall by fitting their results with non ν_e flavor oscillation framework. The debate in the solar neutrino sector ended in 2001 when the Sudbury Neutrino Observatory (SNO) [33] experiment provided conclusive evidence that roughly two-thirds of the solar neutrino flux was related to non ν_e flavours. This result supported the notion of neutrino oscillations and reconciled the total flux measurement with the standard solar model (SSM) prediction. by the Mikheyev-Smirnov-Wolfenstein (MSW) resonance conversion effects [34, 35]. The confirmation of the phenomenon of neutrino oscillation by Super-Kamiokande and SNO has been honoured by awarding the Nobel Prize in Physics in 2015 [36].

1.2 Neutrino mass and its motivation

The search for the invisible width of the Z boson in the Large Electron Positron (LEP) Collider has given the experimental value of neutrinos to be $N_\nu = 2.984 \pm 0.008$ [37]. This value provides a bound to the expected number of light active neutrinos to be 3. Any extra neutrino, if indeed present, must thus be sterile in nature. The discovery of

neutrino oscillation establishes that neutrinos indeed have mass. The origin of the mass of the neutrinos is still under debate. A plausible explanation can be seesaw mechanism that requires the presence of heavy right-handed sterile neutrinos. From the general construct of the standard model Lagrangian, it is implied that the chiral fields ν_L and ν_R (which are also allowed by SM symmetries) will contribute to the neutrino Lagrangian. We consider the case where we only have ν_L in our framework and neutrino is a Majorana particle. Then we can write the following mass term:

$$\mathcal{L}^{L}_{mass} = \frac{1}{2} m_L \nu_L^{\dagger} \mathcal{C}^{\dagger} \nu_L + h.c. \tag{1.1}$$

where m_L is the mass for left-handed neutrino and $\mathcal{C}$ is the charge conjugate operator. Now, if we consider the existence of ν_R in addition to ν_L we will be able to write a Dirac mass term, as well as another Majorana mass term, and the neutrino Lagrangian can be represented in the following form:

$$\begin{aligned} \mathcal{L}^{D+M}_{mass} &= \mathcal{L}^{D}_{mass} + \mathcal{L}^{L}_{mass} + \mathcal{L}^{R}_{mass} \\ &= -m_D \overline{\nu_R} \nu_L + \tfrac{1}{2} m_L \nu_L^{\dagger} \mathcal{C}^{\dagger} \nu_L + \tfrac{1}{2} m_R \nu_R^{\dagger} \mathcal{C}^{\dagger} \nu_R \end{aligned} \tag{1.2}$$

To understand the mass term more precisely it will be helpful to specify the left-handed chiral fields in the matrix form:

$$N_L = \begin{pmatrix} \nu_L \\ \nu_R^C \end{pmatrix} = \begin{pmatrix} \nu_L \\ \mathcal{C}\overline{\nu_R}^T \end{pmatrix} \tag{1.3}$$

The Dirac-Majorana mass term can be written in the following form:

$$\mathcal{L}^{D+M}_{mass} = \frac{1}{2} N_L^T \mathcal{C}^{\dagger} M N_L + h.c. \tag{1.4}$$

where the mass M can be represented in the matrix form:

$$M = \begin{pmatrix} m_L & m_D \\ m_D & m_R \end{pmatrix} \tag{1.5}$$

This expression leads us to a situation where definite mass for ν_L or ν_R can't be determined. But if we can diagonalise the mass matrix through a unitary transformation we may find the field of the massive neutrinos:

$$U^T M U = \begin{pmatrix} m_1 & 0 \\ 0 & m_2 \end{pmatrix} \tag{1.6}$$

where U is the unitary matrix.

If we consider the case where $m_D \ll m_R$ and $m_L = 0$ we will get the following values of the mass terms:

$$m_1 \simeq \frac{m_D^2}{m_R} \tag{1.7}$$

$$m_2 \simeq m_R \tag{1.8}$$

which implies that the neutrino mass state ν_2 is heavy but ν_1 is very light since $m_D \ll m_R$. This is the famous seesaw mechanism (known as Type-I seesaw in literature) [38,39],- the heaviness of the mass of $\nu_2(m_2 \simeq m_R)$ results in the lightness of the ν_1 mass.

Neutrino mass generation through seesaw mechanism is also a crucial component towards explaining another fundamental puzzle, - namely the observed baryon asymmetry in the universe. In 1967, Sakharov first proposed the three conditions necessary for baryogenesis that generates baryon asymmetry in the universe [40]. These include, a) Baryon number(B) violation b) C and CP violation, and c) departure from chemical equilibrium. Among the viable baryogenesis scenarios, the most elegant is leptogenesis [41]. The right-handed neutrino N that generates the seesaw mechanism discussed above, decays to lepton-higgs pair (lH) and its conjugate ($\bar{l}H^*$) with different branching ratios (Γ),- thereby violating B. The second Sakharov condition, namely CP violation, results from the leptonic CP phase δ originating from Yukawa coupling and neutrino mass matrix. Departure from Chemical equilibrium occurs due to the expansion of the universe. As a final result, the following leptonic asymmetry Y_L is generated [42]

$$Y_L \sim \frac{1}{g_*} \frac{\Gamma(N \to lH) - \Gamma(N \to \bar{l}H^*)}{\Gamma(N \to lH) + \Gamma(N \to \bar{l}H^*)}, \tag{1.9}$$

where g_* is the number of degrees of freedom. The lepton asymmetry is then partially converted to baryon asymmetry Y_B through a sphaleron process that preserves $B - L$ while violating B and L separately [43]. Although the viability of leptogenesis depends on various factors such as the right-handed neutrino mass, other variants of seesaw mechanism, flavour effects *etc.*, it is incredible that the neutrino sector offers ingredients to resolve such an elusive mystery of the universe.

1.3 Source of neutrinos and types of neutrino experiments

In this section, we will briefly discuss about various sources of the neutrinos used in the experiments.

- **Solar neutrinos:** According to the Standard Solar Model (SSM) developed by Bahcall *et. al.* [44–46], these are mainly produced through the following two groups of chain reactions inside the sun:

  1. *proton-proton chain:* An overview of this chain including the reactions that produce neutrinos is shown in Fig. 1.1. The three channels, namely *pp*, *hep*, ^8B produce continuous neutrino spectra (also see Fig. 1.3). Note that the production rate of *hep* neutrinos is expected to be even smaller (due to the tiny branching fraction of this channel) than the rare ^8B neutrinos. The *pep* neutrinos and the ^7Be neutrinos, on the other hand produce line spectra of neutrinos.

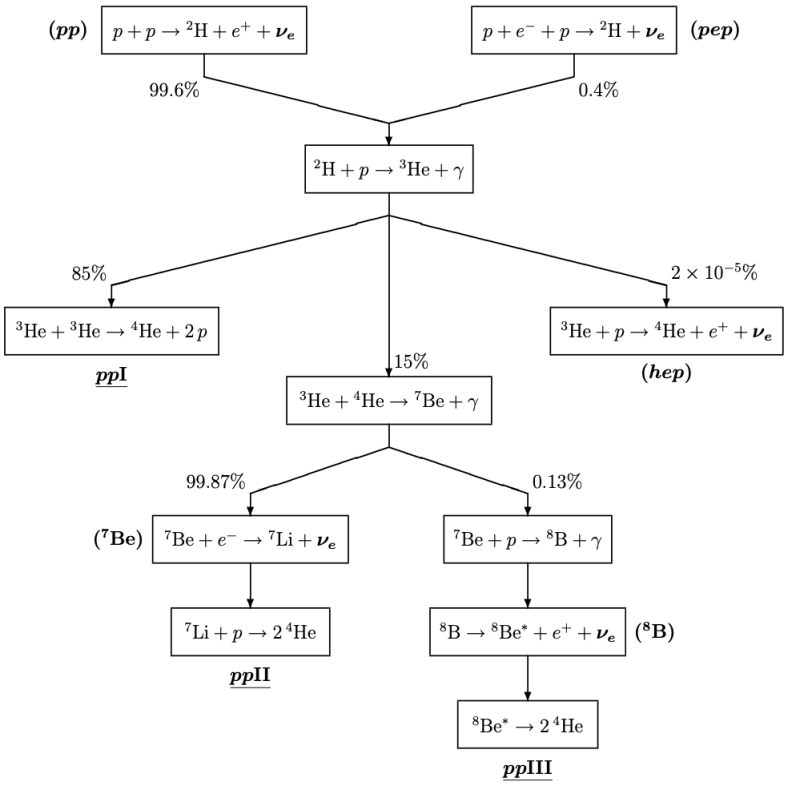

Figure 1.1: A schematic picture showing the proton-proton chain of solar neutrino production. The neutrino-producing reactions (along with corresponding branching ratios) and the familiar neutrino fluxes are mentioned in the parentheses. The main branches are shown as underlined labels. This figure is adopted from [47].

  2. *CNO cycle:* An overview of the CNO (Carbon-Nitrogen-Oxygen) cycle is shown schematically in Fig. 1.2. To summarise, the three most important re-

actions producing neutrinos in the CNO cycle are [48],

$$^{13}N \rightarrow {}^{13}C + e^{+} + \nu_e,$$
$$^{15}O \rightarrow {}^{15}N + e^{+} + \nu_e,$$
$$^{17}F \rightarrow {}^{17}O + e^{+} + \nu_e.$$

where the neutrinos have energy approximately in the range $0 - 2.7$ MeV.

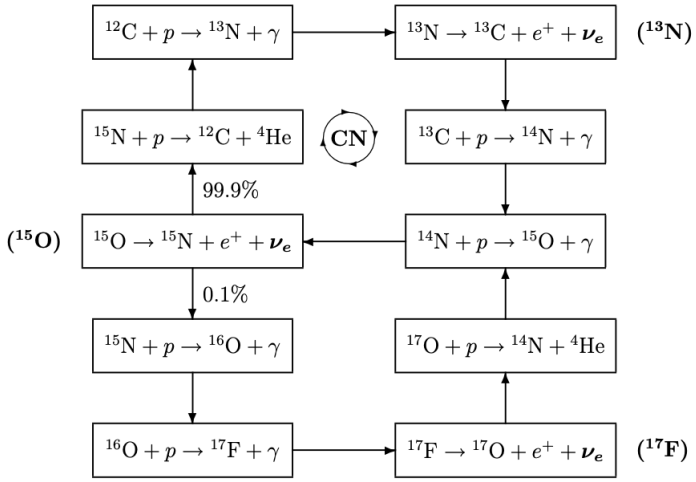

Figure 1.2: A schematic picture showing the CNO cycle of solar neutrino production. The neutrino-producing reactions (along with corresponding branching ratios) and the familiar neutrino fluxes are mentioned in the parentheses. This figure is adopted from [47].

The net effect of each of the chain reactions discussed above is the following fusion process,

$$4p \rightarrow {}^{4}He^{++} + 2\nu_e + n\gamma, \tag{1.10}$$

where n depends on the particular reaction. The C, N,O produced in the CNO cycle discussed above also act as catalysts in this fusion process. We note that there is a high expectation of ν_e flux generated according to SSM. The calculation of the total solar neutrino flux on earth has been done in [48] and is about $5.94 \times 10^{10} cm^{-2} s^{-1}$. .

Years of study of solar neutrinos have convincingly established that neutrino oscillations are the cause of the deficits of $1/3$ to $1/2$ in the measured ν_e flux relative to the SSM. The water Cherenkov detectors of the experiments Kamiokande and Super-Kamiokande [50] and the heavy water detector at SNO [51] measure the higher energy ($4 - 15$ MeV) neutrinos from the sun. ^{37}Cl experiment [52] detects the

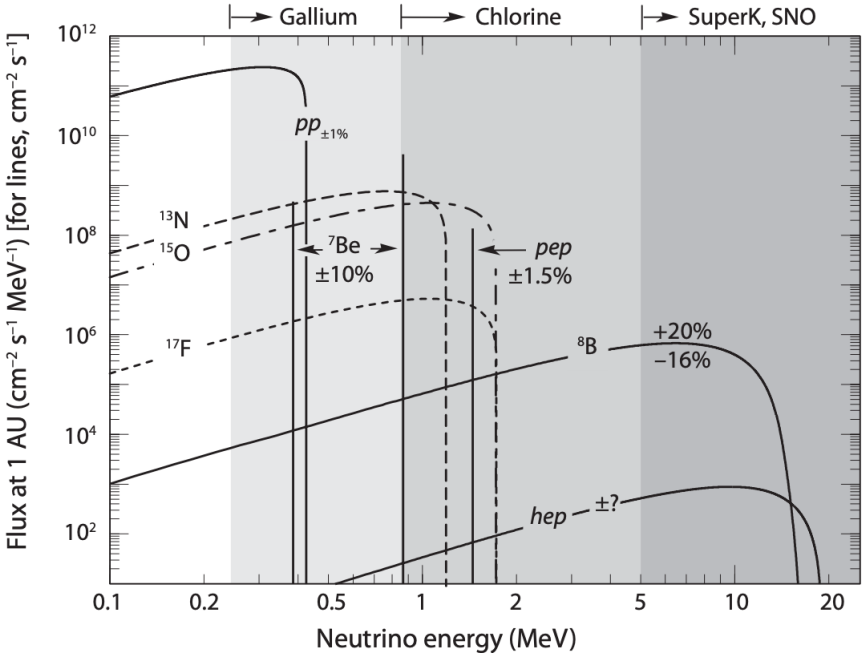

Figure 1.3: Solar neutrino flux shown as a function of neutrino energy as predicted by SSM [44–46]. The energy threshold of several solar neutrino experiments are also shown. This figure is taken from [49].

intermediate-energy neutrinos from ^7Be and from the CNO cycle, while the ^{71}Ga experiments, SAGE [53], GALLEX [54], and GNO [55] look for the low energy pp neutrinos. These experiments have conclusively established the oscillations of ν_e to ν_μ and/or ν_τ. Very recently, the liquid scintillator experiment Borexino, which has a low threshold of about 200 keV, was able to detect, for the first time, neutrinos produced in the CNO cycle of the sun [56].

- **Atmospheric neutrinos:** Primary cosmic rays interact with the nuclei in the atmosphere to produce secondary particles pions and kaons. Pions and kaons subsequently decay to muon neutrino, electron neutrino and the corresponding anti-neutrinos:

$$\begin{aligned} \pi^+, K^+ \rightarrow \quad & \nu_\mu \mu^+ \\ & \hookrightarrow \quad \nu_\mu e^+ \nu_e \bar{\nu}_\mu. \\ \pi^-, K^- \rightarrow \quad & \bar{\nu}_\mu \mu^- \\ & \hookrightarrow \quad \bar{\nu}_\mu e^- \bar{\nu}_e \nu_\mu., \end{aligned}$$

The ratio of ν_μ to ν_e flux becomes roughly 2:1 since ν_e gets produced in the second step above. The energy range of the atmospheric neutrinos is from a few hundred

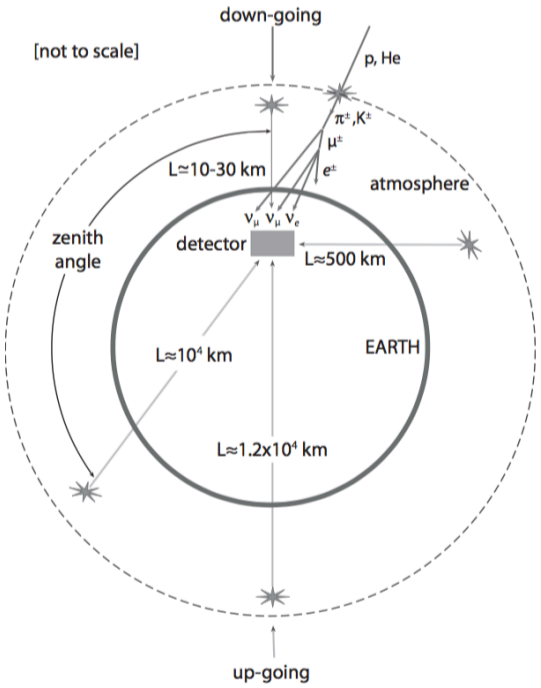

Figure 1.4: A schematic view of different zenith angles of atmospheric neutrinos and the different distances they travel before detection [57].

MeV to 10^8 GeV. Atmospheric neutrino flux falls steeply as $E^{-2.7}$ for energies above 1 GeV and the flux becomes undetectably small after about 100 TeV [58].

Atmospheric neutrino flux peaks at zenith angle $\approx 90°$, i.e near the horizon, due to the larger length of atmosphere available in that direction. Atmospheric neutrinos observed at different zenith angles have different path lengths:- from $\sim 10 - 30$ km for downward going neutrinos to $\sim 10^4$ km for upward going neutrinos. See fig. 6.2 for a schematic (not to scale) of the atmospheric neutrinos (taken from [59]). Atmospheric neutrinos have a long energy range and oscillation length, and hence are very useful to study neutrino oscillations as well as new physics.

The signature of atmospheric neutrino oscillation was noted at [60] when there was a difference between the number of ν_μ calculated theoretically and observed experimentally. Atmospheric neutrino studies in Soudan-2 [61, 62] and MACRO [63, 64] experiments have shown results that are consistent with Super-K results. Unlike these experiments, MINOS [65] can detect the neutrino and anti-neutrino modes separately through CC interactions. CHOOZ experiment [66, 67] has been able to put upper limits on δ_{13} and Δm^2_{13} indicated by atmospheric neutrino experiments.

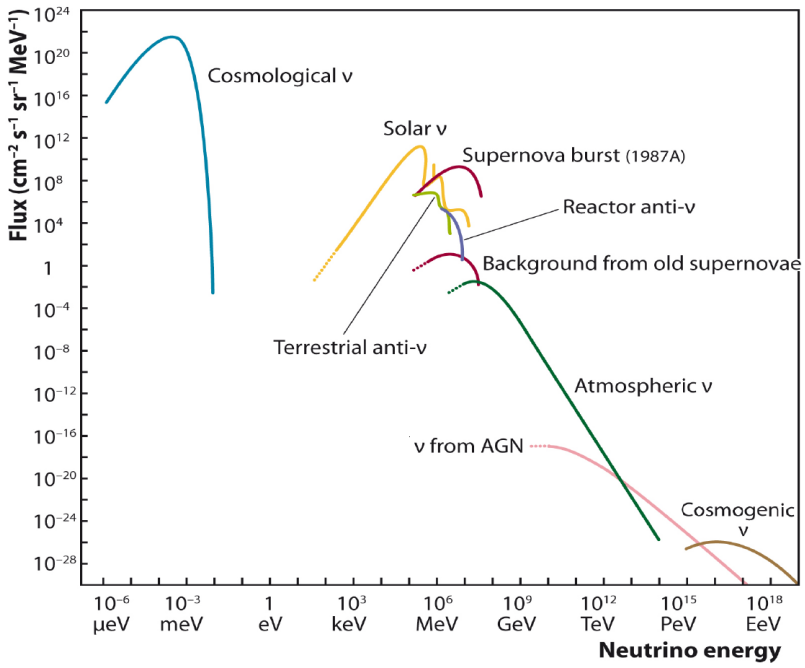

Figure 1.5: Neutrino flux shown as a function of neutrino energy.

India based Neutrino Observatory (INO) [68] collaboration has been working extensively to study atmospheric neutrinos through Iron CALorimeter (ICAL). The long-baseline experiments can probe the oscillation parameters independently and provide crucial information for the atmospheric neutrino sector.

- **Accelerator neutrinos:** Here the beams of neutrinos are produced by the decay of pions, kaons, and muons created by a proton beam hitting a target. They can be of the following three categories.

  1. *Pion Decay In Flight (DIF):* Neutrino beam is produced by the decay of pions and kaons initially produced by a proton beam hitting a target. The pions and kaons are allowed to decay in a decay tunnel of the length of the order of 100 m. The beam is mainly composed of ν_μs or $\bar{\nu}_\mu$s. The typical energy of the neutrinos is of the order of a few GeV but can be much larger, depending on the energy of the proton beam.
  2. *Muon Decay At Rest (DAR):* In this process lower energy beam composed of muon antineutrinos coming from the decay

$$\mu^+ \rightarrow e^+ + \nu_e + \bar{\nu}_\mu$$

of the μ^+ produced in the pion decay:

$$\pi^+ \rightarrow \mu^+ + \nu_\mu \tag{1.11}$$

(the π^- are mostly absorbed by nuclei) are produced. The energy of neutrinos thus produced can be several tens of MeV.

3. *Beam Dump:* a proton beam with very high energy, of the order of some hundreds of GeV, is completely stopped in a thick target, called the beam dump, where the proton nucleon interactions generate heavy hadrons. The charmed heavy hadrons decay promptly with practically equal branching ratios into electrons and muons, emitting equal fluxes of electron and muon neutrinos with energies of the order of 10^2 GeV.

Studies on accelerator neutrinos can provide important information about many new physics scenarios, such as sterile neutrino searches, neutrino-nucleus interactions, and matter effects in neutrino oscillation. ND280 [69], T2K [70] and Super-K [71] in Japan get their neutrino flux from J-PARC and MicroBoone [72], MINERvA [73], ICARUS [74] and SBND [75] get the neutrino flux from NuMI [76] at Fermilab, USA.

- **Reactor neutrinos:** Nuclear reactors are the major sources of artificially produced neutrinos. Power generation in nuclear reactors takes place through the fission of neutron-rich isotopes like U^{235}, U^{238} and Pu^{239}. Electron antineutrinos are produced by the chain of inverse β-decays of the fission products in the energy range of 0.1 to 10 MeV. The calculation of a reactor antineutrino spectrum is a difficult task since the decay of each isotope produces a different neutrino spectrum. The qualitative features of the existing calculations are reviewed in [77, 78]. The electron anti-neutrino oscillation observed in reactor experiments are done through the measurements of the products of the inverse-beta-decay reaction $\bar{\nu}_e + p \rightarrow n + e^+$. This can be an efficient tool to do a precise measurement of θ_{13}. Results from Double CHOOZ [79], Daya Bay [80] and RENO [81] has shown sensitivity at very low θ_{13}-value ($\sin^2 2\theta_{13} = 0.006$).

- **Core-collapse supernova neutrinos:** Stars more massive than about $8M_\odot$ undergo gravitational collapse that leads to the production of a neutron star or a black hole. Among them Stars with mass $\gtrsim 10M_\odot$ have iron cores that exceed the Chandrasekar limit of about $1.44M_\odot$; they can no longer be supported against gravitational collapse by electron degeneracy pressure and catastrophic collapse ensues.

Once the core of the star becomes constituted primarily of iron, further compression of the core does not ignite nuclear fusion and the star is unable to thermodynamically support its outer envelope. As the surrounding matter falls inward under gravity, the temperature of the core rises and iron dissociates into α particles and nucleons. Electron capture on protons becomes heavily favored and electron neutrinos are produced[1]. The collapse continues until $3-4$ times nuclear density is reached, after which the inner core rebounds, sending a shock wave across the outer core and into the mantle. This shock wave loses energy as it heats the matter it traverses and incites further electron capture on the free protons left in the wake of the shock. During the few milliseconds in which the shock wave travels from the inner core to the neutrinosphere, electron neutrinos are released in a pulse. This neutronization burst carries away approximately 10^{51} ergs of energy. However, 99% of the binding energy $E_b \sim 10^{53}$ ergs of the protoneutron star (which is about 10% of the star's rest mass energy) is released in the following $\sim 10s$. The primary processes are beta decay (providing a source of electron antineutrinos), $\nu_e\ \bar{\nu}_e$ annihilation, e^+e^- annihilation, and nucleon bremsstrahlung ($N+N \rightarrow N+N+\nu+\bar{\nu}$, which give all flavors of neutrinos: $\nu_e\bar{\nu}_e, \nu_\mu\bar{\nu}_\mu, \nu_\tau\bar{\nu}_\tau$), in addition to electron capture. Kamiokande II [82] and Irvine-Michigan-Brookhaven [83] results strongly support the core-collapse supernova model. Super-Kamiokande [84] and SNO [85] experiments can study this phenomenon in further detail.

- **Astrophysical neutrinos:** Very high energy neutrino fluxes from cosmologically distant sources are generally expected in association with the production of cosmic-rays (CR), whose energy spectrum can extend to even 10^{20} eV and is likely dominated above $\sim 3\times10^{17}$ eV by protons, neutrons, and nuclei of extragalactic origin. Source candidates include galactic sources like supernova remnants (SNR) and extragalactic sources like Active Galactic Nuclei (AGN) and Gamma Ray Bursts (GRB). This Ultra High-energy (UHE) neutrino production is thought to be associated with the interactions of high-energy protons that produce energetic charged pions by $p\gamma$ or by $p\bar{p}$ interactions. In sources that are optically thin to meson-nucleon interactions, the $\pi^+ \rightarrow \mu^+\nu_\mu$ decays and subsequent $\mu^+ \rightarrow e^+\nu_e\bar{\nu_\mu}$ decays (and corresponding π^- decay chain) lead to ultra high-energy neutrinos. The decays of neutral pions, $\pi^0 \rightarrow \gamma\gamma$, may be observed as gamma ray signals in experiments such as observations by the Fermi Gamma-ray Space Telescope (FGST). GALLEX [86]

[1]This process is known as neutronization.

in Italy and SAGE [53] have detected low energy (<400 keV) neutrinos which are a primary component of the solar neutrino flux. ICECUBE [87] at Antarctica and KM3NET [88], ANTARES [89] under the Mediterranean sea are neutrino telescopes under ice and water respectively and these experiments are expected to provide crucial information about astrophysical neutrino searches.

- **Relic neutrinos:** Relic neutrinos are an important product of the standard hot Big Bang. Neutrinos were in thermal equilibrium in the hot plasma which filled the early Universe through weak interactions with the other particles. As the universe expanded and cooled, the rates of weak interaction processes decreased and neutrinos decoupled when these rates became smaller than the expansion rate. Since for the three known light neutrinos with masses smaller than about 1 eV the decoupling occurred when they were relativistic, these neutrinos are hot relics. Relic neutrinos pervade space, but their temperature T_ν^0 is extremely small, being of the order of 10^4 eV. Their weak interaction cross-section with matter is thus extremely small and hence the direct detection of relic neutrinos is a very difficult task with present experimental techniques.

1.4 Neutrino oscillation: outstanding questions

In the late 1950s Pontecorvo proposed the phenomenon of neutrino oscillation analogous to $K^0 - \bar{K}^0$ oscillation [19, 90]. At that point, experimental data could only ascertain the existence of electron neutrino. Eventually, muon and tau neutrinos were discovered in 1962 and 2000 respectively. Maki, Nakagawa and Sakata proposed the model of mixing of neutrino flavours in 1962 [91]. Pontecorvo then extended this discussion and in 1967 predicted that the solar neutrino problem is a consequence of $\nu_e \to \nu_\mu$ transition [22]. In 1998 neutrino oscillation was detected experimentally in Super-Kamiokande collaboration [92]. We have discussed about the formalism of neutrino oscillation in more detail in Chapter 2. This finding opened up a broad aspect of beyond standard model (BSM) physics. From the theoretical model of leptogenesis, the search for neutrino mass and CP violation have become key observables in current and future neutrino experiments. Also, with the increase in the precision of measurement in the upcoming neutrino experiments, one can expect to explore the domain of new physics, such as non-standard interactions (NSI) of neutrinos, or studies of superluminal neutrinos.

In addition to the standard three neutrino phenomenology, there exists some exper-

imental evidence, although not conclusive and some theoretical models which may indicate to some exotic phenomena that go beyond the standard framework. The possibility of the existence of a fourth neutrino mass eigenstate (called *sterile* neutrino) originates from some anomalous neutrino experiment results. The LSND experiment [93] found evidence for $\bar{\nu}_\mu \rightarrow \bar{\nu}_e$ oscillation at 3.3σ significance (oscillation probability is $(2.64\pm0.67\pm0.45)\times10^{-3}$). The mass squared difference which can successfully explain this LSND $\bar{\nu}_e$ excess (LSND anomaly) is $\Delta m^2_L \sim 1\ eV^2$. Since this mass scale is very different from the existing solar ($\Delta m^2_{21} \sim 10^{-5}\ eV^2$) and the atmospheric ($\Delta m^2_{31} \sim 10^{-3}\ eV^2$) mass differences, this suggests that there may exist a fourth neutrino mass eigenstate, called sterile neutrino, participating in neutrino oscillation. IceCube, Katrin, SBN, ANTARES, STEREO are a few experiments which aim to search for sterile neutrinos with high precision using different neutrino sources and different detection techniques.

The Standard Model of particle physics cannot successfully explain the origin of neutrino masses. Though BSM phenomenology can be introduced to the standard framework through effective field theory which can account for the mass generation of neutrinos. The seesaw mechanism explains the generation of neutrino mass considering the presence of an additional right handed neutrino. In literature, there are several mass models which incorporate the seesaw mechanism intrinsically. The ongoing and future experimental facilities may shine light to the viability of these theories.

Another important question that may arise in the context of neutrino oscillations is the conservation of the intrinsic CPT violation which is intimately related to the Lorentz symmetry. Fundamental symmetry such as the Lorentz Invariance (LI) may spontaneously break at the Planck scale in some unified theories. In a low energy effective field theory such as the Standard Model, such violations of LI can manifest themselves perturbatively. The neutrino sector, where neutrinos can oscillate flavours while propagating through macroscopic distances, is one particularly noteworthy window through which the Lorentz invariance violation (LIV) effects can potentially be observed. The presence of LIV is expected to manifest as Planck suppressed interference effects to the mass induced neutrino oscillations.

In order to study the new physics in neutrino oscillation more precisely one would need to have a clear understanding of the interaction of the neutrinos with the detectors, *i.e.*, with the nuclei. The final state interactions (FSI)[2] in the nuclear medium are being studied widely in the current experimental domain. More precise data of the neutrino-

[2]When a neutrino interacts with the nucleon and knocks out another nucleon, that nucleon may re-interact with other particles in the nuclear medium. This is known as FSI.

nucleus interaction will reduce the systematic uncertainties in the ongoing and forthcoming neutrino experiments.

1.5 Problem statement

To resolve the interesting issues discussed above, a large number of ambitious neutrino experiments have been designed. This thesis addresses the capabilities of the ongoing and forthcoming LBL experiments in probing the new physics scenario.

- In case the sterile neutrino exists in nature, interference terms will arise due to the additional CP phases. Not taking these terms into consideration during the analysis of LBL neutrino oscillation data can impact the physics searches. In this thesis, we aim to study how the ongoing and forthcoming LBL experiments like DUNE, NOvA, T2K and T2HK can probe these standard and new CP phases (δ_{13}, δ_{24} and δ_{34}). We have also briefly explored how the parameter space can change in the case of neutrinoless beta decay due to the introduction of a sterile flavour.

- One of the most discussed model for the neutrino mass generation is Left-Right Symmetric Model (LRSM) which incorporates the seesaw mechanism. This model considers the addition of a single right-handed neutrino in the SM Gauge group and implements an additional scalar triplet. The mass term for neutrino can be written in terms of Yukawa couplings [94]. Although the study of neutrino mass is BSM physics, most neutrino oscillation analyses are done assuming Standard Model neutrino interactions. Non-standard interactions (NSI) of neutrinos that originate from neutrino mass models, can affect the oscillation probabilities as a sub-leading effect and can bring about significant changes in the observable results in the experiments. By implementing effective field theory, a correlation between the parameter spaces of LRSM and NSI can be found. In this thesis, using the available LBL data from NOvA and T2K, we have aim to study how these parameter spaces can be probed in terms of the mass and coupling of the new scalar triplet.

- If we consider the existence of LIV in nature, that will produce modifications in the spectra of events predicted with the standard three-neutrino paradigm. High statistics neutrino experiments represent a rich source of information on neutrino oscillations stemming from its energy and direction dependent multi-layer matter effects. In the current manuscript, we aim to present the physics potential of future

LBL neutrino experiments, namely P2O and DUNE, in measuring sub-dominant effects in neutrino oscillations coming from the breaking of Lorentz symmetry. We have done a χ^2 analysis in order to put a bound on the relevant LIV parameters.

- Main INjector ExpeRiment for v-A (MINERvA) experiment studies the neutrino-nucleus interaction for both heavy and light nuclei. The phenomenon of charged pion production in such detector is currently studied with more precision. In this document, we have studied charged pion production at low energy in MINERvA detector through the production of Michel electron.

We start with the formalism of neutrino oscillation in chapter 2. Then, in chapter 3, we have focussed on the phenomenology of the light sterile neutrino mixing with the active neutrinos through oscillation and how efficiently the LBL experiments can probe the CP phases. In chapter 4, we have discussed the capability to probe the LRSM in terms of NSI manifested in LBL experiments. In chapter 5, we have studied how the LBL experiments can probe the parameter space of LIV. Lastly, in chapter 6, we have investigated the charged pion production channel through Michel electron in a neutrino-nuclear experiment.

Chapter 2

Neutrino Oscillation

The quantum mechanical phenomenon in which the neutrinos are observed at a later time to acquire a different flavor than that at the source is called neutrino oscillation. The initial theory of neutrino oscillation is proposed by Pontecorvo in 1957. But the standard formalism of neutrino oscillation with the plane wave approximation was introduced in 1975-76 by Eliezer and Swift [24]. In this chapter, we aim to do a detailed derivation of the active neutrino oscillation in vacuum as well as in matter. In the end, we have shown how precisely the oscillation parameters have been measured in the experiments.

2.1 Standard derivation of neutrino oscillation

Before proceeding to derive the neutrino oscillation in the standard framework, we first make the following assumptions:

- Neutrino oscillation experiments are not sensitive to the difference in neutrino masses during the production or detection process. They are detected through charged-current or neutral-current weak scattering processes. These neutrinos are described by their flavor state.

- Flavor neutrinos have a definite momentum $\vec{p}$, i.e. all the massive neutrino components have the same momentum. However, there is an alternative method (known as *wave packet analysis* in which the wave packet nature of propagating neutrinos is taken into account [95–99]) of deriving the neutrino oscillation probability where this equal momentum assumption is irrelevant.

- It can be shown in the so-called *wave packet analysis* of the neutrino oscillation phenomena that neutrinos are described by wave packets that are localized in the pro-

duction process at the production time. They propagate between the production and the detection processes with a group velocity close to the velocity of light. The propagation time t is equal to the distance L traveled by the neutrino between production and detection considering $c = 1$.

a neutrino with flavor α and momentum $\vec{p}$, created in a charged-current weak interaction process from a charged lepton ℓ_α^- or together with a charged antilepton ℓ_α^+, is described as the flavor state,

$$|\nu_\alpha\rangle = \sum_k U_{\alpha k}^* |\nu_k\rangle \quad (\alpha = e, \mu, \tau; \langle\nu_k|\nu_j\rangle = \delta_{kj}). \tag{2.1}$$

where the unitary matrix $U_{\alpha k}^*$ is known as the mixing matrix or the Pontecorvo-Maki-Nakagawa-Sakata (PMNS) matrix [21, 22]. The index k stands for the mass eigenstate of the neutrinos. Each flavor eigenstate of neutrinos are linear superpositions of the mass eigenstates. In general, for an $N \times N$ unitary mixing matrix, there are $N(N-1)/2$ mixing angles and $N(N+1)/2$ phases. To see this, we first note that a general $N \times N$ matrix U has N^2 complex elements *i.e.*, it can be described by $2N^2$ real elements. But if U is unitary, not all the $2N^2$ elements are independent. Invoking the unitarity condition $U^\dagger U = I$, we see that,

$$\sum_{k=1..N} U_{ki}^* U_{kj} = \delta_{ij}. \tag{2.2}$$

For $j = i$, Eq. 2.2 gives,

$$\sum_{k=1..N} |U_{ki}|^2 = 1 \tag{2.3}$$

This gives N such conditions corresponding to $i = 1..N$. For $j \neq i$, Eq. 2.2 gives,

$$\sum_{k=1..N} U_{ki}^* U_{kj} = 0. \tag{2.4}$$

Since there are ${}^N C_2$ ways in which a pair of distinct (i, j) values can be chosen from a set of N values, Eq. 2.4 gives ${}^N C_2$ conditions. Now, invoking the other unitarity condition $UU^\dagger = I$, and taking $j = i$, we arrive at the identical N such conditions as Eq. 2.3. But for $j \neq i$ in $UU^\dagger = I$ we get the following different set of ${}^N C_2$ conditions,

$$\sum_{k=1..N} U_{ki} U_{kj}^* = 0. \tag{2.5}$$

Thus the number of independent parameters that can completely parameterise the $N \times N$ unitary matrix U is given by $2N^2 - N - (2 \times {}^N C_2) = N^2$. In the current context of neutrino

mixing, among these N^2 parameters, the number of angles describing mixing between a pair of generations is ${}^{N}C_2$ or $N(N-1)/2$. The rest of the parameters are the CP phases are the number of CP phases are thus given by $N^2 - N(N-1)/2$ or $N(N+1)/2$.

It is important to note that not all the CP phases are physical. To understand this, we note that the $N \times N$ unitary matrix U with its $N(N-1)/2$ mixing angles and $N(N+1)/2$ phases can be written as follows [100, 101].

$$U = D(\omega) \prod_{a<b} W^{ab}(\theta_{ab}, \eta_{ab}) \qquad \text{with } a, b = 1, ..., N. \tag{2.6}$$

where, $D(\omega) = \text{diag}(e^{i\omega_1}, ..., e^{i\omega_N}) = exp[i \sum_{a=1}^{N} \omega_a A^{aa}]$ is a diagonal unitary matrix defined by the set of N phases $\omega = (\omega_1 ..., \omega_N)$. The matrix A^{ab} is defined as $[A^{ab}]_{rs} = \delta_{ar}\delta_{bs}$ and represents the N^2 generators of unitary transformations. W^{ab} in Eq. 2.6 is a unitary and unimodular matrix representing complex rotation in the $a-b$ plane with an angle θ_{ab} and a phase η_{ab} ($a \neq b$). They can be written as [47],

$$\begin{aligned} \big[W_{ab}(\theta_{ab}, \eta_{ab})\big]_{rs} &= [exp(\theta_{ab} e^{i\eta_{ab}} A^{ab} - \theta_{ab} e^{-i\eta_{ab}} A^{ba})]_{rs} \\ &= \delta_{rs} + (\cos\theta_{ab} - 1)(\delta_{ra}\delta_{sa} + \delta_{rb}\delta_{sb}) + \sin\theta_{ab}(\delta_{ra}\delta_{sb} e^{i\eta_{ab}} - \delta_{rb}\delta_{sa} e^{-i\eta_{ab}}). \end{aligned} \tag{2.7}$$

Thus, for *e.g.*,

$$W_{12}(\theta_{12}, \eta_{12}) = \begin{pmatrix} \cos\theta_{12} & \sin\theta_{12} e^{i\eta_{12}} & 0 \\ -\sin\theta_{12} e^{-i\eta_{12}} & \cos\theta_{12} & 0 \\ 0 & 0 & 1 \end{pmatrix}.$$

Thus we observe that Eq. 2.6 is a way of writing the $N \times N$ unitary matrix U in terms of the $N(N-1)/2$ mixing angles θ_{ab}, and the $N(N+1)/2$ phases have been divided into $N(N-1)/2$ phases η_{ab} and N phases ω_k. To analyze the removal of unphysical phases, we now introduce a set of N arbitrary phases $\varphi = (\varphi_1, ..., \varphi_N)$, and write Eq. 2.6 as,

$$\begin{aligned} U &= D(\omega - \varphi) \Bigg[\prod_{a<b} D(\varphi) W^{ab}(\theta_{ab}, \eta_{ab}) D^{\dagger}(\varphi) \Bigg] D(\varphi) \\ &= D(\omega - \varphi) \Bigg[\prod_{a<b} W^{ab}(\theta_{ab}, \eta_{ab} + \varphi_a - \varphi_b) \Bigg] D(\varphi), \end{aligned} \tag{2.8}$$

where we use Eq. 2.7 to arrive at the second line. It is easy to note from Eq. 2.8 that the set of arbitrary phases φ can be chosen so that $N-1$ phases η_{ab} can be extracted (since there are $N-1$ independent differences $\varphi_a - \varphi_b$). Thus eventually one φ_a still remains hanging. To proceed further, let us look at the $N = 3$ scenario and then the general

case will easily follow. For $N = 3$, there are 3 mixing angles $\theta_{12}, \theta_{13}, \theta_{23}$ and 6 phases $\omega_1, \omega_2, \omega_3, \eta_{12}, \eta_{13}, \eta_{23}$. If we choose to extract η_{12} and η_{23} from the complex rotarions with the choice $(\varphi_1, \varphi_2, \varphi_3) = (\varphi_2 - \eta_{12}, \varphi_2, \varphi_2 + \eta_{23})$ (so that only φ_2 remains), then the rotations in the $2-3$ and $1-2$ planes are real and we denote them as R^{23} and R^{12} respectively. we can then write the mixing matrix U in Eq. 2.8 as [101],

$$\begin{aligned} U &= D(\omega - \varphi)R^{23}(\theta_{23})W^{13}(\theta_{13}, \eta_{13})R^{12}(\theta_{12})D(\varphi) \\ &= e^{i\omega_2}\text{diag}(e^{i(\omega_1-\omega_2+\eta_{12})}, 1, e^{i(\omega_3\omega_2-\eta_{23})})R^{23}(\theta_{23})W^{13}(\theta_{13}, \eta_{13})R^{12}(\theta_{12})\text{diag}(e^{-i\eta_{12}}, 1, e^{i\eta_{23}}). \end{aligned} \tag{2.9}$$

Note that, in deriving the second line of Eq. 2.9 the factor $e^{-i\varphi_2}$ arising from $D(\omega - \varphi)$ cancels out the factor $e^{i\varphi_2}$ arising from $D(\varphi)$. Thus the value of φ_2 turns out to be irrelevant and can be taken to be zero for simplicity. Thus, we eventually see that effectively 5 phases can be factorized outside of the rotation $R^{23}(\theta_{23})W^{13}(\theta_{13}, \eta_{13})R^{12}(\theta_{12})$ and only one phase η_{13} remains inside. The five overall phase factors can be eliminated by redefinition of the fields so that the weak Lagrangian remains unchanged and only one physical phase remains. For a general case of N generations where there are $N(N+1)/2$ phases to begin with, $2N-1$ of them can be eliminated and the number of physical CP phases remaining is $N(N+1)/2 - (2N-1)$ or $(N-1)(N-2)/2$. For the standard 3 flavor scenario, $N = 3$ there are three mixing angles (θ_{12}, θ_{23} and θ_{13}) and only one CP violating phase known as δ_{CP}. The unitarity of the mixing matrix denotes that the flavor states are orthonormal:

$$\langle \nu_\alpha | \nu_\beta \rangle = \delta_{\alpha\beta}. \tag{2.10}$$

The massive neutrino states $|\nu_k\rangle$ are eigenstates of the Hamiltonian:

$$\mathcal{H} |\nu_k\rangle = E_k |\nu_k\rangle , \tag{2.11}$$

with energy eigenvalues $E_k = \sqrt{|\vec{p}|^2 + m_k^2}$. The Schrödinger equation

$$i\frac{d}{dt} |\nu_k(t)\rangle = \mathcal{H} |\nu_k(t)\rangle \tag{2.12}$$

implies that the massive neutrino states evolve in time as plane waves:

$$|\nu_k(t)\rangle = e^{-iE_k t} |\nu_k\rangle . \tag{2.13}$$

Now, if we consider a flavor state $|\nu_\alpha(t)\rangle$ which describes a neutrino created with a particular flavor α at time t = 0. So using equations 2.1-2.13, we can now write the time evolution of the flavor state,

$$|\nu_\alpha(t)\rangle = \sum_k U^*_{\alpha k} e^{-iE_k t} |\nu_k\rangle , \tag{2.14}$$

such that $|\nu_\alpha(t=0)\rangle = |\nu_\alpha\rangle$. Now, using the unitarity relation,

$$\sum_\alpha U^*_{\alpha k} U_{\alpha j} = \delta_{jk}, \tag{2.15}$$

and inverting equation 2.1, the massive neutrino states can be expressed in terms of the flavor states as,

$$|\nu_k\rangle = \sum_\alpha U_{\alpha k} \, |\nu_\alpha\rangle \, . \tag{2.16}$$

Using the relation 2.16 in equation 2.14, we can write,

$$|\nu_\alpha(t)\rangle = \sum_{\beta=e,\mu,\tau} \left(\sum_k U^*_{\alpha k} U_{\beta k} e^{-iE_k t} \right) |\nu_\beta\rangle \, . \tag{2.17}$$

The amplitude of the neutrino flavor transition $\nu_\alpha \to \nu_\beta$ as a function of time is given by,

$$A_{\nu_\alpha \to \nu_\beta}(t) = \langle \nu_\beta | \nu_\alpha(t) \rangle \sum_k U^*_{\alpha k} U_{\beta k} e^{-iE_k t}, \tag{2.18}$$

and the probability of the flavor transition $\nu_\alpha \to \nu_\beta$ is given by,

$$P_{\nu_\alpha \to \nu_\beta}(t) = |A_{\nu_\alpha \to \nu_\beta}(t)|^2 = \sum_{k,j} U^*_{\alpha k} U_{\beta k} U_{\alpha j} U^*_{\beta j} e^{-i(E_k - E_j)t}. \tag{2.19}$$

For ultrarelativistic neutrinos, the dispersion relation $E_k = \sqrt{\vec{p}^2 + m_k^2}$ can be written as (using the equal momentum assumption),

$$E_k \approx E + \frac{m_k^2}{2E} \implies E_k - E_j \approx \frac{\Delta m^2_{kj}}{2E}, \tag{2.20}$$

where $\Delta m^2_{kj} = m^2_k - m^2_j$, is the mass squared difference. Also, $E = |\vec{p}|$, neglecting the mass contribution. In an actual neutrino oscillation experiment, the neutrino propagation length L between the source and the detector is measured instead of the propagation time t. Since neutrinos are ultrarelativistic, we use the assumption $t \approx L$ and the oscillation probability in equation 2.19 as a function of energy,

$$P_{\nu_\alpha \to \nu_\beta}(t) = |A_{\nu_\alpha \to \nu_\beta}(L, E)|^2 = \sum_{k,j} U^*_{\alpha k} U_{\beta k} U_{\alpha j} U^*_{\beta j} e^{-i \frac{\Delta m^2_{kj}}{2E} L}. \tag{2.21}$$

Using the unitarity of the mixing matrix (equation 2.15),

$$\begin{aligned} \sum_\beta P_{\nu_\alpha \to \nu_\beta}(L, E) &= 1 \\ \sum_\alpha P_{\nu_\alpha \to \nu_\beta}(L, E) &= 1. \end{aligned} \tag{2.22}$$

where, the running indices α and β denote the initial and final flavors of neutrinos, respectively. The unitarity condition of the mixing matrix allows the sum of the probabilities to be unity when it is summed over all the initial flavors, as well as, all the final flavors, individually. For example, in the case of three neutrino flavors,

$$\sum_{\beta=e,\mu,\tau} P_{\nu_\alpha\to\nu_\beta}(L,E) = P_{\nu_\mu\to\nu_e}(L,E) + P_{\nu_\mu\to\nu_\mu}(L,E) + P_{\nu_\mu\to\nu_\tau}(L,E) = 1$$

$$\sum_{\alpha=e,\mu,\tau} P_{\nu_\alpha\to\nu_\beta}(L,E) = P_{\nu_e\to\nu_\mu}(L,E) + P_{\nu_\mu\to\nu_\mu}(L,E) + P_{\nu_\tau\to\nu_\mu}(L,E) = 1.$$

Now, from relation 2.15, one can show that

$$\sum_k |U_{\alpha k}|^2 |U_{\beta k}|^2 = \delta_{\alpha\beta} - 2\sum_{k>j} Re\left[U^*_{\alpha k} U_{\beta k} U_{\alpha j} U^*_{\beta j}\right], \tag{2.23}$$

which allows us to write the oscillation probability in the following form:

$$\begin{aligned} P_{\nu_\alpha\to\nu_\beta} = \delta_{\alpha\beta} \quad &- \quad 4\sum_{k>j} Re\left[U^*_{\alpha k} U_{\beta k} U_{\alpha j} U^*_{\beta j}\right] \sin^2(\phi_{kj}) \\ &+ \quad 2\sum_{k>j} Im\left[U^*_{\alpha k} U_{\beta k} U_{\alpha j} U^*_{\beta j}\right] \sin(2\phi_{kj}), \text{where, } \phi_{kj} = \frac{\Delta m^2_{kj} L}{4E} \end{aligned} \tag{2.24}$$

Equation 2.24 is known as the transition probability when $\alpha \neq \beta$[1]

For the case of antineutrinos, one starts with

$$|\bar{\nu}_\alpha\rangle = \sum_k U_{\alpha k} |\bar{\nu}_k\rangle \quad (\alpha = e,\mu,\tau; \langle\nu_k|\nu_j\rangle = \delta_{kj}), \tag{2.26}$$

and gets the following expression for oscillation probability of antineutrinos,

$$\begin{aligned} P_{\bar{\nu}_\alpha\to\bar{\nu}_\beta} = \delta_{\alpha\beta} \quad &- \quad 4\sum_{k>j} Re\left[U^*_{\alpha k} U_{\beta k} U_{\alpha j} U^*_{\beta j}\right] \sin^2(\phi_{kj}) \\ &- \quad 2\sum_{k>j} Im\left[U^*_{\alpha k} U_{\beta k} U_{\alpha j} U^*_{\beta j}\right] \sin(2\phi_{kj}). \end{aligned} \tag{2.27}$$

[1]When $\alpha = \beta$,it is known as the survival probability and can be written as,

$$P_{\nu_\alpha\to\nu_\alpha} = 1 - 4\sum_{k>j} Re|U_{\alpha k}|^2 |U_{\alpha j}|^2 \sin^2(\phi_{kj}) \tag{2.25}$$

2.2 Neutrino oscillation in vacuum

Neutrino oscillation in vacuum will give us the basic idea about the propagation of neutrinos unhindered by the interactions with the Standard Model particles, as seen in the case of matter oscillation. It is simple to derive because the mass eigenstates evolve exactly as shown in the previous section (equation 2.11). We give a brief description of it below both in the context of 2 flavors and 3 flavors.

2.2.1 Two flavor oscillation

In this case, there is only one mixing angle θ and only one mass squared difference namely $\Delta m^2 = m_2^2 - m_1^2$. The two flavor neutrino states are linear superpositions of the two massive neutrinos ν_1 and ν_2 with coefficients given by the elements of the two-neutrino effective mixing matrix,

$$U = \begin{pmatrix} \cos\theta & \sin\theta \\ -\sin\theta & \cos\theta \end{pmatrix}, \quad \text{where } 0 \leqslant \theta \leqslant \pi/2. \tag{2.28}$$

Now using equation 2.24 we can write,

$$P_{\nu_\alpha \to \nu_\beta}(L, E) \;=\; \sin^2 2\theta \sin^2\left(\frac{\Delta m^2 L}{4E}\right), \quad (\alpha \neq \beta). \tag{2.29}$$

It is convenient for practical purposes to write the probability expression after unit conversions, in the following form,

$$P_{\nu_\alpha \to \nu_\beta}(L, E) = \sin^2 2\theta \sin^2 1.27\left(\frac{\Delta m^2[eV^2] L[km]}{E[GeV]}\right) \tag{2.30}$$

2.2.2 Three flavor oscillation:

For three generations, one has 3 mixing angles ($\theta_{12}, \theta_{13}, \theta_{23}$), 2 mass squared differences, and one Dirac CP phase (δ_{cp}). The PMNS matrix U can be conveniently parameterized as,

$$\begin{aligned} U &= R_{23}W_{13}R_{12} \\ &= O(\theta_{23})O(\theta_{13},\delta_{13})O(\theta_{12}) \\ &= \begin{pmatrix} 1 & 0 & 0 \\ 0 & c_{23} & s_{23} \\ 0 & -s_{23} & c_{23} \end{pmatrix} \begin{pmatrix} c_{13} & 0 & s_{13}e^{-i\delta_{cp}} \\ 0 & 1 & 0 \\ -s_{13}e^{i\delta_{cp}} & 0 & c_{13} \end{pmatrix} \begin{pmatrix} c_{12} & s_{12} & 0 \\ -s_{12} & c_{12} & 0 \\ 0 & 0 & 1 \end{pmatrix} \\ &= \begin{pmatrix} c_{12}c_{13} & s_{12}c_{13} & s_{13}e^{-i\delta_{\rm CP}} \\ -s_{12}c_{23} - c_{12}s_{13}s_{23}e^{i\delta_{\rm CP}} & c_{12}c_{23} - s_{12}s_{13}s_{23}e^{i\delta_{\rm CP}} & c_{13}s_{23} \\ s_{12}s_{23} - c_{12}s_{13}c_{23}e^{i\delta_{\rm CP}} & -c_{12}s_{23} - s_{12}s_{13}c_{23}e^{i\delta_{\rm CP}} & c_{13}c_{23} \end{pmatrix}, \end{aligned} \tag{2.31}$$

where $s_{ij} = \sin\theta_{ij}, c_{ij} = \cos\theta_{ij}$ *etc.* and $i, j = 1, 2, 3$. The expression for 3 flavors in vacuum can be written in the useful form in the approximation that the solar mass squared difference (Δm^2_{21}) and the mixing angle θ_{13} is small and neglected beyond 2 orders of magnitude.

$$\begin{aligned} P(\nu_\mu \to \nu_e) &= \alpha^2 \sin^2 2\theta_{12} c^2_{23} \left(\frac{\lambda L}{2}\right)^2 + 4 s^2_{13} s^2_{23} \sin^2\left(\frac{\lambda L}{2}\right) \\ &+ 2\alpha s_{13} \sin 2\theta_{13} \sin 2\theta_{23} \left(\frac{\lambda L}{2}\right) \sin\left(\frac{\lambda L}{2}\right) \cos\left(\delta_{\rm CP} + \frac{\lambda L}{2}\right), \end{aligned} \tag{2.32}$$

where $\lambda = \frac{\Delta m^2_{31}}{2E}$, $\alpha = \frac{\Delta m^2_{21}}{\Delta m^2_{31}}$. The discussion regarding the probability expressions for all other channels can be found in [102].

2.3 Neutrino oscillation in matter

Neutrinos propagating in matter are subject to coherent forward scattering with the particles present in the matter. The resulting potential changes the neutrino propagation through matter significantly than in the vacuum, thereby changing the oscillation probability expressions. The flavor changing mechanism in neutrino oscillation in presence of matter is given by the Mikheev-Smirnov-Wolfenstein (MSW) effect. The basis of the MSW effect is that the electron neutrinos have different interactions with matter than the neutrinos of other flavors. When the neutrino traverses the Earth, the oscillation probability is calculated taking into account the Earth's matter potential due to the forward scattering amplitude of charged current interactions with electrons. Neutral current interactions

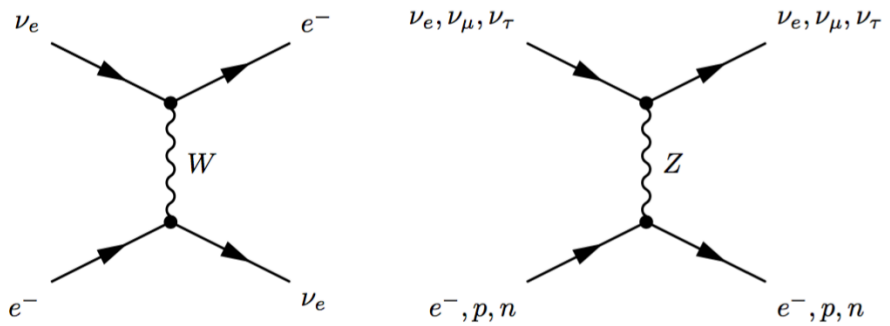

Figure 2.1: Feynman diagrams of coherent forward scattering processes that generate the charged-current potential through W exchange (left) and the neutral-current potential through the Z exchange (right).

are neglected here because they lead to flavor-independent terms which are irrelevant to the oscillation probabilities. The effective CC Hamiltonian for coherent forward elastic scattering (see figure 2.1) can be written as,

$$\begin{aligned}\mathcal{H}^{CC}_{eff}(x) &= \frac{G_F}{\sqrt{2}}\Big[\bar{\nu}_e(x)\gamma^\rho(1-\gamma^5)e(x)\Big]\Big[\bar{e}(x)\gamma_\rho(1-\gamma^5)\nu_e(x)\Big] \\ &= \frac{G_F}{\sqrt{2}}\Big[\bar{\nu}_e(x)\gamma^\rho(1-\gamma^5)\nu_e(x)\Big]\Big[\bar{e}(x)\gamma_\rho(1-\gamma^5)e(x)\Big] \quad \text{(using Fierz Transformation).}\end{aligned}$$

Averaging over the electron background in the rest frame of the medium gives

$$\bar{\mathcal{H}}^{CC}_{eff}(x) = V_{CC}\bar{\nu}_{eL}(x)\gamma^0\nu_{eL}(x), \tag{2.33}$$

with the charged current potential given by,

$$V_{CC} = \sqrt{2}G_F N_e, \quad N_e \text{ being the electron no. density of the medium.} \tag{2.34}$$

For antineutrinos, $V_{CC} \to -V_{CC}$, because of the anti-commutation relation between the creation and the annihilation operators. Similarly starting with the effective NC Hamiltonian (the right one in figure 2.1)

$$\mathcal{H}^{NC}_{eff}(x) = \frac{G_F}{\sqrt{2}}\sum_{\alpha=e,\mu,\tau}\Big[\bar{\nu}_\alpha(x)\gamma^\rho(1-\gamma^5)\nu_\alpha(x)\Big]\sum_f\Big[\bar{f}(x)\gamma_\rho(g^f_V - g^f_A\gamma^5)f(x)\Big], \tag{2.35}$$

one can see that the neutral current potential of any flavor neutrino due to coherent scattering with the fermions of the medium is given by[2],

$$V^f_{NC} = -\frac{1}{\sqrt{2}}G_F N_n. \tag{2.36}$$

[2]In an electrically neutral astrophysical environment with low temperature and density.

In summarizing, the effective neutrino potential is then given by,

$$\bar{\mathcal{H}}_{eff}(x) = \sum_{\alpha=e,\mu,\tau} V_\alpha \bar{\nu}_{\alpha L}(x)\gamma^0 \nu_{\alpha L}(x), \tag{2.37}$$

with the potential

$$V_\alpha = \sqrt{2} G_F \left(N_e \delta_{\alpha e} - \frac{1}{2} N_n \right). \tag{2.38}$$

Now, let us see how the potential affects neutrino oscillation. Going back to the evolution equation we see,

$$i\frac{d}{dt}\left|\nu_\alpha(t)\right\rangle = \mathcal{H}\left|\nu_\alpha(t)\right\rangle, \quad \text{with, } \left|\nu_\alpha(0)\right\rangle = \left|\nu_\alpha\right\rangle, \tag{2.39}$$

where $\mathcal{H}$ is the sum of the vacuum and the matter interaction Hamiltonian:

$$\mathcal{H} = \mathcal{H}_0 + \mathcal{H}_I. \tag{2.40}$$

The massive neutrino eigenstates ν_k with momentum $\vec{p}$ is an eigenstate of the vacuum Hamiltonian:

$$\mathcal{H}_0\left|\nu_k\right\rangle = E_k\left|\nu_k\right\rangle, \quad \text{with} \quad E_k = \sqrt{\vec{p}^2 + m_k^2}, \tag{2.41}$$

and the flavor states are the eigenstates of the interaction Hamiltonian:

$$\mathcal{H}_I\left|\nu_\alpha\right\rangle = V_\alpha\left|\nu_\alpha\right\rangle \quad \text{with } V_\alpha \text{ given by equation 2.38} \tag{2.42}$$

If $\psi_\alpha(t) = \langle\nu_\beta|\left|\nu_\alpha(t)\right\rangle$ is the amplitude of the transition $\nu_\alpha \to \nu_\beta$ after a time t, then its evolution can be written by (using equation 2.39 and using the approximation $t \sim x$)

$$i\frac{d}{dx}\Psi_\alpha = \mathcal{H}_F \Psi_\alpha, \tag{2.43}$$

where,

$$\mathcal{H}_F = \frac{1}{2E}(UM^2U^\dagger + A), \tag{2.44}$$

$$\Psi_\alpha = \begin{pmatrix} \psi_{\alpha e} \\ \psi_{\alpha\mu} \\ \psi_{\alpha\tau} \end{pmatrix}, \quad M^2 = \begin{pmatrix} 0 & 0 & 0 \\ 0 & \Delta m^2_{21} & 0 \\ 0 & 0 & \Delta m^2_{31} \end{pmatrix}, \quad A = \begin{pmatrix} A_{CC} & 0 & 0 \\ 0 & 0 & 0 \\ 0 & 0 & 0 \end{pmatrix},$$

$$A_{CC} = 2EV_{CC} = 2\sqrt{2}EG_F N_e$$

2.3.1 Two flavor oscillation:

For the two flavor scenario, equation 2.43 can be written as,

$$i\frac{d}{dx}\begin{pmatrix}\psi_{ee}\\ \psi_{e\mu}\end{pmatrix} = \mathcal{H}_F\begin{pmatrix}\psi_{ee}\\ \psi_{e\mu}\end{pmatrix}, \tag{2.45}$$

where

$$\mathcal{H}_F = \begin{pmatrix}-\Delta m^2\cos 2\theta + A_{CC} & \Delta m^2\sin 2\theta\\ \Delta m^2\sin 2\theta & \Delta m^2\cos 2\theta - A_{CC}\end{pmatrix}. \tag{2.46}$$

$\Delta m^2 = m_2^2 - m_1^2$ and the only mixing angle is defined as,

$$\nu_e = \nu_1\cos\theta + \nu_2\sin\theta, \quad \nu_\mu = -\nu_1\sin\theta + \nu_2\cos\theta. \tag{2.47}$$

To solve equation 2.45, $\mathcal{H}_F$ is diagonalized by the following orthogonal transformation:

$$U_M^T\mathcal{H}_F U_M = \mathcal{H}_M. \tag{2.48}$$

Here the unitary matrix U_M is the effective mixing matrix in matter:

$$U_M = \begin{pmatrix}\cos\theta_M & \sin\theta_M\\ -\sin\theta_M & \cos\theta_M\end{pmatrix}, \tag{2.49}$$

and the effective squared mass difference is

$$\Delta m_M^2 = \sqrt{(\Delta m^2\cos 2\theta - A_{CC})^2 + (\Delta m^2\sin 2\theta)^2}. \tag{2.50}$$

The effective mixing angles in matter θ_M are given by,

$$\tan 2\theta_M = \frac{\tan 2\theta}{1 - \frac{A_{CC}}{\Delta m^2\cos 2\theta}}. \tag{2.51}$$

Note that, there is a resonance when $A_{CC} = \Delta m^2\cos 2\theta$ and at the resonance the effective mixing angle is maximal *i.e.*$\pi/4$. This implies that if the resonance region is wide enough it may induce total flavor transition of neutrinos. This is the famous MSW effect [34, 35]. Proceeding further, it can now be shown that the appearance probability in presence of matter is given by (by solving equation 2.45 in a constant density *i.e.*, $d\theta_M/dx = 0$),

$$P(\nu_\mu \to \nu_e) = |\psi_{\mu e}|^2 = \sin^2 2\theta_M\sin^2\left(\frac{\Delta m_M^2 x}{4E}\right). \tag{2.52}$$

We note that this probability expression has a similar form as in vacuum (equation 2.29) with the mixing angle and the mass squared difference replaced by their matter counterparts.

2.3.2 Three flavor oscillation:

For the case of three neutrinos, the mixing matrix in the standard parametrization is (from equation 2.31)

$$U = R_{23} W_{13} R_{12}. \tag{2.53}$$

Now, since the matrix A in equation 2.44 commutes with R_{23},

$$R_{23}^{\dagger} A R_{23} = A. \tag{2.54}$$

Redefining $\Psi_\alpha \to R_{23}^{\dagger}\Psi_\alpha$ in equation 2.43 we can write,[3]

$$\begin{aligned} \mathcal{H}_F &= \frac{1}{2E}\left(W_{13} R_{12} M^2 R_{12}^{\dagger} W_{13}^{\dagger} + A\right) \\ &\approx \frac{1}{2E}\left(W_{13} M^2 W_{13}^{\dagger} + A\right) \end{aligned} \tag{2.55}$$

Now one can follow the usual procedure (as shown in subsection 2.3.1) by diagonalizing $\mathcal{H}_F$ and obtain the effective mixing angle and mass squared differences in matter as,

$$\begin{aligned} \tan 2\theta_{13}^{m} &= \frac{\tan 2\theta_{13}}{1 - \frac{A_{CC}}{\Delta m_{31}^2 \cos 2\theta_{13}}} \\ \Delta m_{m31}^2 &= \sqrt{(\Delta m_{31}^2 \cos 2\theta_{13} - A_{CC})^2 + (\Delta m_{31}^2 \sin 2\theta_{13})^2}. \end{aligned} \tag{2.56}$$

In the OMSD approximation, the expression for $P(\nu_\mu \to \nu_e)$ in matter is given by,

$$P(\nu_\mu \to \nu_e)^m = \sin^2\theta_{23} \sin^2 2\theta_{13}^{m} \sin^2\left[\Delta m_{m31}^2 L/4E\right] \tag{2.57}$$

2.4 Current status of neutrino oscillation parameters

Once the theory of neutrino oscillation had been studied extensively, experiments have been fabricated to find out the numerical values of the neutrino oscillation parameters. Standard neutrino oscillation is governed by three mixing angles ($\theta_{12}, \theta_{13}, \theta_{23}$), two mass squared differences ($\Delta m_{31}^2, \Delta m_{21}^2$), and one Dirac CP phase (δ_{CP}). Combined analyses of KamLAND [103] and the solar neutrino experiments [104] have determined the parameters θ_{12} and Δm_{21}^2. The atmospheric neutrino experiments such as Super-Kamiokande (SK) [31], MINOS [31,105] have measured $\sin^2 2\theta_{23}$ and $|\Delta m_{31}^2|$. The short baseline reactor neutrino experiments Daya Bay [106], RENO [107], and Double Chooz [108] have recently

[3] We also make use of the One Mass Squared Dominance (OMSD) approximation $\Delta m_{31}^2 >> \Delta m_{21}^2$ and $M \approx diag(0, 0, \Delta m_{31}^2)$

evaluated the non-zero value of θ_{13} very precisely. The ongoing and the upcoming accelerator long-baseline neutrino experiments (T2K [109], NOvA [110,111], DUNE [112,113], T2HK [114]) are expected to probe the precise value of Δm^2_{31} (with correct sign), $\delta_{\rm CP}$ and θ_{23}. The present status of the oscillation parameters is shown in table 2.1.

Parameter	Best-fit-value	3σ interval	1σ uncertainty
θ_{12} [Deg.]	34.3	31.4 - 37.4	2.9%
θ_{13} (NH) [Deg.]	8.58	8.16 - 8.94	1.5%
θ_{13} (IH) [Deg.]	8.63	8.21 - 8.99	1.5%
θ_{23} (NH) [Deg.]	48.8	41.63 - 51.32	3.5%
θ_{23} (IH) [Deg.]	48.8	41.88 - 51.30	3.5%
Δm^2_{21} [eV^2]	7.5×10^{-5}	[6.94 - 8.14]$\times 10^{-5}$	2.7%
Δm^2_{31} (NH) [eV^2]	$+2.56 \times 10^{-3}$	[2.46 - 2.65] $\times 10^{-3}$	1.2%
Δm^2_{31} (IH) [eV^2]	-2.46×10^{-3}	-[2.37 - 2.55]$\times 10^{-3}$	1.2%
δ_{13} (NH) [Rad.]	-0.8π	$[-\pi, 0] \cup [0.8\pi, \pi]$	–
δ_{13} (IH) [Rad.]	-0.46π	$[-0.86\pi, -0.1\pi]$	–

Table 2.1: Standard oscillation parameters and their uncertainties used in our study. The values were taken from the global fit analysis in [115]. If the 3σ upper and lower limit of a parameter is x_u and x_l respectively, the 1σ uncertainty is $(x_u - x_l)/3(x_u + x_l)\%$ [116].

Chapter 3

Exploring the new physics phases in $3+1$ scenario in neutrino oscillation experiments

3.1 Introduction

The phenomenon of standard three-neutrino oscillation [32, 51] (cited as $3+0$ hereafter) has been consolidated through significant experimental data with solar, reactor, accelerator, or atmospheric neutrinos over a long-range of energy (E) and baseline (L). Despite the remarkable success of the $3+0$ picture, there are a few anomalies, namely, LSND and MiniBooNE anomalies. LSND detected 3.8σ event excess in the $\bar{\nu}_e$ channel and MiniBooNE observed 4.5σ event excess in ν_e channel. These results could not be explained in the framework of standard three-neutrino oscillation. There are several possible explanations for these SBL anomalies, such as the decay of heavy ($\mathcal{O}$(keV)) sterile neutrinos to active neutrinos [117], new resonance matter effects [118], decay of axion-like particles [119] *etc.* Mixing of one light sterile neutrino ($\mathcal{O}$(eV)) with the active neutrinos through oscillation is one of them [120]. This particular theory of one additional sterile neutrino in the oscillation picture (referred to as $3+1$ hereafter) improves the accuracy by 5σ [121] and this is unlikely to be a random advancement. Various existing and future facilities aim to search for sterile neutrinos with high precision using different neutrino sources and detection techniques. These facilities include IceCube [122], Karlsruhe Tritium Neutrino Experiment (KATRIN) [123], FermiLab's Short Baseline Neutrino (SBN) program [124], ANTARES [89], Neutrino Experiment for Oscillation at Short baseline (NEOS) [125], Short baseline neutrino Oscillations with a novel Lithium-6 composite scintillator Detector(SoLid) [126], Neutrino-4 [127], Precision Reactor Oscillation and SPECTrum Ex-

periment (PROSPECT) [128], Sterile Reactor Neutrino Oscillations (STEREO) [129, 130], Detector of the reactor AntiNeutrino based on Solid Scintillator (DANSS) [131], J-PARC Sterile Neutrino Search at J-PARC Spallation Neutron Source(JSNS^2) [132, 133].

The large splittings ($O(1\ \text{eV}^2)$ mass-squared splittings that are much larger than the two splittings of the standard paradigm) hinted at by the short-baseline anomalies imply the existence of additional, largely sterile, neutrino mass eigenstates, beyond the three of the standard scenario. These additional mass eigenstates introduce not only additional splittings but also additional mixing angles and phases. For simplicity, we restrict ourselves to the scenario, referred to as 3+1, with only one additional mass eigenstate. In this scenario, there are six mixing angles (the standard $3+0$ mixing angles $\theta_{12}, \theta_{23}, \theta_{13}$, and the $3+1$ mixing angles $\theta_{14}, \theta_{24}, \theta_{34}$) and three CP-violating phases that can affect oscillation. The standard Dirac CP phase is associated with the $1-3$ mixing angle in the standard parametrization and thus, δ_{13}. For the $3+1$ scenario, we have chosen the two additional phases with the $2-4$ and $3-4$ mixing angles. The new 4×4 mixing matrix will have the form:

$$U^{3+1} = R(\theta_{34}, \delta_{34})R(\theta_{24}, \delta_{24})R(\theta_{14})R(\theta_{23})R(\theta_{13}, \delta_{13})R(\theta_{12}),$$

where $R_{ij}(\theta_{ij}, \delta_{ij})$ denotes the rotation in ij-th plane. Denoting the mass eigenstates of 3+0, as usual, as ν_1, ν_2, ν_3, and the additional mass eigenstate as ν_4, and defining the mass-squared splittings as $\delta m^2_{ij} = m^2_i - m^2_j$ (i, j = 1, 2, 3, 4 & $i \neq j$), we have, according to the present data,

$$\delta m^2_{41} \sim \delta m^2_{42} \sim \delta m^2_{43} >> |\delta m^2_{31}| \sim |\delta m^2_{32}| >> \delta m^2_{21}. \tag{3.1}$$

The presence of sterile neutrino in nature is going to impact the physics searches in the long-baseline (LBL) experimental data if the interference terms arising due to the additional CP phases are not accounted for properly. The impact of the presence of sterile neutrino is more pronounced around $L/E \sim 500$ km/GeV at the far detectors (FD) in the case of LBL experiments. It has been shown [134–157] that even at the FDs of these LBL experiments, the interference effects provided by the additional CP phases play very significant roles in spoiling the sensitivities to the crucial issues of CPV, MH and θ_{23} octant. But the bound on the allowed region of the active-sterile mixing angles θ_{i4} ($i = 1, 2, 3$) reduces the uncertainty in interpreting the ambiguities in the result obtained. The search for the origin of CP violation has been discussed in presence of a sterile neutrino in [141]. Here, χ^2 analysis has been done to study how precisely the DUNE experiment can put a bound on δ_{24} (or, δ_{14}, depending on the parametrization). But the CP phase δ_{34} and its correlation with other phases have been discussed less. In [148] it has been discussed how

the Δm^2_{41} driven oscillations are averaged out at the LBL experiments and δ_{24} is probed mainly through matter oscillations but it is comparatively cumbersome to put a bound on δ_{34}.

In this chapter, we aim to study that if sterile neutrino exists in nature, how precisely the ongoing and future experiments will be able to measure the CP phases. The precise value of the CP phases will give a measurement of leptonic CP violation which in turn may answer the long-standing question of matter-antimatter asymmetry in the universe. We have carried out this exercise in the context of DUNE experiment and eventually incorporated data from T2K, NOvA, and T2HK experiments. The T2HK projected data having larger statistics is expected to give improved results. In addition to that, we have also incorporated the tau appearance channel as a signal (otherwise, mostly considered as background) in our study. Lastly, we have briefly explored how the parameter space of the neutrinoless double beta decay phenomenon gets affected by the presence of one eV scale sterile neutrino.

3.1.1 Method of χ^2 analysis:

The calculation of χ^2 gives the measure of the validity of some theoretical hypothesis against a set of experimental data. To put it simply, χ^2 measures the amount of *deviation* between the following two datasets:

1. The dataset produced by the actual experiment - called the *true* or simply *data*.

2. The dataset assuming the theoretical hypothesis - called the *test* or *fit*.

The computation of χ^2 for a fixed set of parameters (test) is performed using the method of pulls [158–161]. This method allows us to take into account the various statistical and systematic uncertainties in a straightforward way. The flux, cross-sections and other systematic uncertainties are included by allowing these inputs to deviate from their standard values in the computation of the expected (test) event rate in the particular bin. The analytical form is given as:

$$\Delta\chi^2(p^{\text{true}}) = \underset{p^{\text{test}},\eta}{\text{Min}}\Bigg[2\sum_{k}^{\text{mode}}\sum_{j}^{\text{channel}}\sum_{i}^{\text{bin}}\Bigg\{N^{\text{test}}_{ijk}(p^{\text{test}};\eta) - N^{\text{true}}_{ijk}(p^{\text{true}}) + N^{\text{true}}_{ijk}(p^{\text{true}})\ln\frac{N^{\text{true}}_{ijk}(p^{\text{true}})}{N^{\text{test}}_{ijk}(p^{\text{test}};\eta)}\Bigg\} + \sum_{l}\frac{(p^{\text{true}}_l - p^{\text{test}}_l)^2}{\sigma^2_{p_l}} + \sum_{m}\frac{\eta^2_m}{\sigma^2_{\eta_m}}\Bigg]. \quad (3.2)$$

The superscripts *true* and *test* stands for the *true* and *test* data sets, respectively. N denotes the event numbers and p stands for the set of oscillation parameters. The *true* or best-fit values and the corresponding uncertainties of the oscillation parameters are tabulated in Table 3.1. The indices *i*, *j*, *k* denote the energy bins, oscillation channels ($\nu_\mu \to \nu_e, \nu_\mu \to \nu_\mu, \nu_\mu \to \nu_\tau$), and corresponding the modes (ν and $\bar{\nu}$), respectively. The energy bins vary from experiment to experiment and that has been efficiently taken care of by GLoBES through the plugin *snu.c* [162, 163]. The plugin *snu.c* takes care of the new physics phenomenon beyond the three-neutrino oscillation framework in GLoBES. It handles the extension of the oscillation parameter space in presence of another sterile neutrino as well as non-standard interaction terms for neutrinos.

Uncertainties in the prior measurement of the l^{th} oscillation parameter are given by the parameters σ_{pl}. η_m is the nuisance parameter and σ_{η_m} is the corresponding uncertainty. Now, let us go through equation 3.2 term by term. The first term ($N^{test} - N^{true}$) accounts for the algebraic difference between the two sets of event numbers, whereas, the log-term gives the fractional difference. The entire expression in the curly brackets consists of the statistical part of the $\Delta\chi^2$ calculation. The term summed over l takes care of the uncertainties in the oscillation parameter space and the last term (summed over m) is the systematic part.

3.1.2 Simulation details:

We simulate the long baseline neutrino experiments DUNE, NOvA, T2K, and T2HK using GLoBES [164, 165]. DUNE is a 1300 km long baseline experiment employing a liquid argon far detector (FD) of 40 kt fiducial mass with a beam of power 1.07 MW and running 3.5 years each on ν and $\bar{\nu}$ mode (resulting in a total exposure of roughly 300 kt.MW.yr corresponding to 1.47×10^{21} protons on target or POT). We have used the official configuration files [166] provided by the DUNE collaboration for its simulation. Following this, we have also taken into account the presence of a near detector (ND) at 459 m from the source. The ND helps in making a more precise measurement of the flux and cross-section, thereby reducing the relevant systematic uncertainties at the FD. We should mention here that we have done a χ^2 analysis (discussed later) with the simulated data at FD alone, rather than a joint χ^2 analysis using simulated data both at ND and FD[1]. Electron

[1]It is worthwhile to note here that an eV-scale sterile neutrino will have its signature at the ND due to short baseline active-sterile oscillation and consequently a joint analysis using both ND and FD data would probably constrain the active-sterile mixing angles slightly more. But our main aim is the analyses of the CP phases, given the already existing constraints on the mixing angles from the global analysis [167], and

neutrino appearance signals (CC), muon neutrino disappearance signals (CC), as well as neutral current (NC) backgrounds and tau neutrino appearance backgrounds (along with the corresponding systematics/efficiencies *etc.*) are already included in the configuration files.

In the present analysis, we have additionally incorporated tau neutrino appearance as a separate signal following [152, 153]. Charged current interaction of an incoming ν_τ produces a τ lepton (requires a threshold energy of $\gtrsim 3.4$ GeV for the incoming ν_τ), which can decay hadronically (with a branching fraction $\sim 65\%$) or leptonically (with a branching fraction of $\sim 35\%$). The analysis of the hadronic decay channel involves the capability of the detector to study the resulting pions and kaons. More importantly, NC neutrino scattering constitutes the biggest background for the hadronic decay channel of τ. Following [152], we have used an efficiency to separate 30% hadronically decaying τ events (with about 1% NC events remaining). On the other hand, the leptonic decay channels of τ ($\tau^- \to e^- \bar{\nu}_e \nu_\tau$; $\tau^- \to \mu^- \bar{\nu}_\mu \nu_\tau$) are more difficult to analyse, due to the large background mainly consisting of ν_e-CC and ν_μ-CC respectively (along with backgrounds from NC and contaminations due to wrong sign leptons.). Following [153], we have taken the efficiency of the electron channel to be 15%. Due to the overwhelming background, we have taken a nominal efficiency of 5% in the muon channel. Naturally, the contribution of the leptonic decay channel of τ is very small. We should also mention here that the decay of τ at the detector will involve missing energy in the form of an outgoing ν_τ, which in turn makes the energy reconstruction of the incoming ν_τ difficult. From [152], we use a Gaussian energy reconstruction with a resolution of 20% which is a conservative estimate. We acknowledge that our implementation of the ν_τ channel as a signal is conservative in nature. Nevertheless, this provides small but non-negligible statistics in terms of events and χ^2 sensitivity. Using a much more sophisticated analysis of ν_τ appearance channel at DUNE by implementing jet- clustering algorithms and machine learning techniques, as has been pioneered in [168], one certainly expects to exploit the rich physics capabilities hidden within this channel.

We have simulated NOvA with a baseline of 800 km employing an FD of fiducial mass of 14 kt and a beam of 742 kW. The simulation for NOvA was implemented according to [169] which generates 8.85×10^{20} (12.33×10^{20}) POT in ν ($\bar{\nu}$) mode. T2K is a 295 km experiment with a 22.5 kt water Cherenkov FD. For T2K simulation we use the inputs from [70, 170]. We have used a beam of 515 kW and simulating 1.97×10^{21} (1.63×10^{21})

this would have more observable signals at the FD, especially in neutrino appearance measurements [136]

POT in ν ($\bar{\nu}$) mode. T2HK is an *upgraded* version of T2K with a higher beam of 1.3 MW and a much bigger fiducial mass of 187 kt of its water Cherenkov FD. For T2HK we simulate a total of 2.7×10^{22} POT in 1:3 ratio of ν and $\bar{\nu}$ mode (with inputs taken from [171, 172]). Note that, for the future experiments DUNE and T2HK we have used the full expected exposure, while for the currently running experiments T2K and NOvA we have simulated up to their current exposure.

3.2 Effect of new CP phases on probabilities

In the current analysis, we are trying to find out the effect of the CP phases in LBL experiments. Our initial motivation is to derive the form of the probabilities ($P(\nu_\mu \to \nu_e)$, $P(\nu_\mu \to \nu_\mu)$, and $P(\nu_\mu \to \nu_\tau)$) in an added sterile flavor picture in the neutrino sector. The expression for these probabilities in presence of matter becomes extremely cumbersome, hence, we have presented the analytical form of the same in vacuum to get hold of the understanding of the underlying physics and to draw a conclusion of the results as we move further. The first notable change comes in terms of the mixing matrix and we have adopted the following parametrization [136]:

$$U^{3+1} = R(\theta_{34}, \delta_{34})R(\theta_{24}, \delta_{24})R(\theta_{14})R(\theta_{23})R(\theta_{13}, \delta_{13})R(\theta_{12}), \tag{3.3}$$

where $R(\theta_{ij}, \delta_{ij})$ is a rotation in the $ij-$th plane with an associated phase δ_{ij} such that, for *e.g.*,

$$R(\theta_{34}, \delta_{34}) = \begin{pmatrix} 1 & 0 & 0 & 0 \\ 0 & 1 & 0 & 0 \\ 0 & 0 & \cos\theta_{34} & e^{-i\delta_{34}}\sin\theta_{34} \\ 0 & 0 & -e^{i\delta_{34}}\sin\theta_{34} & \cos\theta_{34} \end{pmatrix}. \tag{3.4}$$

The mixing matrix introduces three new mixing angles and two new CP phases. By analyzing data from several neutrino experiments [167] bounds on the values of these parameters have been estimated. We start from the term U_{e4} element in the 4×4 mixing matrix which can be bounded by the ν_e and $\bar{\nu}_e$ disappearance channels. We have found that combined atmospheric data from IceCube, DeepCore, and SK, at 99% C.L. (2 DOF) give us $|U_{e4}|^2 \lesssim 0.1$ (which implies $\theta_{14} \lesssim 18.4°$). Whereas, the best-fit value is: $|U_{e4}|^2 \approx 0.01$, which gives $\theta_{14} \approx 5.7°$. The muon disappearance channels (both ν and $\bar{\nu}$) put constraints on $|U_{\mu 4}|(= \cos\theta_{14}\sin\theta_{24})$ and $|U_{\tau 4}|(= \cos\theta_{14}\cos\theta_{24}\sin\theta_{34})$. Data from these disappearance searches give the following bounds at 99% C.L. (2 D.O.F.): $|U_{\mu 4}|^2 \lesssim 0.01$ and $|U_{\tau 4}|^2 \lesssim 0.17$ which translates into $\theta_{24} \lesssim 6.05°$ and $\theta_{34} \lesssim 25.8°$, respectively. The allowed value for

Δm^2_{41} lies in the range $1 - 10\ eV^2$ and we take it to be $1.3\ eV^2$ as per global analysis in the current work.

Now we follow the prescription in section [2.1] and arrive at the oscillation probability for the transition $\nu_\alpha \to \nu_\beta (\alpha, \beta = e, \mu, \tau, s$ and $\alpha \neq \beta)$ in $3+1$ scenario.

$$\begin{aligned} P^{3+1}_{\alpha\beta} &= 4|U_{\alpha4}U_{\beta4}|^2 \times 0.5 \\ &- 4\text{Re}(U_{\alpha1}U^*_{\beta1}U^*_{\alpha2}U_{\beta2}) \sin^2\Delta_{21} + 2\text{Im}(U_{\alpha1}U^*_{\beta1}U^*_{\alpha2}U_{\beta2}) \sin 2\Delta_{21} \\ &- 4\text{Re}(U_{\alpha1}U^*_{\beta1}U^*_{\alpha3}U_{\beta3}) \sin^2\Delta_{31} + 2\text{Im}(U_{\alpha1}U^*_{\beta1}U^*_{\alpha3}U_{\beta3}) \sin 2\Delta_{31} \\ &- 4\text{Re}(U_{\alpha2}U^*_{\beta2}U^*_{\alpha3}U_{\beta3}) \sin^2\Delta_{32} + 2\text{Im}(U_{\alpha2}U^*_{\beta2}U^*_{\alpha3}U_{\beta3}) \sin 2\Delta_{32}, \end{aligned} \tag{3.5}$$

where $\Delta_{ij} = \frac{\Delta m^2_{ij} L}{4E}$. In this exercise, it has been assumed that the 4×4 mixing matrix is unitary and the term containing mass square splitting between m_4 and m_i $(i = 1, 2, 3)$, *i.e.*, $\sin^2\Delta_{4i}$ and $\sin 2\Delta_{4i}$ average out to 0.5 and 0, respectively at long baseline $(i = 1, 2, 3)$. Moreover, in long-baseline experiments, the effects due to Δm^2_{21} on the oscillation are negligible. Using these assumptions we have derived the analytical form of the dominant oscillation channel $\nu_\mu \to \nu_e$:

$$\begin{aligned} P^{4\nu}_{\mu e} \approx& \frac{1}{2}\sin^2 2\theta^{4\nu}_{\mu e} \\ &+ (a^2 \sin^2 2\theta^{3\nu}_{\mu e} - \frac{1}{4}\sin^2 2\theta_{13} \sin^2 2\theta^{4\nu}_{\mu e}) \sin^2\Delta_{31} \\ &+ \cos(\delta_{13} + \delta_{24}) a \sin 2\theta^{3\nu}_{\mu e} \sin 2\theta^{4\nu}_{\mu e} \cos 2\theta_{13} \sin^2\Delta_{31} \\ &+ \sin(\delta_{24}) ba \sin 2\theta^{4\nu}_{\mu e} \sin^2\theta_{13} \sin 2\Delta_{31} \\ &+ \frac{1}{2}\sin(\delta_{13} + \delta_{24}) a \sin 2\theta^{3\nu}_{\mu e} \sin 2\theta^{4\nu}_{\mu e} \sin 2\Delta_{31}, \end{aligned} \tag{3.6}$$

where we have followed the convention of [136] for the following quantities.

$$\begin{aligned} \sin 2\theta^{3\nu}_{\mu e} &= \sin 2\theta_{13} \sin\theta_{23}, \\ b &= \cos\theta_{13} \cos\theta_{23} \sin 2\theta_{12}, \\ \sin 2\theta^{4\nu}_{\mu e} &= \sin 2\theta_{14} \sin\theta_{24}, \\ a &= \cos\theta_{14} \cos\theta_{24}. \end{aligned}$$

Equation 3.6 tells us that in vacuum $P(\nu_\mu \to \nu_e)$ is sensitive to both δ_{13} and δ_{24}, but not to δ_{34}. As explained in [136], small dependence on δ_{34} creeps in when matter effect is taken into account. The expressions for the less dominant channels $P(\nu_\mu \to \nu_\mu)$ and $P(\nu_\mu \to \nu_\tau)$ can similarly be derived from equation 3.5. We have implemented General Long Baseline Experiment Simulator (GLoBES) [164, 165] and the relevant plugin

Parameter	Best-fit-value	3σ interval	1σ uncertainty
θ_{12} [Deg.]	34.3	31.4 - 37.4	2.9%
θ_{13} (NH) [Deg.]	8.58	8.16 - 8.94	1.5%
θ_{13} (IH) [Deg.]	8.63	8.21 - 8.99	1.5%
θ_{23} (NH) [Deg.]	48.8	41.63 - 51.32	3.5%
θ_{23} (IH) [Deg.]	48.8	41.88 - 51.30	3.5%
Δm^2_{21} [eV^2]	7.5×10^{-5}	[6.94 - 8.14]$\times 10^{-5}$	2.7%
Δm^2_{31} (NH) [eV^2]	$+2.56 \times 10^{-3}$	[2.46 - 2.65] $\times 10^{-3}$	1.2%
Δm^2_{31} (IH) [eV^2]	-2.46×10^{-3}	-[2.37 - 2.55]$\times 10^{-3}$	1.2%
δ_{13} (NH) [Rad.]	-0.8π	$[-\pi, 0] \cup [0.8\pi, \pi]$	–
δ_{13} (IH) [Rad.]	-0.46π	$[-0.86\pi, -0.1\pi]$	–
θ_{14} [Deg.]	5.7, 10	0 - 18.4	$\sigma(\sin^2\theta_{14}) = 5\%$
θ_{24} [Deg.]	5, 6	0 - 6.05	$\sigma(\sin^2\theta_{24}) = 5\%$
θ_{34} [Deg.]	20, 25	0 - 25.8	$\sigma(\sin^2\theta_{34}) = 5\%$
δ_{24} [Rad.]	$0, -0.5\pi$	$[-\pi, \pi]$	–
δ_{34} [Rad.]	$0, -0.5\pi$	$[-\pi, \pi]$	–

Table 3.1: Standard oscillation parameters and their uncertainties were used in our study. The values of 3+0 parameters were taken from the global fit analysis in [115] while the 3+1 parameter values were chosen from [167]. If the 3σ upper and lower limit of a parameter is x_u and x_l, respectively, the 1σ uncertainty is $(x_u - x_l)/3(x_u + x_l)\%$ [116]. For the active-sterile mixing angles, a conservative 5% uncertainty was used on $\sin^2\theta_{i4}$ (i = 1, 2, 3).

snu.c [162, 163] to derive the probabilities for different oscillation channels in the case of DUNE experiment (baseline length 1300 km). The results are shown in figure 3.1 where we have plotted the bands by varying $\delta_{13}, \delta_{24}, \delta_{34}$ in the range $[-\pi, \pi]$ for three oscillation channels ($P_{\mu e}, P_{\mu\mu}, P_{\mu\tau}$) in three consecutive panels. The grey, blue and red band manifest the effect of variation of the standard Dirac CP phase δ_{13}, new sterile CP phases δ_{24} and δ_{34}, respectively. We have kept the values of the active-sterile mixing angles constant at $\theta_{14} = 10°, \theta_{24} = 6°, \theta_{34} = 25°$ which are slightly higher. While varying each CP phase we have kept the values of other two phases constant at $\delta_{13} = -0.8\pi$ (the current best-fit value), $\delta_{24} = 0$ and $\delta_{34} = 0$. Now in figure 3.1 (A), the $\nu_\mu \to \nu_e$ channel is most affected by δ_{13} and the effect of the sterile phase δ_{24} is slightly larger than that of δ_{34} as we can see from equation 3.6 that the impact of δ_{34} only comes from matter effect. In figure 3.1 (B),

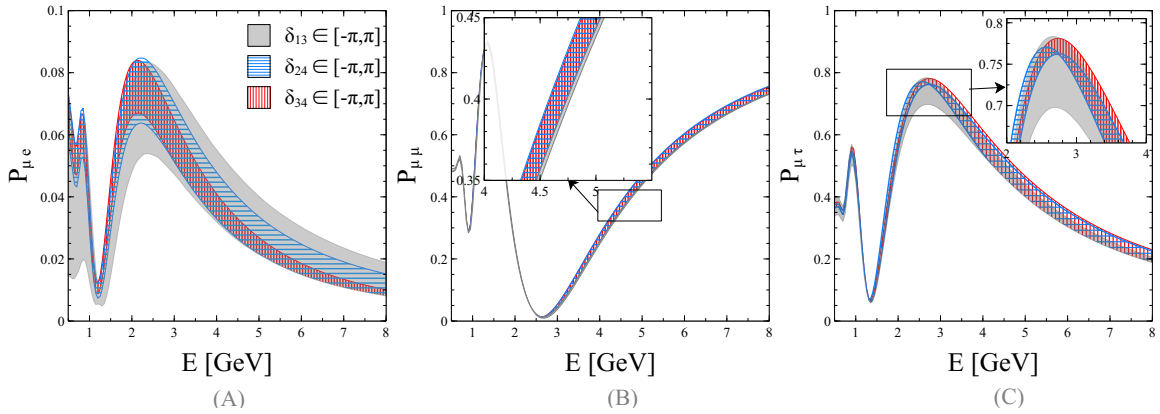

Figure 3.1: We show the probability bands due to individual variation of the CP phases δ_{13} (grey), δ_{24} (blue), and δ_{34} (red) in the whole range of $[-\pi, \pi]$ at a baseline of 1300 km. The three panels correspond to the three channels $P(\nu_\mu \to \nu_e), P(\nu_\mu \to \nu_\mu)$ and $P(\nu_\mu \to \nu_\tau)$. The insets in panels (A) and (B) show magnified versions of the rectangular regions indicated. The three active-sterile mixing angles were taken as $\theta_{14} = 10°, \theta_{24} = 6°, \theta_{34} = 25°$. The values of the rest of the oscillation parameters were taken from table 3.1. The normal hierarchy was assumed for generating this plot.

we can see that the effect of CP phases are minimal in the case of $P(\nu_\mu \to \nu_\mu)$. $P(\nu_\mu \to \nu_\tau)$, on the other hand, is more prone to the variation of δ_{13} in comparison to the disappearance channel. As expected[2], the CP phases have a larger impact on appearance channels in comparison to the disappearance channels.

3.3 Correlation among the new CP phases

In this work, we have estimated how efficiently all the CP phases (δ_{13}, δ_{24} and δ_{34}) can be reconstructed considering their $\Delta\chi^2$ correlation with each other. Figure 3.2 shows the reconstruction of the CP phases at 1σ C.L. in the (test δ_{13} - test δ_{24}), (test δ_{13} - test δ_{34}) and (test δ_{24} - test δ_{34}) planes, respectively. The red contours depict the reconstruction capability of DUNE experiment. The green and blue contours show the reconstruction capability when data from T2K & NOνA, and T2K, NOνA & T2HK are combined with DUNE data, respectively. The top and bottom row manifest the two sets of choices for the *true* values of the new sterile CP phases (δ_{24} and δ_{34}): in the top row, we have taken the CP conserving scenario, whereas, in the bottom row we have taken the maximal CP violating scenario. The *test* values of the poorly measured oscillation parameters, $\theta_{13}, \theta_{23}, \Delta m^2_{31}$ (for both the mass hierarchies), have been marginalized with prior and uncertainties mentioned in table 3.1. Also, *test* values of the active-sterile mixing angles $\theta_{i4} (i = 1, 2, 3)$ and the third CP

[2]In equation 3.5 for $\alpha = \beta$, the imaginary part in the RHS vanishes, diminishing the effect of the CP phases.

phase absent in each plane have also been considered for marginalisation.

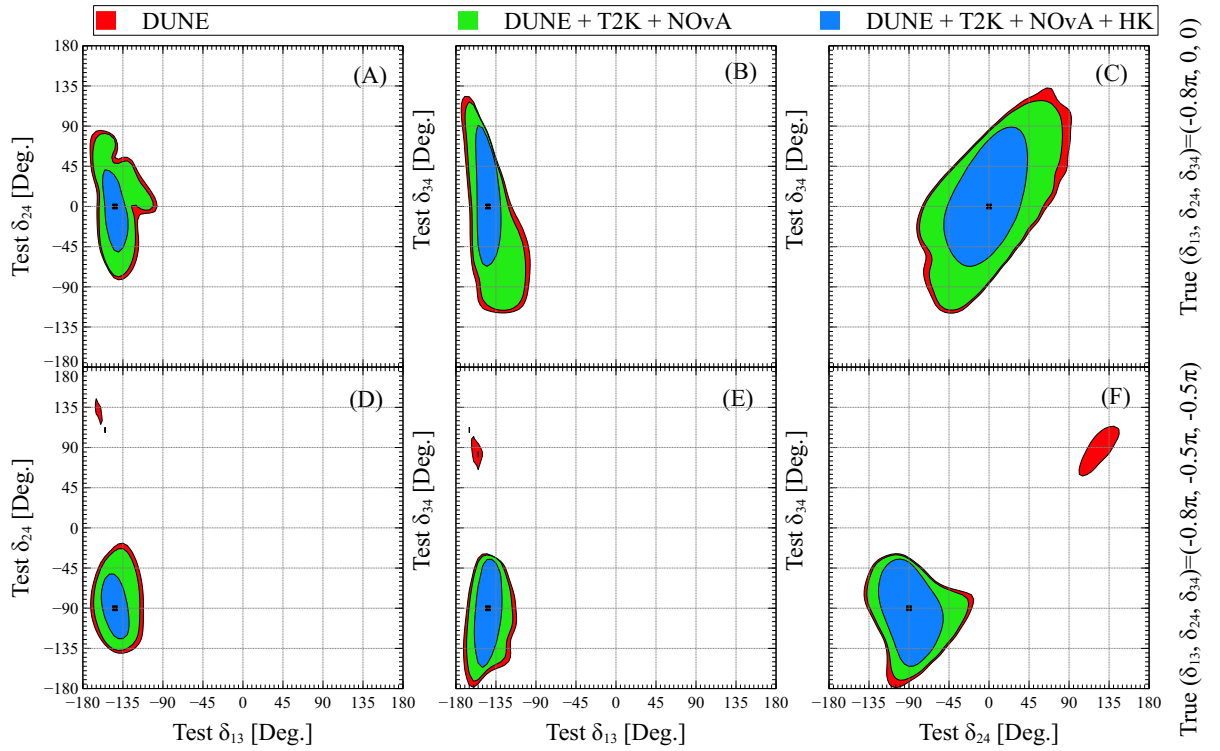

Figure 3.2: Reconstruction of the CP phases, taken pairwise at a time, at a C.L. of 1σ (2 D.O.F.) at DUNE (red), DUNE + T2K + NOvA (green), and DUNE + T2K + NOvA + T2HK (blue). The top (bottom) row corresponds to the choice $\delta_{24} = \delta_{34} = 0$ $(-\pi/2)$. The true value of the standard Dirac CP phase δ_{13} is fixed at -0.8π. The black dot indicates the true values assumed. The true values of active-sterile mixing angles are taken as $\theta_{14}, \theta_{24}, \theta_{34} = 5.7°, 5°, 20°$. Other oscillation parameters were taken from table 3.1.

The reconstruction of the CP phases largely depends on the precision of the measurement of the corresponding mixing angle and among the three mixing angles in question θ_{13} has been measured very precisely. It is also evident from the contours as they are narrower along the *test* δ_{13} axis in comparison to the other two phases. For the maximally CP violating choices of true δ_{24} and true δ_{34}, their reconstruction gets better at the cost of small degeneracies appearing for DUNE around test $\delta_{24} \approx 135°$, $\delta_{34} \approx 90°$. But as we incorporate data points from several experiments (T2K, NOvA & T2HK) the degeneracies are lifted.

In figure 3.3 we have shown how efficiently the long baseline experimental data can reconstruct the CP phases at 1σ C.L. Here, individually, all possible *true* values of the CP phases have been varied in the whole parameter space ($\in [-\pi, \pi]$). The three columns show the reconstruction of the three CP phases and the *true* and *test* values along the axes. The top and bottom row manifests the difference in reconstruction in the case of the

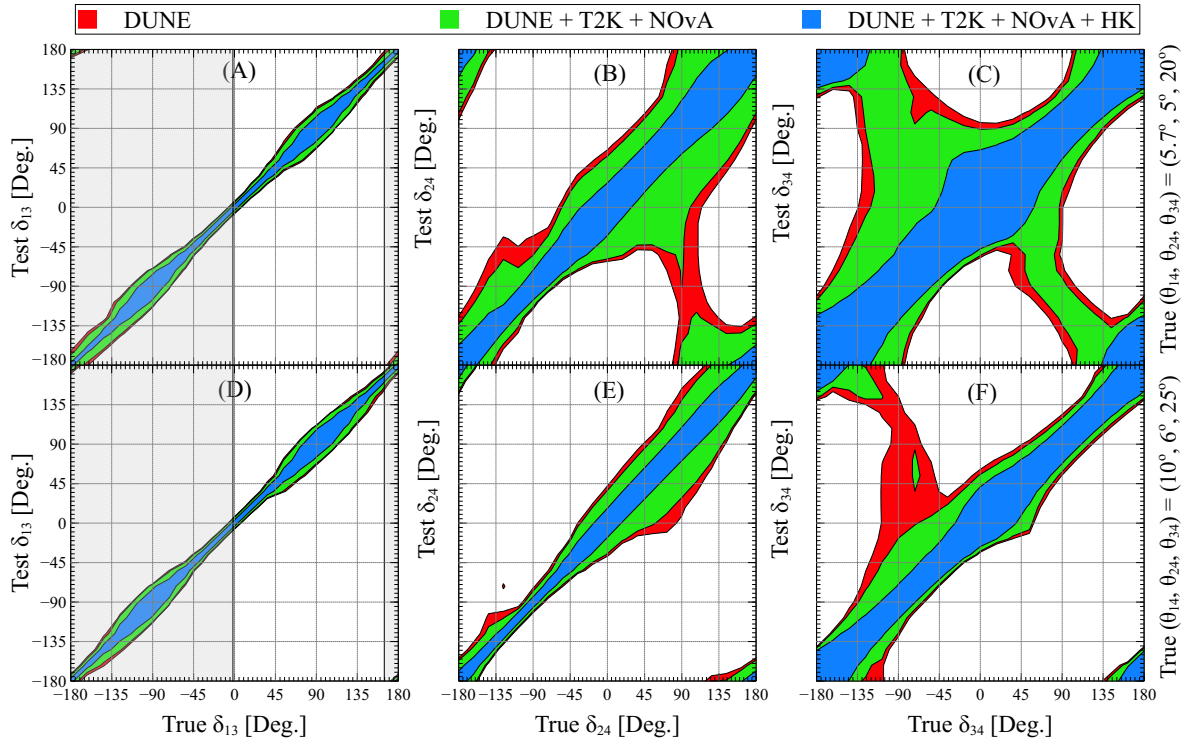

Figure 3.3: Reconstruction of the CP phases δ_{13}, δ_{24} and δ_{34}, for all the choices of their true values in $[-\pi, \pi]$ at a C.L. of 1σ (1 D.O.F.) at DUNE (red), DUNE + T2K + NOvA (green), and DUNE + T2K + NOvA + T2HK (blue). The top (bottom) row corresponds to the choice of the active-sterile mixing angles as true $\theta_{14}, \theta_{24}, \theta_{34} = 5.7°, 5°, 20°$ $(10°, 6°, 25°)$. The true values of the phases not shown in a panel are fixed at: δ_{13}, δ_{24} and $\delta_{34} = -0.8\pi, 0$ and 0, respectively. In the first column, the grey shaded regions depict the 3σ allowed values measured by T2K [170].

true values of the smaller and larger active-sterile mixing angles, respectively. The choices have been made in line with the limits on the parameter space discussed in section 3.2. Marginalization has been done in each panel over *test* values of the above-mentioned parameters (*i.e.*, $\theta_{13}, \theta_{23}, \Delta m^2_{31}, \theta_{14}, \theta_{24}, \theta_{34}$) and also over the two CP phases not shown in the axes over the entire parameter space. For each *true* value of the CP phase marked on X-axis the vertical width of the contour gives an estimation of how precisely the reconstruction can be done. In the first column, we can see that LBL experiments can reconstruct δ_{13} much more efficiently in comparison to δ_{24} and δ_{34}. This is also indicated in figure 3.1 left column where we can see that electron appearance channel is more sensitive to the variation of δ_{13} and least sensitive to δ_{34}. The reconstruction of δ_{13} doesn't vary much in the case of smaller or larger active-sterile mixing mentioned in the two rows, respectively. Now, T2K data [170] indicates that the allowed region for δ_{13} is $[-\pi, 0]$ (shaded in grey in the left column) with a best-fit value around the maximal CP violating value ($\approx -\pi/2$).

In case this holds true, future analyses done with a combination of (DUNE, NOvA T2K, T2HK) with the proposed runtime will be able to do a more precise approximation in the range of $[-115°, -75°]$ at 1σ C.L. The reconstruction is slightly better closer to the *true* value $\delta_{13} = 0°$ which is the CP conserving value. The middle and right column shows significant change in the reconstruction for the smaller and larger values of the active-sterile mixing angle. A larger mixing angle leads to a better sensitivity in the measurement of δ_{24} and δ_{34} in the case of LBL experiments. It should also be noted that the sterile phase δ_{24} is reconstructed with more precision in comparison to δ_{34}. In the top row of figure 3.3 without considering the T2HK-projected data, δ_{24} shows better reconstruction in the lower half region (*i.e.*, $[0, \pi]$) but in the upper half region, the values are unbounded. The T2HK experiment can provide larger statistics due to a shorter baseline and larger fiducial mass of the water Cerenkov detector. Hence, the addition of T2HK-projected data phenomenally changes the reconstruction in the entire parameter space. In the right column, the reconstruction scenario for δ_{34} is poor for both choices of the active-sterile mixing angles in absence of T2HK-projected data. For *e.g.*, the combination of DUNE, NOvA and T2K simulated data fails to put any bound on the reconstructed value of δ_{34} at 1σ C.L. in the range $[-135°, -90°]$ for smaller values of the mixing angles (top row). But clearly, the degeneracies can be alleviated with more statistics from the future experimental data.

3.4 Effect of different channels

In this section, we will discuss how different channels can impact the reconstruction of the CP phases in LBL experiments. Here we have just considered the simulated data from DUNE experiment and aimed to reconstruct the CP phases pairwise (as done in figure 3.2) at 1σ C.L. The cyan contour in figure 3.4 gives the uncertainty in the measurement of the phases for the data in the electron appearance channel. Reconstruction gets improved as the tau appearance channel and muon disappearance channels are added as shown in grey and red contours, respectively. The red contours in all three panels are identical to those on the top row of figure 3.2. In the case of δ_{13} reconstruction, the addition of channels doesn't improve the bound much which in turn consolidates the contribution of ν_e channel in the said measurement. We can see from figure 3.1 (C), that in the case of the tau appearance channel, the dependence of the phase δ_{34} is significant. But in the current experiments, there are larger uncertainties in the case of ν_τ events in comparison to ν_μ events. As a consequence, in the case of figure 3.4 (B), we can see that the bounds on the reconstruction of δ_{34} don't improve at χ^2 level by the addition of $\nu_\mu \to \nu_\tau$ channel.

Whereas, in figure 3.4 (C), the grey contour shows a slight improvement in the reconstruction of δ_{34} by the addition of ν_τ channel. The reconstruction of δ_{24} and δ_{34} gets refined particularly by the addition of ν_μ disappearance channel and the effect is prominent in the third panel. The reconstruction contour shrinks to give a bound to the parameter space. Next, we discuss the correlation of the phases and the active-sterile mixing angles and at what precision they can be measured in the present framework.

Figure 3.5 shows the efficacy of LBL experiments in the reconstruction of the active-sterile mixing angle in correlation to the CP phases at 1σ C.L. The phases and angles in question are shown along the rows and columns, respectively. The ranges of the mixing angles are chosen as per the discussion in section 3.2. Combining NOvA and T2K data to DUNE improves the precision of measurement in all the panels whereas, adding T2HK projected data gives a tighter bound to the parameter space. The *test* values of the angles are varied up to their upper limit at 99% C.L.: $\theta_{14} \lesssim 18.4°, \theta_{24} \lesssim 6.05°, \theta_{34} \lesssim 25.8°$, and the *true* values to be reconstructed were $\theta_{14} = 5.7°, \theta_{24} = 5°, \theta_{34} = 20°$

The span (horizontal and vertical) of the resulting contours gives an estimate of the uncertainties in measuring the mixing angles $(\theta_{14}, \theta_{24}, \theta_{34})$ and the CP phases $(\delta_{13}, \delta_{24}, \delta_{34})$, respectively. It should be noted that in the first row δ_{13} has less uncertainty as we have concluded from the previous results. In the third column, we note that as the value of θ_{34} increases the uncertainty also increases. This is an indication of the difficulty of measuring θ_{34} through experiments which in turn results in a poor reconstruction of the associated CP phase δ_{34}. To have a quantitative idea about the potential to reconstruct the true values of the active-sterile mixing angle θ_{i4} $(i = 1, 2, 3)$, we calculate how much the total horizontal span of each blue contour is. From this, we estimate the maximum range of uncertainty (to obtain a conservative range) in reconstructing θ_{i4} and tabulate these below in table 3.2.

Angle	Value to be reconstructed [Degree]	Reconstructed range [Degree]
θ_{14}	5.7	$3.3 \lesssim \theta_{14} \lesssim 9.1$
θ_{24}	5	$3.2 \lesssim \theta_{24} \lesssim 6$
θ_{34}	20	$9.0 \lesssim \theta_{34} \lesssim 25$

Table 3.2: The maximum reconstructed ranges for $\theta_{14}, \theta_{24}, \theta_{34}$ as estimated from figure 3.5 for DUNE + T2K + NOvA + HK.

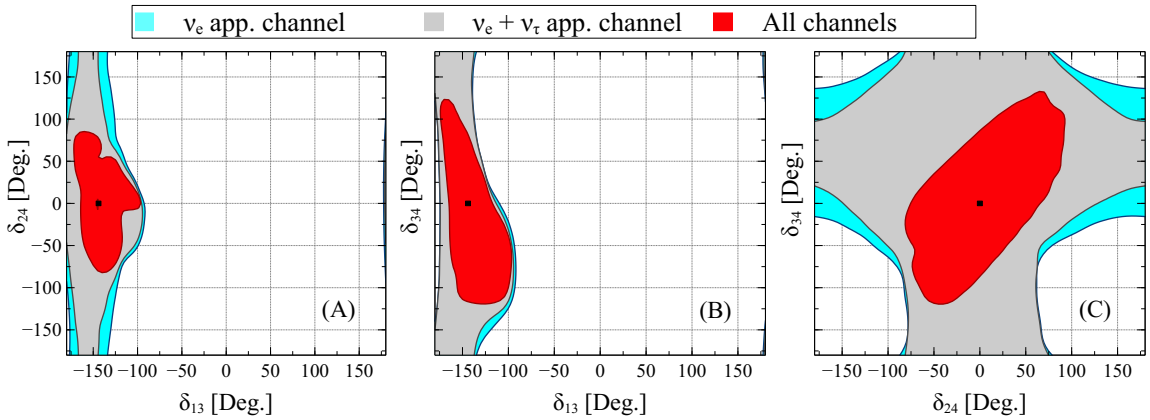

Figure 3.4: Reconstruction of the CP phases, taken pairwise at a time for three different channels at DUNE at a C.L. of 1σ (2 D.O.F.). for ν_e appearance channel (cyan), ν_e + ν_τ appearance channel (grey), and all channels (red). The three panels depict the test values of the three CP phases. The true values for the CP phases were assumed as $\delta_{13}, \delta_{24}, \delta_{34} = -0.8\pi, 0, 0$ and the true active-sterile mixing angles were chosen as $\theta_{14}, \theta_{24}, \theta_{34} = 5.7°, 5°, 20°$. The black dot indicates the true values assumed.

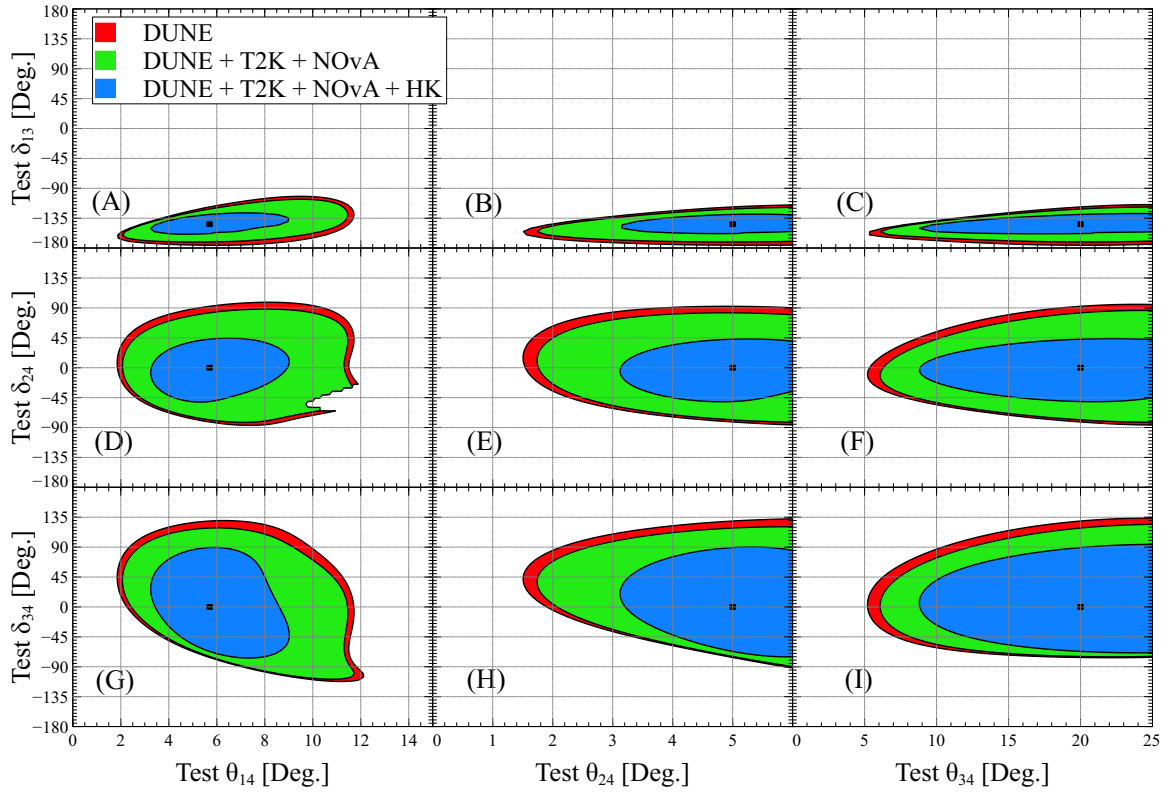

Figure 3.5: Reconstruction of the CP phases in correlation with the mixing angles $\theta_{14}, \theta_{24}, \theta_{34}$ at a C.L. of 1σ (2 D.O.F.) at DUNE (red), DUNE + T2K + NOvA (green), and DUNE + T2K + NOvA + T2HK (blue). The three columns and rows depict the test values of the three active-sterile mixing angles and the three CP phases, respectively. The true values for the CP phases were assumed as $\delta_{13}, \delta_{24}, \delta_{34} = -0.8\pi, 0, 0$ and the true active-sterile mixing angles were chosen as $\theta_{14}, \theta_{24}, \theta_{34} = 5.7°, 5°, 20°$. The black dot indicates the true values assumed.

3.5 Effect of the new phase on neutrinoless beta decay

Till now we have discussed the CP phases in the framework of oscillation experiments. In this section, we will examine their impact on another observable, *i.e.*, neutrino-less double beta decay(NDBD). The lepton number violating NDBD process will have a non-zero contribution in case the sterile neutrino is a Majorana particle. When θ_{14} is non-zero, the effective mass for NDBD process is [173]:

$$m_{\text{eff}} = |m_1|U_{e1}|^2 + m_2|U_{e2}|^2 e^{i\alpha_2} + m_3|U_{e3}|^2 e^{i\alpha_3} + m_4|U_{e4}|^2 e^{i\alpha_4}|, \tag{3.7}$$

where α_2, α_3, α_4 are the relevant CP phases. We have followed the parametrization given in equation 3.3. The relevant elements of the mixing matrix are as follows.

$$|U_{e1}| = c_{12}c_{13}c_{14}, |U_{e2}| = s_{12}c_{13}c_{14}, |U_{e3}| = s_{13}c_{14}, |U_{e4}| = \sin\theta_{14}. \tag{3.8}$$

The expression for the half-life of $0\nu\beta\beta$ transitions can be given as [174],

$$\frac{1}{T^{0\nu}_{1/2}} = G_{0\nu} \left| M_\nu \eta_\nu + M_N \eta_N \right|^2, \tag{3.9}$$

where,

$$\eta_\nu = \frac{U^2_{e\,i} m_i}{m_e}, \quad \eta_N = \frac{V^2_{e\,i} m_p}{M_i}. \tag{3.10}$$

In the above equation, m_i is the mass of active neutrino and U_{ei} is the PMNS mixing; whereas, θ_{ei} is the mixing among the active and sterile and M_i is the corresponding mass of heavy sterile. The reference masses m_e and m_p are chosen to be electron and proton masses, respectively. In the above, M_ν and M_N are the nuclear matrix elements (NME) for the exchange of light and heavy neutrinos, respectively.

The values of NME and phase space factor $G_{0\nu}$ can be found in Ref. [177]. The half-life of $0\nu2\beta$ is can generally be given as [178]

$$\frac{1}{T_{1/2}} = K_{0\nu} \left| \Theta^2_{ej} \frac{\mu_j}{\langle p^2 \rangle - \mu_j^2} \right|^2, \tag{3.11}$$

Here, $K_{0\nu} = G_{0\nu}(\mathcal{M}_N m_p)^2$ and $\langle p^2 \rangle \equiv -m_e m_p \frac{\mathcal{M}_N}{\mathcal{M}_\nu}$. j is the combined number of light and additional heavy neutrino states. μ_j and Θ_{ej} are the masses of neutrino states and the mixing with active neutrinos, respectively. Experiments have been performed for over a decade to tighten the lower bound for $T^{0\nu}_{1/2}$ for NDBD transformation. the most

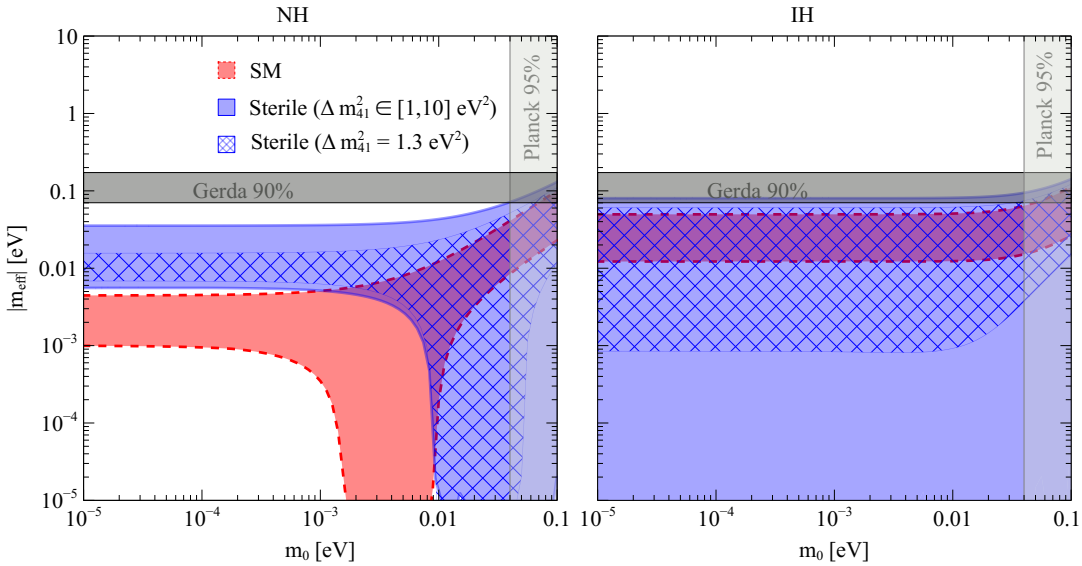

Figure 3.6: Effective mass of NDBD versus the smallest neutrino mass. The left and right panels show the case of NH and IH, respectively. The red (blue) region corresponds to 3+0 (3+1) scenario, labeled as SM (Sterile). The region hatched with blue *cross* lines represents $\Delta m^2_{41} = 1.3$ eV^2. The vertical light grey region is excluded by Planck data at 95% C.L. [175], while the horizontal dark region shows the 90% sensitivity from GERDA [176].

conservative values have been obtained from germanium-76, Xenon-136, and Tellurium-130 [179] isotopes. GERDA-II experiment has given a value of $T^{0\nu}_{1/2} > 8.0 \times 10^{25}$ year for $Ge^{(76)}$ [180] at 90% C.L., whereas, KamLAND-Zen experiment $Xe^{(136)}$ data has been able to put a bound at $T^{0\nu}_{1/2} > 1.07 \times 10^{26}$ year at 90% C.L. [181, 182].

In figure 3.6 we show how the effective mass for the standard $3+0$ scenario changes as we introduce the $3+1$ scenario. Here we have used equation 3.7 and varied the lightest mass. The two panels indicate the NH and IH, respectively. We consider a variation of Δm^2_{41} (for NH), and Δm^2_{43} (for IH) in between (1-10) eV^2. The CP phases α_2, α_3, and α_4 have been varied in between $-\pi$ to π. The other oscillation parameters follow the values tabulated in table 3.1 [115] as applicable for NH and IH. 10^7 iterations have been carried out for each value of the lightest mass. The red and blue regions show the variation of $|m_{eff}|$ in the case of $3+0$ and $3+1$ scenario, respectively. It is apparent from the figure that $|m_{eff}|$ can be significantly large when Δm^2_{41} is large and hence, constrained from the experimental constraints. To correlate the parameter space with our discussion in the previous sections about the oscillation phenomenon, we have marked the region corresponding to $\Delta m^2_{41} = 1.3eV^2$ with blue cross lines. Eventually, the blue regions can be seen to be shrinking and it gets down below the GERDA exclusion limit. For NH, there

is a complete cancellation of m_{eff} in the $3+0$ case when the lightest mass approximately lies in the range of $10^{-3} - 10^{-2}$ eV. On the contrary, for $3+1$ scenario there is no such complete cancellation in this region (due to the dominance of the m_4-term in equation 3.7 in this range) but it happens when the lightest mass is greater than $10^{-2}eV$. However, for IH, 3+0 case shows no total cancellation (dominant m_1-term in equation 3.7), while there is a total cancellation in the 3+1 case in the range mentioned. These results are compatible with [173].

3.6 Summary

In this chapter, we have discussed about the presence of an eV-scale sterile neutrino (in the oscillation framework) as a possible solution to SBL anomaly and have analyzed with what efficiency the present and future LBL experiments (DUNE, T2K, NOvA, T2HK) can probe the oscillation parameters. We have mainly focussed on the new CP phases ($\delta_{13}, \delta_{24}, \delta_{34}$). Initially, we have studied how the variation of these phases can impact the probability curve for different oscillation channels. We have followed the constraints on active-sterile mixing from global analyses in this work. While estimating the capability of the LBL data to probe the phases, we have concluded that $\nu_\mu \to \nu_e$ channel contributes the most in terms of constraining the parameter space, the contribution from $\nu_\mu \to \nu_\mu$ channel is also significant (because of the larger statistics), whereas, the contribution from $\nu_\mu \to \nu_\tau$ channel is lesser but it helps in exploring the $\delta_{24} - \delta_{34}$ parameter space in particular. We have done marginalization over all the poorly measured oscillation parameters in this entire work. During the reconstruction of the CP phases individually, we have found that δ_{24} and δ_{34} can't be reconstructed very efficiently with DUNE, T2K and NOvA data. But the inclusion of T2HK projected data attenuates the degeneracy significantly. We found that if the active-sterile mixing angles turn out to be lying close to their current upper limits, the enhanced sensitivities to the associated phases make the reconstructions of δ_{24} and δ_{34} much better. In comparison, we get tight bounds for the standard CP phase δ_{13} throughout the exercise. The precision of measuring δ_{13} remains unchanged in the case of addition of another sterile flavor and it has slight modification over the entire allowed range of active-sterile mixing. Further, we have studied the precision of probing the parameter space associated to one CP phase and one active-sterile mixing angle. We have drawn the conclusion that the parameter space associated with θ_{14} can be probed more precisely in comparison to the other mixing angles. Finally, a brief discussion has been done on the relevant parameter spaces in NDBD phenomenon and how they get

modified in presence of a sterile neutrino.

Chapter 4

Probing the Left-Right Symmetric Model in neutrino oscillation data

4.1 Introduction

Analyses of the neutrino experimental data accumulated in the domain of solar, reactor, and accelerator neutrinos have given us strong evidence of oscillation of massive neutrinos [32, 51]. Even though the neutrino mass is orders of magnitude smaller than the charged leptons, the search for mass generation is an important study. The oscillation experiments have been able to measure the mass-squared differences for the neutrinos which are Δm^2_{21} and $|\Delta m^2_{31}|$. It can be concluded that at least two of the three active neutrinos have non-zero masses. But the results from the oscillation data have not been able to determine the absolute magnitude of the neutrino masses. There are several mechanisms explored in the literature that account for neutrino mass generation. One of the salient mechanisms is the seesaw mechanism [39, 100]. It explains the generation of neutrino mass through the presence of a new right-handed (sterile) neutrino which introduces a mass scale higher than that of the electroweak scale.

The transformation of neutrinos is presented as (1, 2, -1) under the Gauge group $SU(3)_C \times SU(2)_L \times U(1)_Y$ in SM. A gauge singlet Majorana mass term can't be written in the case of neutrinos. Also, the absence of the RH neutrinos doesn't allow a Dirac mass term.

The initial solution to this problem can be the addition of a singlet right-handed neutrino ν_{iR} which transforms as (1, 1, 0) under the mentioned gauge group. Then one can write the neutrino mass term in terms of Yukawa couplings:

$$\mathcal{L}_{mass} = -\frac{1}{2} h_{ij} \bar{\psi_{iL}} \nu_{jR} \phi. \tag{4.1}$$

Thus when symmetry breaking occurs, ϕ acquires a vacuum expectation value (VEV) v and the neutrino gets a Dirac mass $m_{D_{ij}} = h_{ij}v$. But to be consistent with the smallness of the neutrino mass, one needs a very small Yukawa coupling, compared to that of charged leptons and quarks. There is no theoretical understanding of such a fine-tuned Yukawa coupling. Additionally, accidental $B - L$ symmetry in the SM prevents the neutrinos to have Majorana masses. To tackle this problem, there are models which attempt to explain the origin of neutrino mass by invoking dimension-5 operators of the form $\nu\nu\phi\phi/\Lambda$ (where Λ is a mass scale much higher than the electroweak scale) and applying the seesaw mechanism. In this mechanism, after electroweak symmetry breaking, neutrino obtains a mass of $\frac{v^2}{\Lambda}$, which explains the smallness of neutrino mass, because of the suppression by a high scale Λ.

4.2 Left-Right Symmetric model:

One of the most popular classes of neutrino mass models that naturally invokes the seesaw mechanism (so-called type-II seesaw) is the Left-Right Symmetric Model (LRSM) [39, 183–186]. One starts with the SM gauge symmetry $SU(3)_C \times SU(2)_L \times U(1)_Y$, which can explain the $V-A$ structure of the weak interaction and parity violation, which is reflected by the trivial transformation of all right-handed fields under $SU(2)_L$. However, the origin of parity violation is not explained within the SM, and the LRSM is motivated by a quest to seek an explanation for parity violation starting from a parity conserved theory at some higher energy scale. In LRSM, one extends the gauge group $SU(2)_L \times U(1)_Y$ to $SU(2)_L \times SU(2)_R \times U(1)_{B-L}$ where the fermions are represented by the following.

$$\begin{aligned} l_L = \begin{pmatrix} \nu_L \\ e_L \end{pmatrix} \sim (2,1,-1); \quad l_R = \begin{pmatrix} \nu_R \\ e_R \end{pmatrix} \sim (1,2,-1); \\ q_L = \begin{pmatrix} u_L \\ d_L \end{pmatrix} \sim (2,1,1/3); \quad q_R = \begin{pmatrix} u_R \\ d_R \end{pmatrix} \sim (1,2,1/3). \end{aligned} \tag{4.2}$$

LRSM is thus a simple extension of the Weinberg-Salam theory incorporating the right-handed neutrino. The foundation of the model is that Parity is an explicit symmetry until spontaneous symmetry breaking (SSB) occurs. The SSB occurs in the following two steps by the introduction of two Higgs scalars ξ and ϕ.

$$\begin{aligned} SU(2)_L \times SU(2)_R \times U(1)_{B-L} \to SU(2)_L \times U(1)_Y \text{ with } \langle \xi \rangle \neq 0, \\ SU(2)_L \times U(1)_Y \to U(1)_{em} \text{ with } \langle \phi \rangle \neq 0. \end{aligned} \tag{4.3}$$

ξ belongs to a triplet representation of $SU(2)_R$ with the representation $(1,3,2)$ and the Higgs doublet ϕ is taken as $(2,2,0)$. ξ can be represented in a 2×2 matrix form,

$$\xi = \frac{1}{\sqrt{2}}\sigma_i\xi_i, \tag{4.4}$$

such that ξ transforms under $SU(2)_R$ as $\xi \to u_R\xi u_R^\dagger$. To understand the $U(1)_Y$ charge content of ξ, we note that under a $U(1)_Y$ rotation,

$$\xi \to e^{-i\varepsilon}e^{-i\varepsilon\frac{\sigma_3}{2}}\xi e^{i\varepsilon\frac{\sigma_3}{2}} = \xi - i\varepsilon(\xi + [\frac{\sigma_3}{2},\xi]) + ... = \xi - i\frac{\varepsilon}{2}\begin{pmatrix}\xi_3/\sqrt{2} & 2(\xi_1+i\xi_2)/\sqrt{2}\\ 0 & -\xi_3/\sqrt{2}\end{pmatrix} + ... \tag{4.5}$$

Thus the $U(1)_Y$ charge content of ξ is,

$$\xi = \begin{pmatrix}\xi^+/\sqrt{2} & \xi^{++}\\ \xi^0 & -\xi^+/\sqrt{2}\end{pmatrix}. \tag{4.6}$$

The electromagnetic charge is given by,

$$Q_{em} = I_L^3 + Y = I_L^3 + I_R^3 + \frac{I}{2}. \tag{4.7}$$

When ξ^0 develops a VEV V,

$$\langle\xi\rangle = \begin{pmatrix}0 & 0\\ V & 0\end{pmatrix}, \tag{4.8}$$

then $SU(2)_L\times SU(2)_R\times U(1)_{B-L}$ breaks to $SU(2)_L\times U(1)_Y$ (see equation 4.3). The EM charge assignment of the Higgs doublet ϕ is,

$$\phi = \begin{pmatrix}\phi_1^0 & \phi_1^+\\ \phi_2^- & \phi_2^0\end{pmatrix}. \tag{4.9}$$

If ϕ develops a VEV,

$$\langle\phi\rangle = \begin{pmatrix}v_1 & 0\\ 0 & v_2\end{pmatrix}. \tag{4.10}$$

the second step of SSB (equation 4.3) occurs. Let us now look at the relevant Yukawa Lagrangian (we only discuss the part involving the interactions of the triplet ξ that are relevant for our subsequent neutrino oscillation phenomenology) [187].

$$\mathcal{L} \supset Y_{\alpha\beta}l_{\alpha L}^T Ci\sigma_2\xi l_{\beta L} + \lambda_\phi\phi^T i\sigma_2\xi^\dagger\phi + h.c., \tag{4.11}$$

where $Y_{\alpha\beta}$ $(\alpha, \beta = e, \mu, \tau)$ parameters denote the Yukawa couplings and C denotes the charge conjugation operator. Using the representation of ξ (equation 4.6), we can now write [188],

$$\mathcal{L} \supset Y_{\alpha\beta}\left[\xi^0 \bar{\nu}^C_{\alpha R}\nu_{\beta L} - \frac{1}{\sqrt{2}}\xi^+\left(\bar{l}^C_{\alpha R}\nu_{\beta L} + \bar{\nu}^C_{\alpha R} l_{\beta L}\right) - \xi^{++}\bar{l}^C_{\alpha R} l_{\beta L}\right] + h.c. \tag{4.12}$$

The range where the triplet scalar masses M_ξ which are assumed to be the same for all the members of the triplet are much higher than the EW scale. At this mass scale one can use the Effective Field Theory (EFT) approach to obtain an effective low-energy Lagrangian valid for the energy scale under consideration. The effective Lagrangian is obtained by integrating out the heavy triplet scalar fields and is defined as follows.

$$\exp\left[i\int d^4x \mathcal{L}_{eff}\right] = \exp\left[i\int d^4x \mathcal{L}_{SM}\right]\prod_{i=1}^{3}\mathcal{D}\xi_i\mathcal{D}\xi_i^\dagger \exp\left[i\int d^4x \mathcal{L}_\xi\right]. \tag{4.13}$$

The effective Lagrangian $\mathcal{L}_{eff}$ can be shown to have a power series expansion of the form,

$$\mathcal{L}_{eff} = \mathcal{L}_{SM} + \frac{1}{M_\xi}\mathcal{L}_{d=5} + \frac{1}{M_\xi^2}\mathcal{L}_{d=6} + ... = \mathcal{L}_{SM} + \delta\mathcal{L}_{d=5} + \delta\mathcal{L}_{d=6} + ... \tag{4.14}$$

The dimension-5 and dimension-6 terms of the effective lagrangian provide the neutrino mass term and the non-standard interaction (NSI) term of neutrinos, respectively [189–191]:

$$\begin{aligned}
\mathcal{L}^m_\nu &= \frac{Y_{\alpha\beta}\lambda_\phi v^2}{M_\xi^2}\left(\bar{\nu}^C_{\alpha R}\nu_{\beta L}\right) = -\frac{1}{2}\left(m_\nu\right)_{\alpha\beta}\left(\bar{\nu}^C_{\alpha R}\nu_{\beta L}\right), \\
\mathcal{L}^{NSI}_\nu &= \frac{Y_{\sigma\beta}Y^\dagger_{\alpha\rho}}{M_\xi^2}\left(\bar{\nu}_{\alpha L}\gamma_\mu\nu_{\beta L}\right)\left(\bar{l}_{\rho L}\gamma^\mu l_{\sigma L}\right),
\end{aligned} \tag{4.15}$$

where $v(\simeq 174$ GeV) denotes the VEV of the SM scalar Higgs field. m_ν is the neutrino mass matrix and will be explained shortly.

4.3 Non-Standard Interaction parameters and their correlation to LRSM parameters:

It is theoretically well-established that NSI which arises naturally in most of the neutrino mass models can be of charged-current (CC) or neutral-current (NC) in nature. Both of

them can be described with a dimension-six operator in the four-fermion effective Lagrangian [34, 192, 193],

$$\mathcal{L}_{\text{NC}-\text{NSI}} = -2\sqrt{2}G_F \sum_{\alpha,\beta,f,C} \varepsilon^{fC}_{\alpha\beta}(\bar{\nu}_\alpha \gamma^\mu P_L \nu_\beta)(\bar{f}\gamma_\mu P_C f), \tag{4.16}$$

$$\mathcal{L}_{\text{CC}-\text{NSI}} = -2\sqrt{2}G_F \sum_{\alpha,\beta,f',f,C} \varepsilon^{ff'C}_{\alpha\beta}(\bar{\nu}_\alpha \gamma^\mu P_L l_\beta)(\bar{f}'\gamma_\mu P_C f), \tag{4.17}$$

where, P_C denotes the chiral projection operators P_L or P_R. The dimensionless coefficients $\varepsilon^{fC}_{\alpha\beta}$ in equation 4.16 denote the strength of NSI between the leptons of flavors α and β ($\alpha, \beta = e, \mu, \tau$), and the first generation fermions $f \in \{e, u, d\}$.

In the present work, we are interested in NC-NSI which is relevant for neutrino propagating through the earth's matter. The NC-NSI couplings are parameterized by

$$\varepsilon^m_{\alpha\beta} \equiv \sum_{f=e,u,d} \varepsilon^f_{\alpha\beta}\frac{N_f}{N_e} \equiv \sum_{f=e,u,d} \left(\varepsilon^{fL}_{\alpha\beta} + \varepsilon^{fR}_{\alpha\beta}\right)\frac{N_f}{N_e}\,. \tag{4.18}$$

Here, N_f is the first generation (e, u, d) fermion number density in the ambient medium. The effective matter potential is then given by

$$V = A\begin{pmatrix} 1+\varepsilon^m_{ee} & \varepsilon^m_{e\mu} & \varepsilon^m_{e\tau} \\ \varepsilon^{m*}_{e\mu} & \varepsilon^m_{\mu\mu} & \varepsilon^m_{\mu\tau} \\ \varepsilon^{m*}_{e\tau} & \varepsilon^{m*}_{\mu\tau} & \varepsilon^m_{\tau\tau} \end{pmatrix}, \tag{4.19}$$

where $A = \sqrt{2}G_F N_e$ and N_e is the electron density along the neutrino propagation path. The relevant effective hamiltonian for neutrino propagation will then be given by,

$$H = \frac{1}{2E}\left[U\begin{pmatrix} 0 & 0 & 0 \\ 0 & \Delta m^2_{21} & 0 \\ 0 & 0 & \Delta m^2_{31} \end{pmatrix}U^\dagger + V\right], \tag{4.20}$$

where U is the 3×3 unitary PMNS mixing matrix. Equation 4.20 can be used to calculate the oscillation probability $P_{\nu_\alpha\to\nu_\beta} = |\langle\nu_\beta| e^{-iHL} |\nu_\alpha\rangle|^2$.

Now comparing equations 4.16 and 4.15, we can establish the following relation between the LRSM parameters (namely the triplet mass M_ξ and its coupling λ_ϕ with Higgs) and the NSI parameters $\varepsilon^m_{\alpha\beta}$ [187, 188].

$$\varepsilon^{\rho\sigma}_{\alpha\beta} = -\frac{M^2_\xi}{8\sqrt{2}G_F v^4 \lambda^2_\phi}(m_\nu)_{\sigma\beta}(m^\dagger_\nu)_{\alpha\rho}. \tag{4.21}$$

In the context of long-baseline experiments since neutrinos propagate through the earth's matter, mainly electron-type NSI will contribute to the matter potential and we can write $\varepsilon^m_{\alpha\beta} \simeq \varepsilon^{ee}_{\alpha\beta}$. The above equation 4.21 thus simplifies to,

$$\frac{M^2_\xi}{|\lambda^2_\phi|} = \frac{8\sqrt{2}G_F v^4 \varepsilon^m_{\alpha\beta}}{(m_\nu)_{e\beta}(m^\dagger_\nu)_{\alpha e}}. \tag{4.22}$$

The neutrino mass matrix that appears in the denominator is defined as,

$$(m_\nu)^2 = U \begin{pmatrix} m_1^2 & 0 & 0 \\ 0 & m_2^2 & 0 \\ 0 & 0 & m_3^2 \end{pmatrix} U^\dagger + A \begin{pmatrix} 1+\varepsilon^m_{ee}-\varepsilon^m_{\mu\mu} & \varepsilon^m_{e\mu} & \varepsilon^m_{e\tau} \\ \varepsilon^{m*}_{e\mu} & 0 & \varepsilon^m_{\mu\tau} \\ \varepsilon^{m*}_{e\tau} & \varepsilon^{m*}_{\mu\tau} & \varepsilon^m_{\tau\tau}-\varepsilon^m_{\mu\mu} \end{pmatrix}. \tag{4.23}$$

Note that in equation 4.23 we have subtracted a common diagonal term $\varepsilon^m_{\mu\mu}$ since it will have no physical effect on the final result. From equation 4.22, it is clear that the more constrained the couplings of $\varepsilon^m_{\alpha\beta}$, the tighter will be the upper limits on the LRSM parameter $\frac{M^2_\xi}{|\lambda^2_\phi|}$.

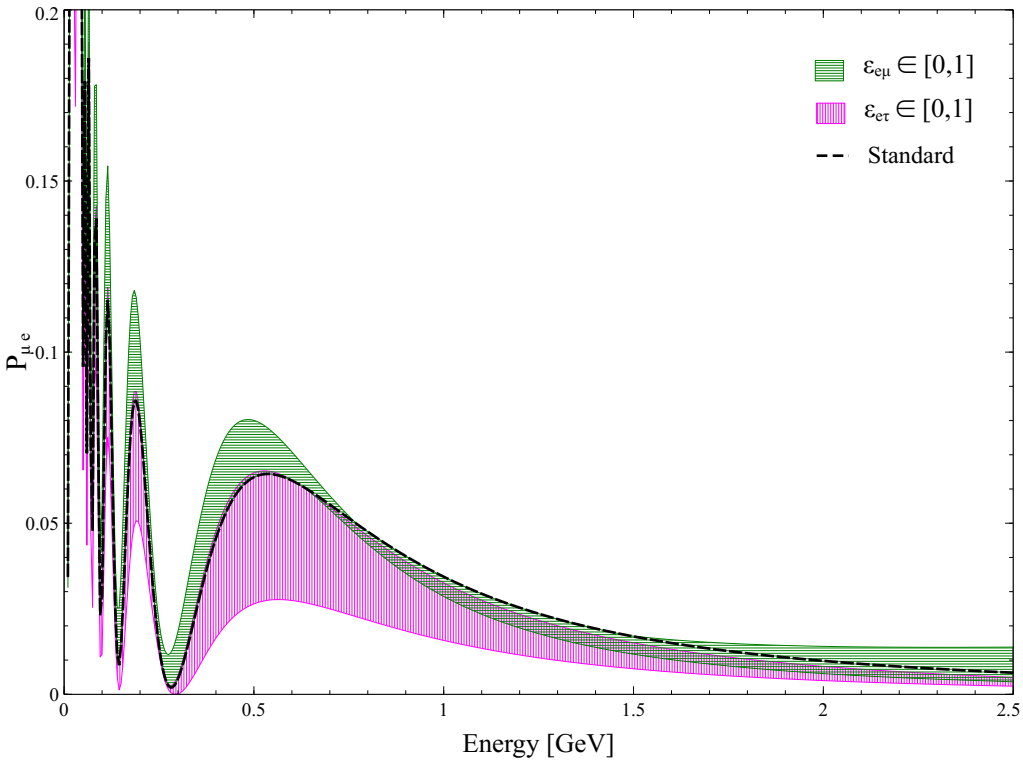

Figure 4.1: We show the probability band for the T2K experiment due to the variation of NSI parameters $\varepsilon_{e\mu}$ and $\varepsilon_{e\tau}$ through green and magenta shaded regions, respectively. We have varied both the NSI parameters within the range of $[0, 1]$ at a baseline of 295 km.

In figure 4.1, we have shown how the probability of the disappearance channel may change in presence of NSI in the long-baseline (295 km) experiment T2K. We have considered the $\nu_\mu \to \nu_e$ transition since it is one of the dominant channels in the signal. The black dashed curve gives the probability of $\nu_\mu \to \nu_e$ transition in a standard three-neutrino oscillation scenario. The NSI parameters $\varepsilon_{e\mu}$ and $\varepsilon_{e\tau}$ have been varied in the range $[0, 1]$, one at a time while all the other $\varepsilon_{\alpha\beta}$'s are taken to be zero. The corresponding phases are also taken to be zero. The green and magenta shaded regions give the variation in the probability curve as the NSI parameters $\varepsilon_{e\mu}$ and $\varepsilon_{e\tau}$ vary, respectively. At around $E = 0.55$ GeV, we can see a significant effect of the presence of NSI. The non-zero value of $\varepsilon_{e\mu}$ within the mentioned range can increase $P_{\mu e}$ by $\sim 33\%$, whereas, $\varepsilon_{e\tau}$ can decrease the same by $\sim 50\%$. The sensitivity of the long-baseline neutrino experiments to NSI couplings can indirectly probe the LRSM parameters as a function of the oscillation parameters using equation 4.22. We use the available data from the currently running LBL experiments NOvA and T2K for this analysis. In the next section, we sketch our simulation details and numerical procedure.

4.4 Simulation details:

In this study, we have used the results of the analyses of available data of the currently running LBL experiments T2K and NOvAas our inputs. T2K has a baseline of 295 km starting from J-PARC accelerator facility in Tokai to the far detector at Kamioka. The water Cherenkov far detector has a fiducial mass of 22.5 kt. The experiment uses a beam of 515 kW, delivering 1.97×10^{21} (1.63×10^{21}) Protons on target or POT in ν $(\bar{\nu})$ mode. T2K has a dataset of 318 (137) events in ν_μ $(\bar{\nu_\mu})$ channel and 94 (16) events in ν_e $(\bar{\nu_e})$ channel, also 14 events in ν_e channel from π decay [194]. Further details of experimental configurations and the analyses of data by the collaboration have already been discussed in literature [195, 196]. NOvA is another ongoing LBL experiment with a baseline of 800 km and employing a liquid scintillator far detector with a fiducial mass of 14 kt. NOvA uses a beam of 742 kW generating a POT of 8.85×10^{20} (12.33×10^{20}) in ν $(\bar{\nu})$ mode [197]. NOvA has a sample of 211 (105) events in ν_μ $(\bar{\nu_\mu})$ channel and 82 (33) events in ν_e $(\bar{\nu_e})$ channel [198]. In literature there exist several recent studies [199–201] that attempt to fit the available T2K and NOvAdata with vector NSI parameters. In the present study, we start from the following best-fit values for the NSI parameters from Tab. 2 of [201]. For the case of normal ordering (NO), the best-fit values are $|\varepsilon_{e\mu}| = 0.19, |\varepsilon_{e\tau}| = 0.28, |\varepsilon_{\mu\tau}| = 0.35, \phi_{e\mu} = -0.5\pi, \phi_{e\tau} = -0.4\pi, \phi_{\mu\tau} = 0.6\pi$. For inverted ordering (IO), the estimated best-

fit values are $|\varepsilon_{e\mu}| = 0.04, |\varepsilon_{e\tau}| = 0.15, |\varepsilon_{\mu\tau}| = 0.17, \phi_{e\mu} = -0.5\pi, \phi_{e\tau} = -0.54\pi, \phi_{\mu\tau} = 0.14\pi$. We then proceed with our analysis in two steps. At first, we use these values as the *true* values of the NSI parameters and estimate the capability to reconstruct these in the simulated data of future LBL experiments DUNE, T2HK, and T2HKK. In the next step, the limits on the NSI parameters obtained from the allowed region contours are then translated to the LRSM parameters (the procedure is explained in more detail in the next section) to estimate the capability of future LBL experiments to probe LRSM parameter space. Below we give brief descriptions of the three future LBL experiments that we simulate using GLoBES [164, 165] and its add-on *snu.c* (for implementing NSI physics).

DUNE is a 1300 km long baseline experiment from Fermilab to South Dakota with a liquid argon far detector (FD) of 40 kt fiducial mass. We prepare the GLoBES configuration files from the information in the Technical Design Report of DUNE [116, 202]. We use a 120 GeV proton beam of power 1.2 MW and of running 5 years each on ν and $\bar{\nu}$ mode (resulting in a total exposure of roughly 480 kt.MW.yr). The flux, cross-sections, migration matrices for energy reconstruction, efficiencies *etc.* were implemented according to the official configuration files [202] provided by the DUNE collaboration for its simulation.

T2HK is an *upgraded* version of T2K with a higher beam of 1.3 MW, offering a substantially higher exposure of 2.7×10^{22} POT per year. The two water Cerenkov Hyper-Kamiokande detectors are located at a baseline of 295 km, at an off-axis angle of 2.5° from the J-PARC neutrino beam in Japan. For the GLoBES simulation of T2HK, we consider a total fiducial mass of the far-detector as 374 kt (two detectors of 187 kt each) and a total runtime of 10 years (2.5 years in ν mode + 7.5 years in the $\bar{\nu}$ mode in order to have equal weightage from both polarities). The inputs (including the background/systematics/energy resolutions *etc.*) for preparing the GLoBES configuration files were taken from [114, 203].

T2HKK is another proposed setup for T2HK such that one detector (187 kt) is placed at a baseline of 295 km in Japan and the second detector (187 kt) is placed in Korea at a baseline of 1100 km, in order to probe the second oscillation maximum as well as to have access to more matter effects [204]. In our GLoBES simulation of T2HKK, we have taken the same configuration files as in T2HK with the detectors placed at two different baselines as stated above.

4.5 Results:

In figure 4.2, we illustrate the allowed regions at 68% and 90% confidence levels (C.L.) in the plane of LRSM parameter $(M_\xi/\lambda_\phi)^2$ and the atmospheric mixing angle θ_{23} when one off-diagonal NSI parameter is present at a time. The top (bottom) row shows the results with T2K (NOvA) available data. To fit the NSI parameter (thereby the LRSM parameter $(M_\xi/\lambda_\phi)^2$) and the standard parameter θ_{23}, we marginalized over $\theta_{12}, \theta_{13}, \delta_{\rm CP}, \Delta m^2_{21}, \Delta m^2_{31}$ (including both the hierarchies) and also over the corresponding NSI phase ($\phi_{e\mu}$ or $\phi_{e\tau}$, as the case may be). Note that, we have allowed the NSI parameters $\varepsilon_{e\mu}$ and $\varepsilon_{e\tau}$ to vary in the range $[0, 1]$, since a too large a value will defy the current constraints in the global analyses [205]. This has restricted our range of the LRSM parameter $(M_\xi/\lambda_\phi)^2$ up to roughly 12×10^{24}. Also, we have not discussed $\varepsilon_{\mu\tau}$ since there is already very tight constraint on it from Super-Kamiokande [206] as well as the global analyses [205].

For T2K, the presence of either NSI parameter $\varepsilon_{e\mu}$ or $\varepsilon_{e\tau}$ points to roughly similar values for $(M_\xi/\lambda_\phi)^2$ and θ_{23}. For θ_{23}, both the octants of θ_{23} are allowed by T2K data. Irrespective of the allowed octant of θ_{23}, T2K indicates a non-zero value of the LRSM parameter $(M_\xi/\lambda_\phi)^2$ at 68% C.L. In presence of $\varepsilon_{e\mu}$ ($\varepsilon_{e\tau}$), $(M_\xi/\lambda_\phi)^2 \gtrsim 4(5) \times 10^{24}$ at 68% C.L. for lower octant. For higher octant, while $\varepsilon_{e\mu}$ points to a bounded region: $0.5 \times 10^{24} \lesssim (M_\xi/\lambda_\phi)^2 \lesssim 11 \times 10^{24}$, $\varepsilon_{e\tau}$ only points to $(M_\xi/\lambda_\phi)^2 \gtrsim 1.5 \times 10^{24}$ in the range of parameters shown. Interestingly, the NOvA dataset is able to narrow down the allowed regions to a much-restricted set of values. Though NOvA is estimated to show degeneracies in θ_{23} octant at 90% for $\varepsilon_{e\mu}$, only a small higher octant solution survives at 68% C.L. The corresponding value of $(M_\xi/\lambda_\phi)^2$ is roughly less than 2.5×10^{24}. For $\varepsilon_{e\tau}$, NOvA data is able to exclude almost all the parameter space under consideration at greater than 90% C.L., except for only a very tiny region around $\theta_{23} \simeq 50.5^\circ$ and $(M_\xi/\lambda_\phi)^2 \lesssim 0.5 \times 10^{24}$. The difference in baseline length of T2K and NOvA (295 km vs 810 km) as well as higher peak energy of the neutrino flux (0.6 GeV vs 1.8 GeV) allows more matter effect in NOvA and thus constrains the NSI and LRSM parameter more stringently. We have checked that the range of values of $(M_\xi/\lambda_\phi)^2$ is approximately in the similar ballpark with [188], where the authors explore the dependence of the smallest neutrino mass on LRSM for the DUNE projected data.

In figure 4.3, we show similar allowed regions by considering the diagonal NSI parameters ε_{ee} and $\varepsilon_{\tau\tau}$, taken one at a time. For the diagonal NSI parameters, our analysis estimates a higher octant solution for both T2K and NOvA, again visibly more constraining in the latter case. We also note that the allowed regions are approximately independent of

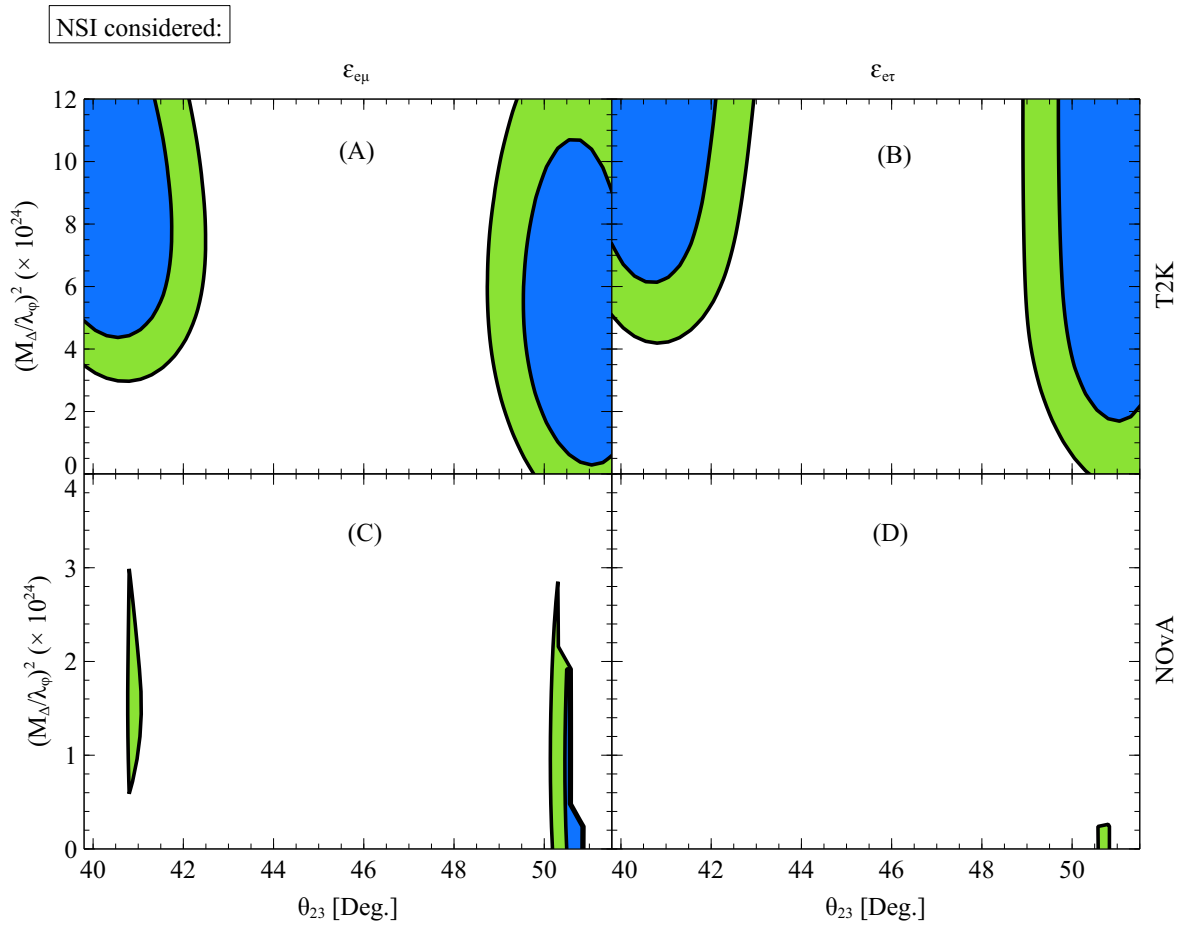

Figure 4.2: The allowed regions in the parameter space of $(M_\xi/\lambda_\phi)^2$ and θ_{23} are shown for the confidence levels of 68% (blue) and 90% (green). The top and bottom rows refer to the T2K and NOvA experiment, respectively, while the two columns indicate the presence of three single off-diagonal NSI parameters present at a time (indicated as labeled). The Normal hierarchy was assumed and the lightest neutrino mass is 0.1 eV.

the value of the LRSM parameter, thereby hinting at the worsening sensitivity to LRSM in presence of diagonal NSI. We have not shown $\varepsilon_{\mu\mu}$ since it can be safely subtracted from ε_{ee} and $\varepsilon_{\tau\tau}$ without any physical impact on the analysis (see equation 4.23).

In figure 4.4, we illustrate the allowed regions in the parameter space of the LRSM parameter and the standard Dirac CP phase $\delta_{\rm CP}$. Here we have marginalized over $\theta_{12}, \theta_{13}, \theta_{23}, \Delta m^2_{21}$, Δm^2_{31} (including both the hierarchies) and also over the corresponding NSI phase $\phi_{e\mu}$ or $\phi_{e\tau}$. At 68% C.L., in presence of $\varepsilon_{e\mu}$, T2K restricts allowed values of $\delta_{\rm CP}$ to the lower-half plane ($\in [-\pi, 0]$ approximately). At 90% C.L., the allowed values of $\delta_{\rm CP}$ also extend to the upper-half plane for $(M_\xi/\lambda_\phi)^2 \simeq (6-9) \times 10^{24}$. NOvA, on the other hand, allows all $\delta_{\rm CP}$ values for small LRSM triplet Higgs mass to coupling

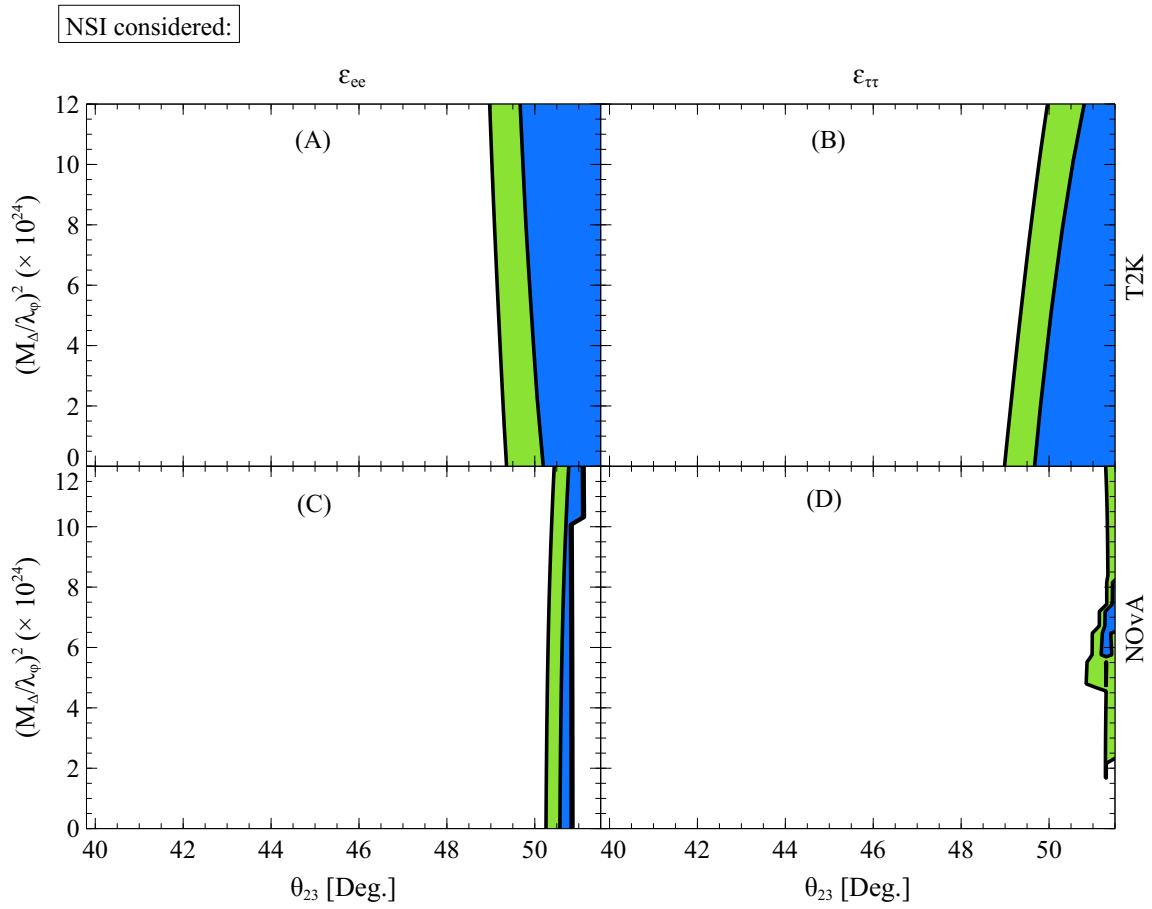

Figure 4.3: Similar to figure 4.2 but shown for the diagonal NSI parameters.

ratio($(M_\xi/\lambda_\phi)^2 \simeq (1-3)\times 10^{24}$), but prefers the CP phase to lie largely in the range -45° to 135° for larger LRSM parameter. This implies a somewhat complementary nature of T2K and NOvA while probing the CP phase, and this is consistent with the analyses by the collaboration while fitting the CP phase in the standard scenario [198, 207]. In presence of $\varepsilon_{\mu\tau}$, T2K again rules out a large part of positive values of $\delta_{\rm CP}$ at 68% C.L. (less so at 90% C.L., but the pattern of the allowed regions remains qualitatively similar). For $\varepsilon_{e\tau}$, NOvA is more restrictive compared to $\varepsilon_{e\mu}$ (as also observed for figures 4.2 and 4.3), and the allowed value of the LRSM parameter is estimated to be lying at less than 6×10^{24} at 68% C.L. (around $\delta_{\rm CP} \simeq -\pi/2$). We note that the shapes of the allowed contours in figure 4.4 are roughly in agreement with the previous analyses where T2K and NOvA data (available at that time) were fit with NSI [199, 200]. Overall it is clear that when the CP phase $\delta_{\rm CP}$ is kept free, the contours become less constraining, as compared to the case when the mixing angle θ_{23} is allowed to vary.

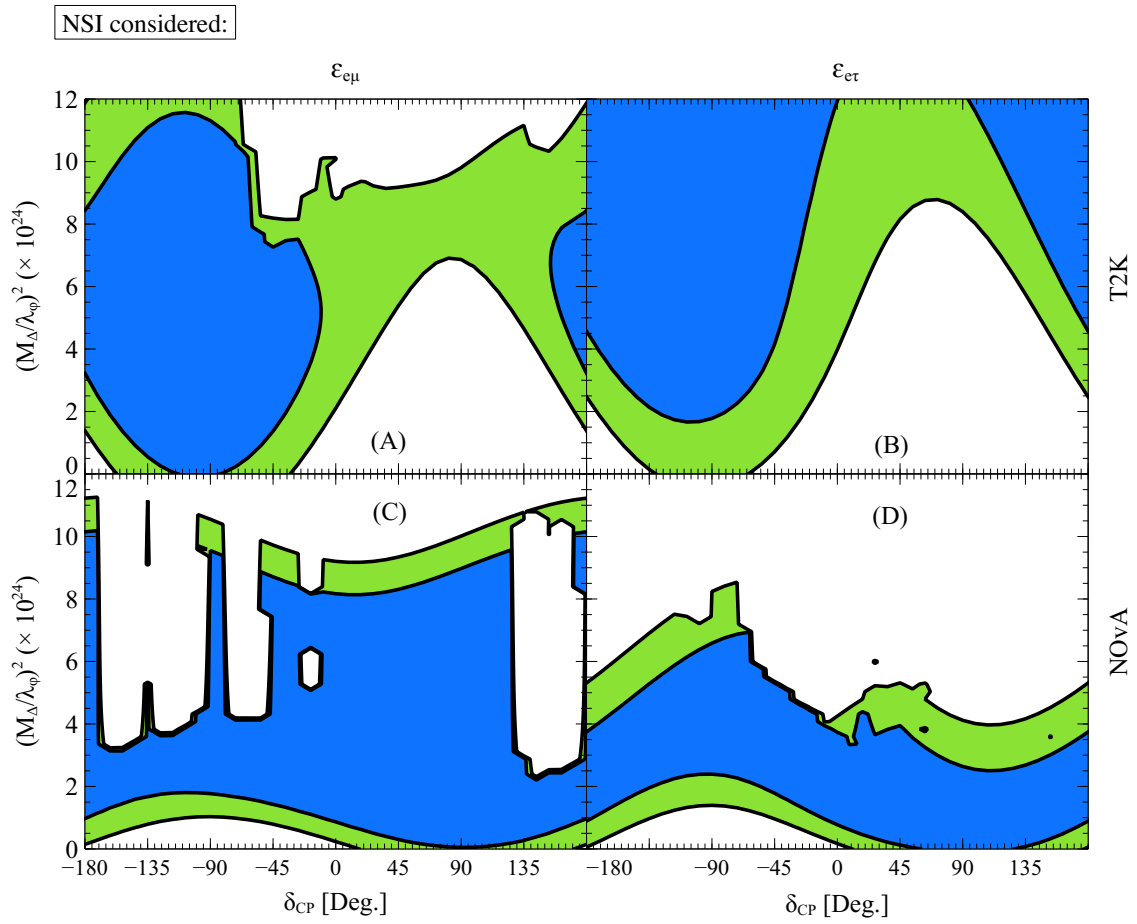

Figure 4.4: Similar to figure 4.2 but shown as a function of the Dirac CP phase $\delta_{\rm CP}$. Blue (green) contour indicates 68% (90%) C.L.

While probing the LRSM parameter with the diagonal NSI, the complementary nature of T2K and NOvA (in ruling out the CP phase values at a given C.L.) becomes more apparent. While T2K shows only slight dependence on $(M_\xi/\lambda_\phi)^2$ without an upper limit in the range discussed, NOvA actually restricts its upper limit to around $(7-8)\times 10^{24}$.

Figure 4.6 illustrates the upper limit on $M_\xi/|\lambda_\phi|$ as a function of the lightest neutrino mass m_1. The lowest or the most conservative estimate for the upper limit from all the NSI parameter is reported here for a given value of m_1. This is a similar strategy followed in [188]. It shows that the upper limit on $M_\xi/|\lambda_\phi|$ gets constrained rather steeply for $m_1 \lesssim 50$ meV, and then slightly slows down to become roughly 3.5×10^{12} when $m_1 \gtrsim 50$ meV. Figure 4.7 shows that for an estimated constraint on $M_\xi/|\lambda_\phi|$ (for a fixed $m_1 = 0.1$ eV), how the individual triplet scalar mass M_ξ and the coupling λ_ϕ are allowed to vary.

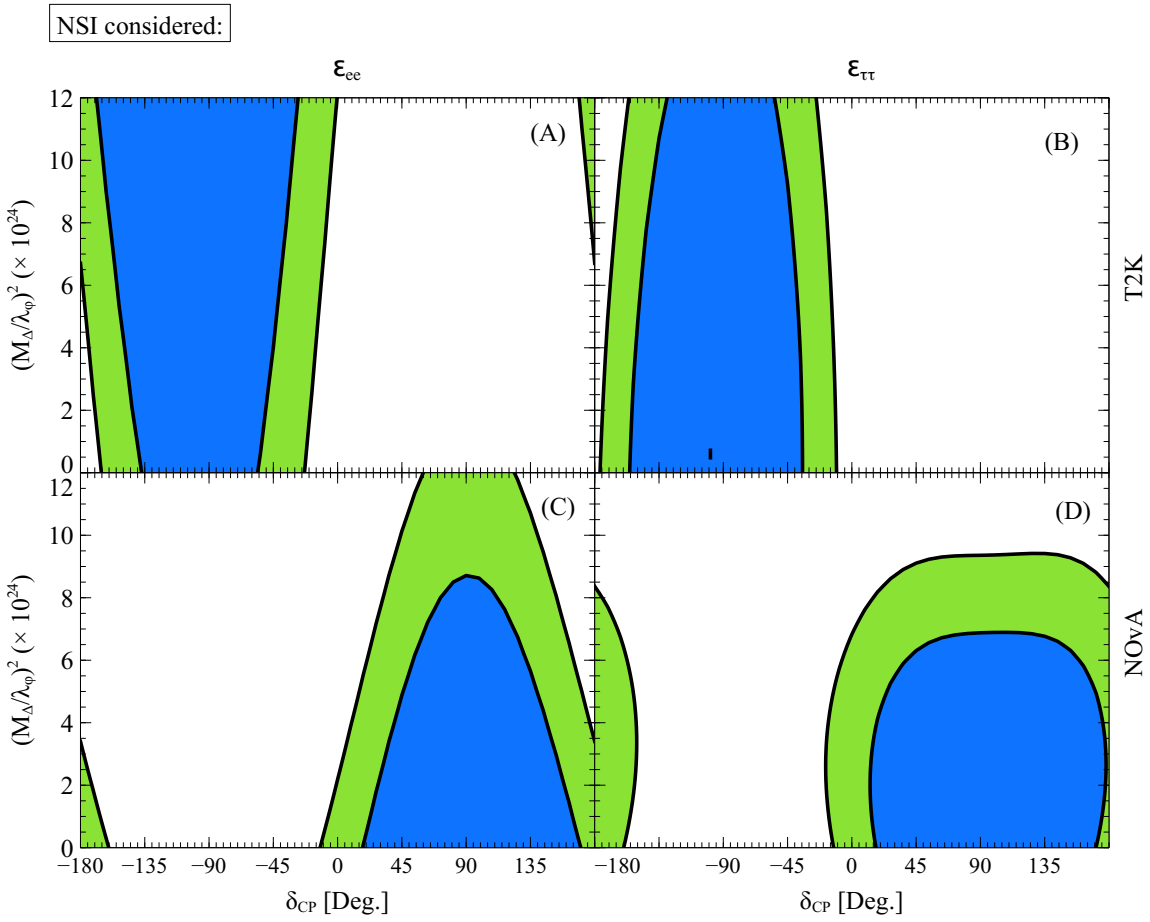

Figure 4.5: Similar to figure 4.4 but shown for the diagonal NSI parameters.

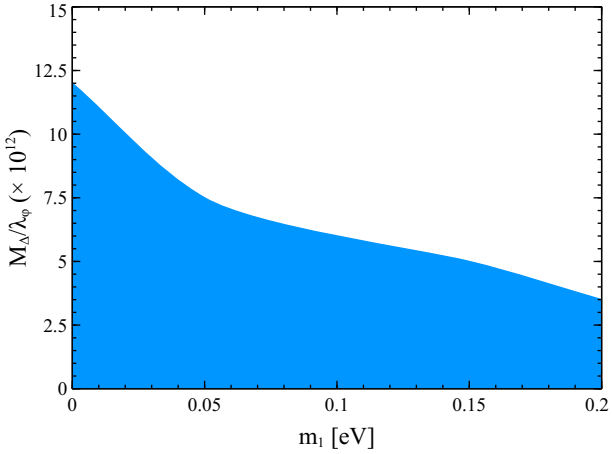

Figure 4.6: Shows how $M_\xi/|\lambda_\phi|$ is constrained as a function of the lightest neutrino mass $m1$. NOvA data was used for this figure.

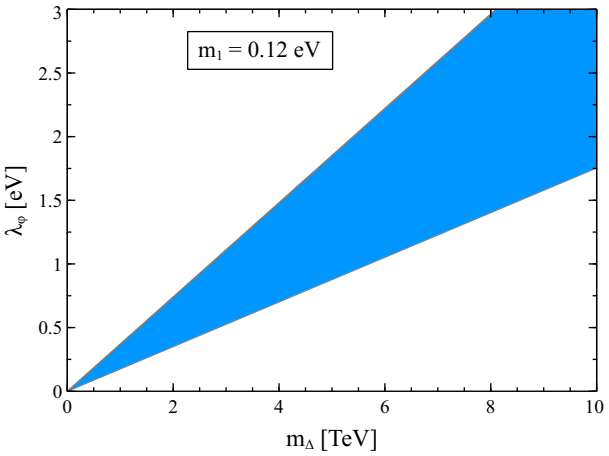

Figure 4.7: For a given constraint on $M_\xi/|\lambda_\phi|$, this figure illustrates how much each quantity can vary.

4.6 Summary:

In this chapter, we have done a brief discussion on the Left-Right Symmetric Model that spontaneously incorporates the popular seesaw mechanism for neutrino mass generation. We have identified the relevant LRSM parameters M_ξ (mass of the triplet scalar) and the Higgs-triplet coupling λ_ϕ in our study. We have implemented the low-energy effective field theory approach and explained how the LRSM parameters are related to the NC NSI interactions. We have shown how the effect of the NSI parameters can be probed through long-baseline neutrino oscillation experiments. Here, we have extracted available data from two ongoing experiments: NOvA and T2K. We have used the GLoBES framework to estimate the LRSM parameters by probing the NSI couplings. The variation in the ratio of the LRSM parameters $(M_\xi/\lambda_\phi)^2$ has been shown in correlation to the poorly measured standard oscillation parameters θ_{23} and the Dirac CP phase $\delta_{\rm CP}$. Even though the LRSM parameters could not be constrained tightly, θ_{23} has indicated higher octant solutions for both T2K and NOvA experiments. NOvA data have shown tighter constraints for θ_{23}. Whereas, in the case of $\delta_{\rm CP}$ the two experimental data have implied complementary results. Depending on the physics capabilities of the two experiments, we are able to estimate restrictive upper limits on the LRSM parameters. We have demonstrated the mentioned constraints in terms of the lightest neutrino mass as well.

Chapter 5

Investigating the new physics scenario in the P2O experiment

5.1 Introduction

Lorentz invariance comes as a natural consequence of *local* relativistic quantum field theory. The violation of Lorentz invariance may occur if the locality of the theory is given up and is expected to be suppressed by Planck mass ($M_P \sim 10^{19}$ GeV). Lorentz invariance violation (LIV) can be probed at a low energy scale through coherence, interference, and extreme effects. One example of interference is neutrino oscillation in long-baseline (LBL) experiments [208–211]. Now, for these experiments, the neutrino beam passes through the earth's crust and the matter effect can give a CPT violation-like signal. The effects of CP and T violation have been studied for appearance and disappearance channels by varying both the baseline and energy for neutrino oscillation experiments [142]. This study has helped to disentangle the matter effect and the effect due to CPT violation and matter effect in the standard oscillation scenario.

The effective Hamiltonian in the case of ultra-relativistic left-handed neutrinos is given by [212]:

$$(\mathcal{H}_{eff})_{\alpha\beta} = E\delta_{\alpha\beta} + \frac{m^2_{\alpha\beta}}{2E} + V_{\alpha\beta} + \frac{1}{E}(a^{\mu}_{L}\, p_{\mu} - c^{\mu\nu}_{L}\, p_{\mu}p_{\nu})_{\alpha\beta} \tag{5.1}$$

The indices α and β indicate the neutrino flavors. p_μ and E are the four-momenta and energy of the neutrinos. The first two terms in the equation are the standard kinematic terms; the term $V_{\alpha\beta}$ arises due to matter-induced potential, and the last term in the parentheses denotes the LIV terms, respectively. The terms a_L and c_L are the CPT violating and CPT conserving terms, respectively [213]. The current work deals with the isotropic components of the LIV parameters. For the matter effects, since, it's the earth's crust, we only

consider the potential that arises due to the CC events with the electrons and neglects the effects due to other interactions. Introducing the ultra-relativistic limit (equation 2.20), we get the following form of the Hamiltonian [214]:

$$\begin{aligned}\mathcal{H}_{eff} &= \frac{1}{2E}U\begin{pmatrix}0 & 0 & 0\\ 0 & \Delta m^2_{21} & 0\\ 0 & 0 & \Delta m^2_{31}\end{pmatrix}U^\dagger + \sqrt{2}G_F N_e\begin{pmatrix}1 & 0 & 0\\ 0 & 0 & 0\\ 0 & 0 & 0\end{pmatrix}\\ &+ \begin{pmatrix}a_{ee} & a_{e\mu} & a_{e\tau}\\ a^*_{e\mu} & a_{\mu\mu} & a_{\mu\tau}\\ a^*_{e\tau} & a^*_{\mu\tau} & a_{\tau\tau}\end{pmatrix} - \frac{4}{3}E\begin{pmatrix}c_{ee} & c_{e\mu} & c_{e\tau}\\ c^*_{e\mu} & c_{\mu\mu} & c_{\mu\tau}\\ c^*_{e\tau} & c^*_{\mu\tau} & c_{\tau\tau}\end{pmatrix}\end{aligned} \tag{5.2}$$

In equation 5.2 the first term signifies the H_{vacuum} part of the Hamiltonian for left-handed neutrinos. Whereas, the second term is H_{matter} which consists of the induced potential. G_F is the Fermi coupling constant and N_e is the number density of electrons in the medium. The $-4/3$ factor corresponding to the last term arises due to the non-observability of the Minkowski trace of c_L. It should be noted that the contribution of LIV in oscillation through $a_{\alpha\beta}$ ($\alpha, \beta = e, \mu, \tau$) is proportional to the neutrino baseline L and the contribution through $c_{\alpha\beta}$ is proportional to L/E. Constraints on $c_{\alpha\beta}$ have been studied extensively in the context of atmospheric neutrinos by the Super-Kamiokande collaboration. They have studied the effect of LIV for path lengths varying from 15 to 12,800 km and energies ranging from 100 MeV to 100 TeV [208, 215].

The proposed P2O experiment [88, 216–218] will have a baseline extending approximately 2595 km from the Protvino accelerator complex to the ORCA/KM3NET detector at the Mediterranean, - both of which are already existing. P2O baseline is most sensitive to the first $\nu_\mu \to \nu_e$ oscillation maxima around 4-5 GeV. Neutrino interaction around this energy is dominated by Deep Inelastic Scattering which is relatively well described theoretically, compared to, for *e.g.*, 2-2.5 GeV (for DUNE) where resonant interactions and nuclear effects can potentially impact the measurements more significantly [219–224]. Such a very long baseline and relatively higher energy of the oscillation maxima give P2O an excellent level of sensitivity, especially towards neutrino mass ordering. As has been illustrated in reference [225], the P2O baseline is favorable to determine mass hierarchy also due to the much less interference by the hierarchy-CP phase degeneracy. The very large detector volume of 6 Mt at ORCA will allow the detection of thousands of neutrino events per year even with a very large baseline and a moderate beam power, - subsequently offering sensitivities to neutrino mass ordering, CP violation, and θ_{23}-octant that are com-

petitive with the current and upcoming long-baseline neutrino experiments[1] [218, 226]. Recently it has been proposed that it is also possible to reach unprecedented sensitivity to leptonic CP violation at P2O using tagged neutrino beams by utilizing the kinematics of neutrino production in accelerators and recent advances in silicon particle detector technology [227]. In recent years, there has been some interest in estimating the new physics capabilities of P2O. Reference [228] discussed the sensitivity reach of P2O to Non-unitarity of the leptonic mixing matrix and also estimated how it will affect the standard physics searches. The authors of [225] discussed the possible optimization of P2O in order to explore non-standard neutrino interactions.

In this chapter, we analyze the capabilities of P2O to probe violations of Lorentz invariance and CPT symmetry to estimate the constraints that can be put on these new physics parameters. We have considered the upcoming experiments P2O and DUNE with baselines of 2600 km and 1300 km, respectively. Our motivation is to investigate if better constraints can be put on the parameters with a longer baseline.

5.2 Simulation details:

Due to the large fiducial mass of the water Cherenkov detector at ORCA, P2O is expected to provide good statistics, even with moderate beam power and runtime. In the current manuscript, we aim to probe the sensitivity of the P2O experiment (in addition to the DUNE experiment) to put a bound on LIV parameters.

In this work, we simulate the LBL neutrino experiments DUNE and P2O using GLoBES [164, 165]. DUNE is a 1300 km long-baseline experiment employing a liquid argon far detector (FD) of 40 kt fiducial mass with a beam of power 1.07 MW and running 3.5 years each on ν and $\bar{\nu}$ mode (resulting in a total exposure of roughly 300 kt.MW.yr corresponding to 1.47×10^{21} protons on target or POT). We have used the official configuration files [166] provided by the DUNE collaboration for its simulation. Charged current (CC) electron neutrino appearance signals, muon neutrino disappearance signals (CC), as well as neutral current (NC) backgrounds, and tau neutrino appearance backgrounds (along with the corresponding systematics/efficiencies *etc.*), are already included in the configuration files.

P2O (Protvino to ORCA) is a proposed long baseline neutrino experiment with a base-

[1] P2O in its nominal configuration with a 90 kW beam, can resolve mass ordering with $\gtrsim 6\sigma$ sensitivity in 5 years of running, and also has a projected sensitivity of more than 3σ to θ_{23}-octant with 3 years of running. With a 450 kW beam, it can offer 2σ sensitivity to $\delta_{\rm CP}$ after 3 years of operation.

line of nearly 2595 km from the Protvino accelerator complex, situated at 100 km south of Moscow to the site of ORCA (Oscillation Research with Cosmics in the Abyss), hosting 6 MT a Cherenkov detector located 40 km off the coast in South France, at a mooring depth of 2450 m in the Mediterranean sea. ORCA is the low energy component of the KM3NeT Consortium [229], with a primary goal of studying atmospheric neutrino oscillations in the energy range of 3 to 100 GeV in order to determine the neutrino mass ordering. Currently, 10 lines (*i.e.*, detection units) of the ORCA detector are live and taking data. A full ORCA detector is expected to have 115 lines and foresees completion in subsequent phases around 2025 [230]. Construction of the neutrino beamline and relevant upgradation of the accelerator for the P2O experiment is expected to be completed in a few years. Assuming a favorable geopolitical situation and available funding, the P2O project in its nominal configuration might be realised during the next decade [231]. We simulate the nominal configuration[2] of P2O experiment using a 90 kW proton beam with a runtime of 3 yrs. in ν and 3 yrs. in $\bar{\nu}$ mode, - corresponding to a total POT of 4.8×10^{20}. The baseline mostly passes through the earth's upper mantle with an average density of 3.4 g/cc and the deepest point along the beam being 134 km [232]. The fluxes, detector response parameters, detection efficiencies, signal and background systematics *etc.*, corresponding to our nominal P2O configuration were taken from [218, 229].

We have attempted to see how the LIV parameters can be reconstructed considering their $\Delta\chi^2$ correlation with each other and also with the oscillation parameters. Here we follow the method of $\Delta\chi^2$ calculation from section 3.1.1. The Hamiltonian in equation 5.2 has been incorporated in GLoBES using the plugin *snu.c* [162, 163] which handles the sterile and non-standard interaction parameters in neutrino oscillation. But in this case, we have modified the probability function in *snu.c* to study the LIV parameters accordingly.

5.3 Effects of the LIV parameters on the oscillation probabilities:

To find the impact of the LIV parameters in long-baseline (LBL) experiments, we first have a look at the probability distribution. We have taken the non-zero value of one $a_{\alpha\beta}$ at a time to assess the role of individual LIV parameters.

In figure 5.1 the probability distribution is given as a function of the energy P2O ex-

[2]There are proposals for using an upgraded proton beam with 450 kW power and also to use the Super-ORCA detector with denser geometry, lower energy thresholds and better flavour identification capabilities [218].

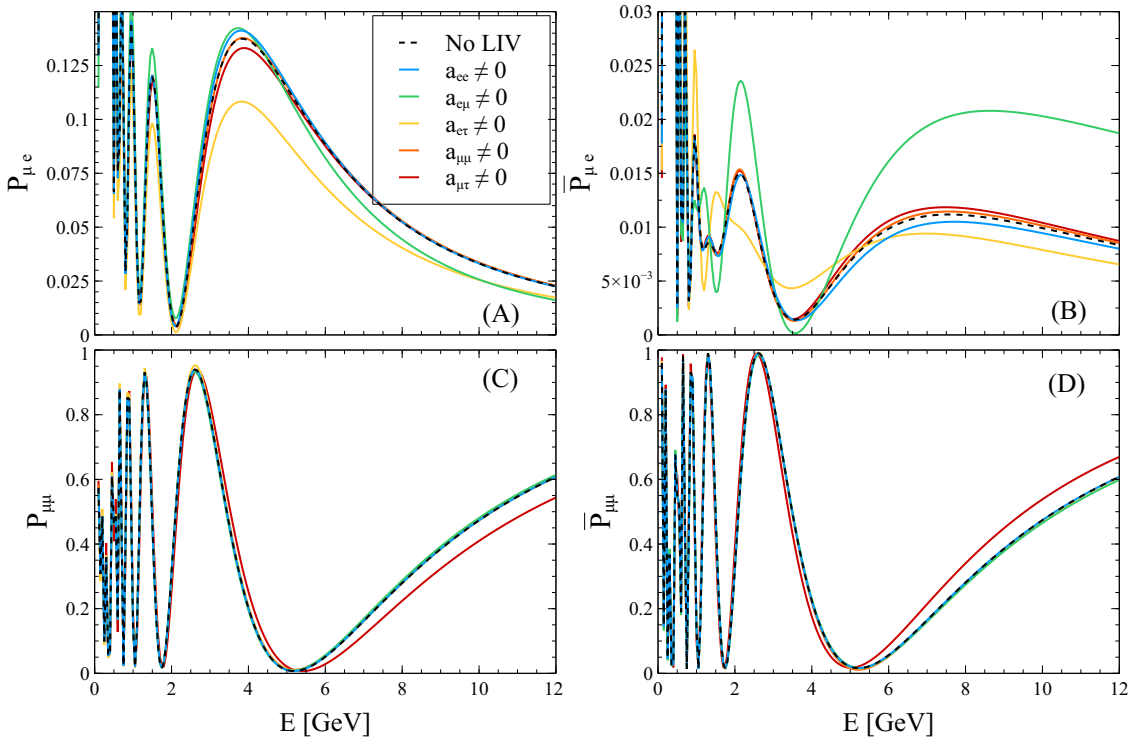

Figure 5.1: The probability curve for P2O experiment in presence of non-zero LIV parameters ($a_{ee} = a_{e\mu} = a_{e\tau} = a_{\mu\mu} = a_{\mu\tau} = 5 \times 10^{23}$ GeV). The top and bottom rows give the probability distribution for appearance and disappearance channels, respectively. The left and right columns give the probability distribution for neutrino and anti-neutrino modes, respectively.

periment can probe, i.e., up to 12 GeV. The black dotted curve gives us the distribution in absence of LIV while the colored curves demonstrate the effect of LIV on probability. We have taken the same numerical values of different LIV parameters to display their effects uniformly. We have taken the phase values $\phi_{\alpha\beta}$ corresponding to the off-diagonal elements ($a_{\alpha\beta}, \alpha \neq \beta$) to be zero as well. Here we can see that fluctuation in the probabilities due to non-zero values of the LIV parameters are manifested more in the case of $P_{\mu\mu}$ and $\overline{P}_{\mu\mu}$ in comparison to $P_{\mu e}$ and $\overline{P}_{\mu e}$ (please note, the scales for these two channels are different). In the disappearance channel, the effect of the non-zero value of the LIV parameter $a_{\mu\tau}$ is more distinct. It reduces the probability in the neutrino mode and increases the probability in the anti-neutrino mode by $\sim 5\%$ at $E = 12$ GeV. Whereas, for the appearance channel $P_{\mu e}$, the non-zero value of $a_{e\tau}$ reduces the probability by $\sim 2.5\%$ around the second oscillation maxima.

5.4 Results:

In this section, we will discuss the results obtained in the analysis. While doing the $\Delta\chi^2$ calculations we have taken the *true* values of the oscillation parameters as mentioned in table 2.1. We have done marginalization over the poorly measured oscillation parameters ($\theta_{13}, \theta_{23}, \delta_{CP}, \Delta m^2_{31}$ (for both mass hierarchies)) with the mentioned prior and uncertainties shown in table 2.1. The *glbChiNP* function in GLoBES has given us a scope to implement the marginalization during the $\Delta\chi^2$ calculation more efficiently without increasing the computation time. We have taken the true values of the LIV parameters, including the relevant phases, to be zero.

5.4.1 Correlation among the LIV parameters

Next, we have demonstrated how the experiments can reconstruct the LIV parameters in correlation to each other. In figure 5.2 and figure 5.3 the χ^2 distribution of the test parameters in correlation are shown as realized by P2O projected data. The solid and dotted lines give the 3σ and 2σ contours, respectively. While doing these statistical calculations we have marginalized over the test values of θ_{23}, δ_{13}, Δm^2_{31} (normal or inverted mass hierarchy) and also the relevant phases of the non-diagonal LIV parameters (varying over the entire parameter space $[0,\ \pi]$). It can be observed that test $a_{e\beta}$ ($\beta = e,\ \mu,\ \tau$) has tighter bounds in comparison to other LIV parameters. But from the bottom panel of figure 5.4, we can see that adding DUNE simulated data improves the efficiency of measurement of $a_{\mu\tau}$ parameter almost by one order. Fig. 5.5 shows the χ^2 correlation among the off-diagonal LIV parameters themselves ($|a_{e\mu}|, |a_{e\tau}|, |a_{\mu\tau}|$) and also between the two diagonal parameters a_{ee} and $a_{\mu\mu}$, for P2O and (P2O+DUNE). The improvement by the combined analysis is especially prominent for the most impactful parameter space $a_{e\mu} - a_{e\tau}$ (top left panel of Fig. 5.5).

5.4.2 Correlation of the LIV parameters with the oscillation parameters

In figure 5.6 we demonstrate how efficiently LBL data can reconstruct the LIV parameters in correlation to the CP phase δ_{CP}. The LIV parameters are varied along the x-axis and the CP phase is varied along the y-axis encompassing the entire range $[-\pi, \pi]$. At 3σ C.L., P2O simulated data fails to give any bound on the values of the CP phase but has tighter bounds in the case of a_{ee} and $a_{e\mu}$. The 2σ contour for P2O simulated data tightens the bounds for the LIV parameters, and marginalizing also shows some exclusion regions

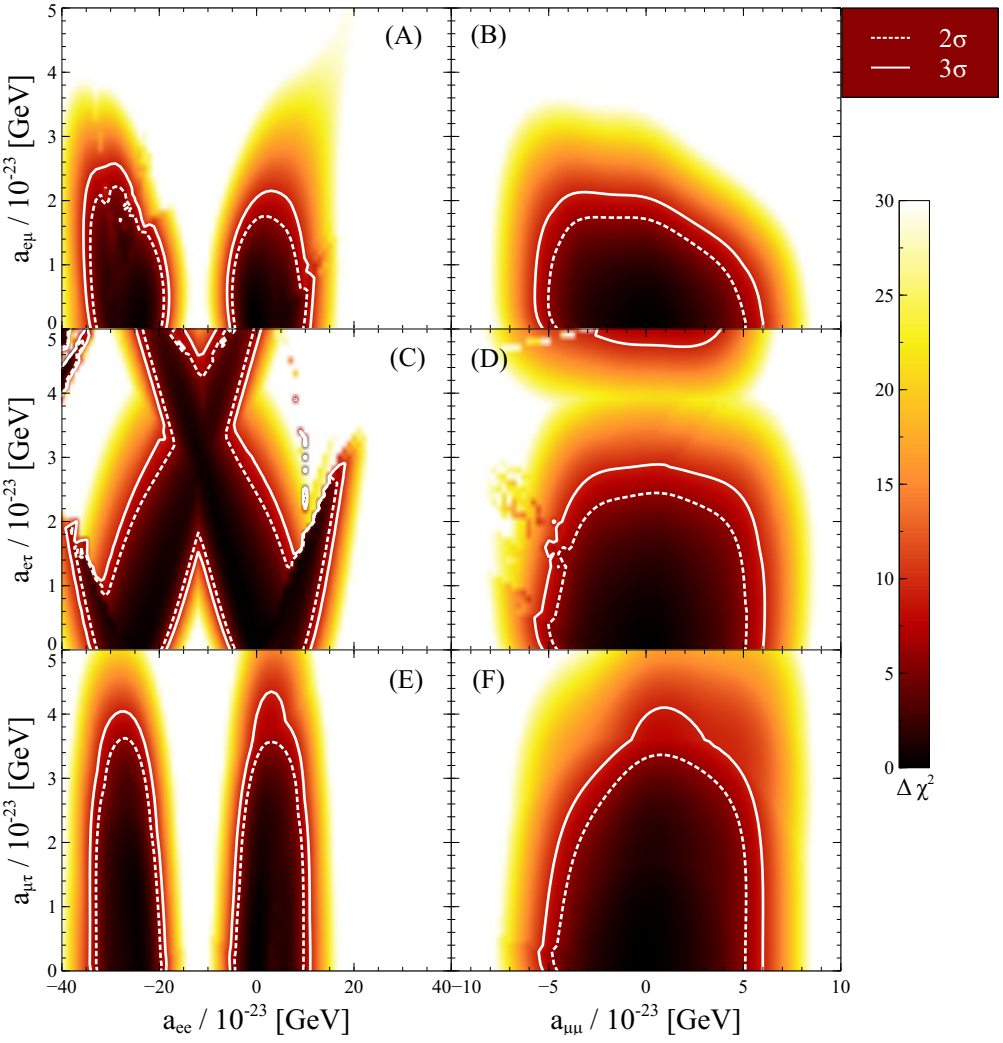

Figure 5.2: Sensitivity of simulated P2O experiment to the LIV parameters pairwise. The solid and dotted lines mark the 3σ and 2σ confidence level (C.L.), respectively.

for δ_{CP} in correlation with $a_{\mu\beta}(\beta = e, \mu, \tau)$. Adding DUNE simulated data changes the scenario drastically. The allowed regions shrink considerably around the true values in the parameter space. We still have the degeneracy along a_{ee}. The contours in the bottom panel (with the off-diagonal terms of the LIV parameters) are not closed because we have taken the modulus($|a_{\alpha\beta}|$) of these parameters while marginalizing over the phase factors ($\phi_{\alpha\beta}$) which take care of the sign of these parameters.

Here in figure 5.7 despite of choosing a higher octant *true* value for θ_{23} we get a degeneracy in the lower octant region in the case of $a_{e\mu}$ and $a_{e\tau}$ reconstruction despite of taking $\theta_{23,\ true} = 48.8°$. Even then, the value for maximal mixing (*i.e.*$\theta_{23} = 45°$) lies in the exclusion region. But in the case of a_{ee}, $a_{\mu\mu}$, and $a_{\mu\tau}$ the degeneracy in θ_{23} is lifted when we

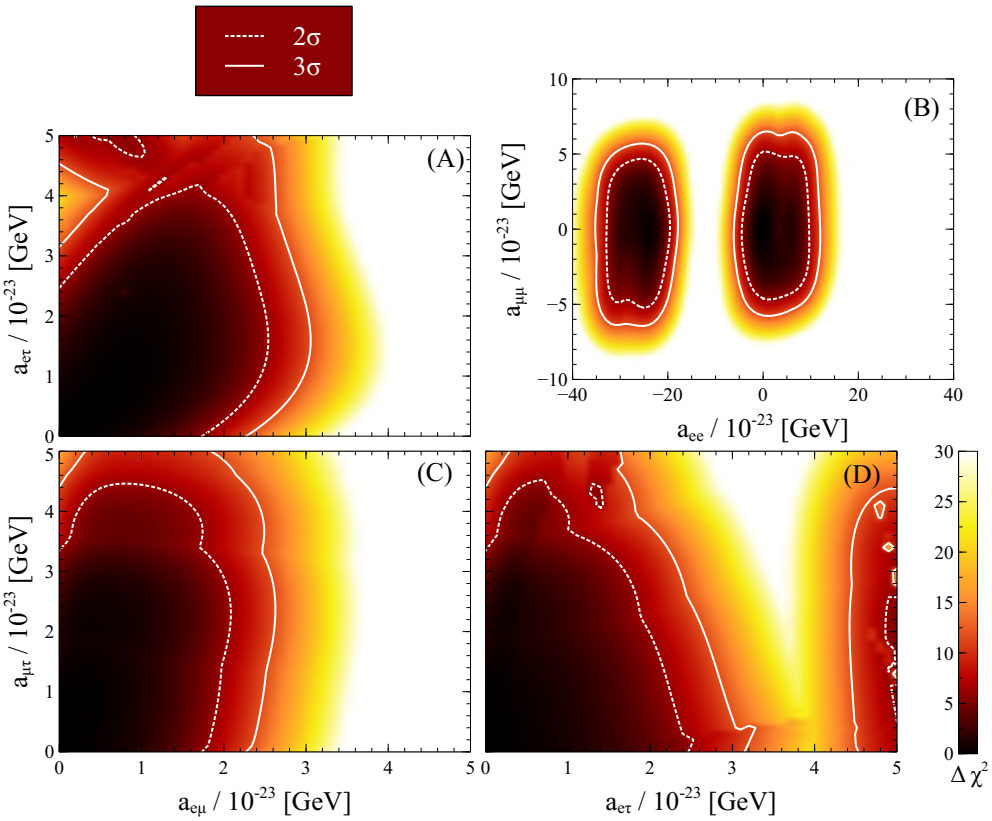

Figure 5.3: Sensitivity of simulated P2O experiment to the LIV parameters pairwise. The solid and dotted lines mark the 3σ and 2σ C.L., respectively.

combine DUNE and P2O simulated data. The allowed region discards the lower octant values.

We already know the bounds on the standard oscillation parameters as shown in table 2.1. If the phenomenon of LIV is true in nature, the P2O simulated data along with DUNE can lift the fake octant degeneracy in θ_{23} in correlation to the LIV parameters.

5.4.3 Bounds on the LIV parameters

We aim to study the likelihood of the P2O experiment to put a bound on the values of the LIV parameters. Figure 5.8 shows the $\Delta\chi^2$ distribution of each test parameter individually at 1σ level. The blue curve gives the distribution for P2O experiment only. Here the values of test a_{ee} have been from -40×10^{-23} GeV to 40×10^{-23} GeV, test $a_{\mu\mu}$ has been varied from -10×10^{-23} GeV to 10×10^{-23} GeV [214]. The off-diagonal parameters have the form $a_{\alpha\beta}e^{i\phi_{\alpha\beta}}$. But as we add the simulated data from the DUNE experiment, we can

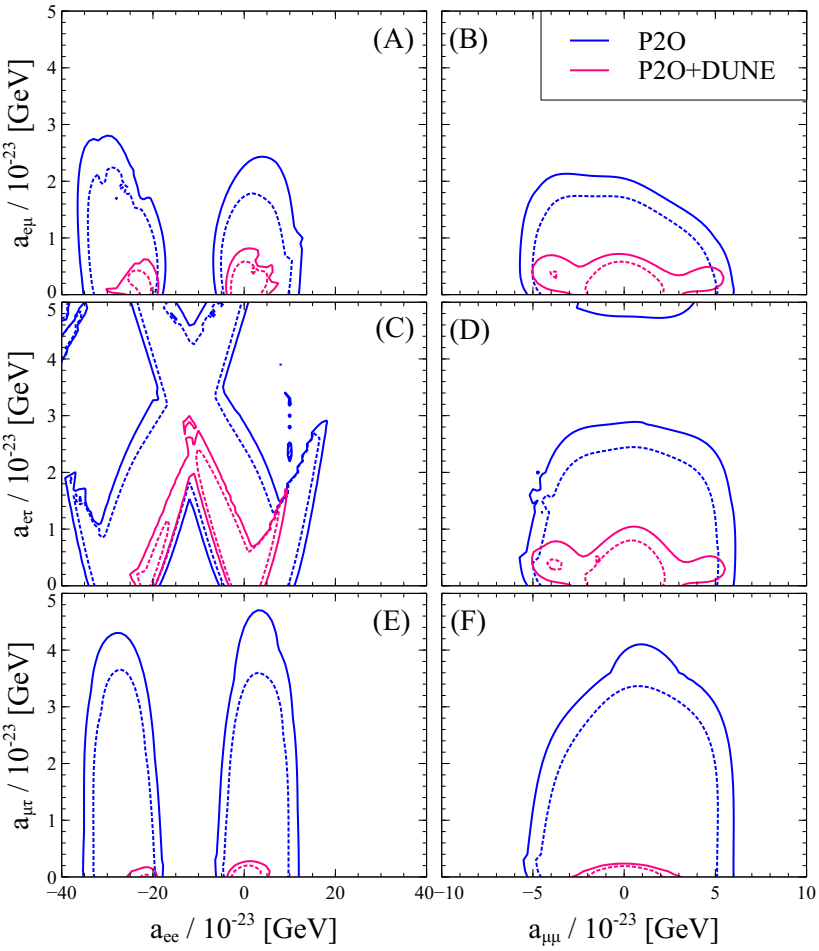

Figure 5.4: Reconstruction of the LIV parameters taken pairwise at 2σ and 3σ (2 D.O.F.) C.L. at P2O (blue) and P2O+DUNE (magenta). The *true* values of the LIV parameters are taken at zero.

see the bound on the LIV parameter values get tighter. Also, we can see that at 95% C.L. the degeneracy on the bounds on a_{ee} is lifted. One significant feature can be observed in the panel where the χ^2 distribution of the test LIV parameter a_{ee} is shown. It has two minima, one at $a_{ee} = 0$ which was anticipated because we have taken the true value of all the LIV parameters to be 0. Another minima occurs at $a_{ee} = -24 \times 10^{-23}$ GeV for P2O experiment and $a_{ee} = -22 \times 10^{-23}$ GeV when the simulated data from P2O and DUNE is combined. This second minima arises due to the interference term in the electron sector in the matter-induced CC potential.

We have given the bounds on the LIV parameters obtained from this study at 95% C.L. in table 5.1. As we can also see from figure 5.8 the steeper χ^2 curves for the combined simulated data from P2O and DUNE have given us tighter constraints in comparison to previous studies. One significant conclusion is the elimination of the degenerate region

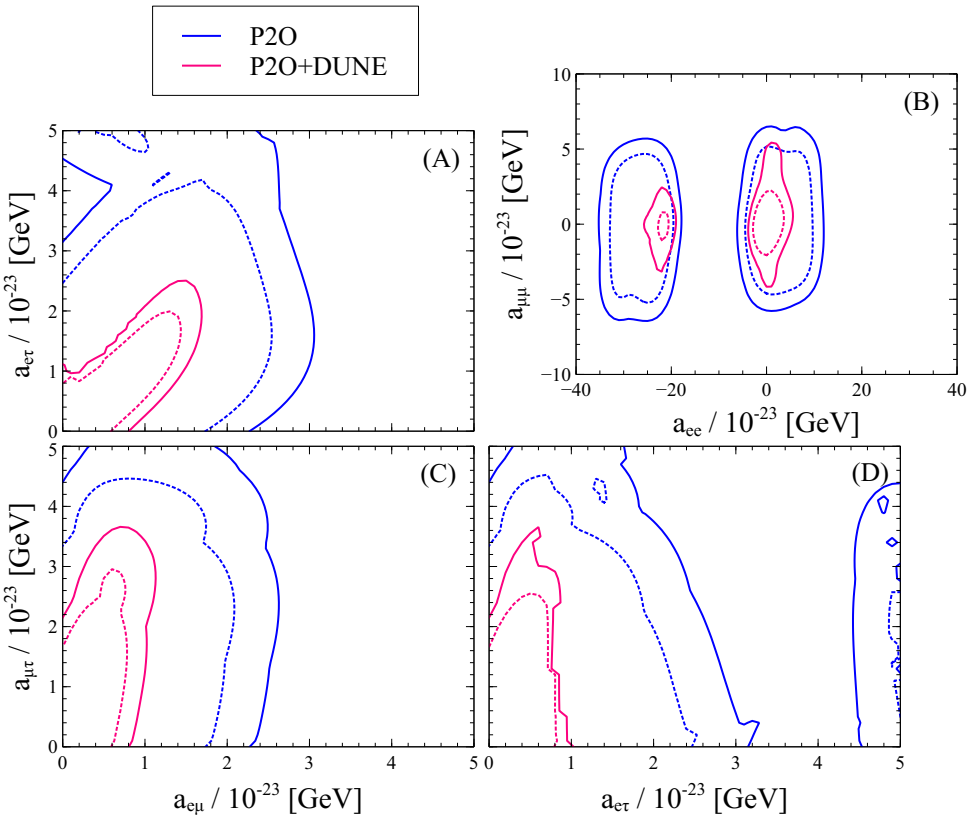

Figure 5.5: Reconstruction of the LIV parameters taken pairwise at 2σ and 3σ (2 D.O.F.) C.L. at P2O (blue) and P2O+DUNE (magenta). The *true* values of the LIV parameters are taken at zero.

in the case of a_{ee}.

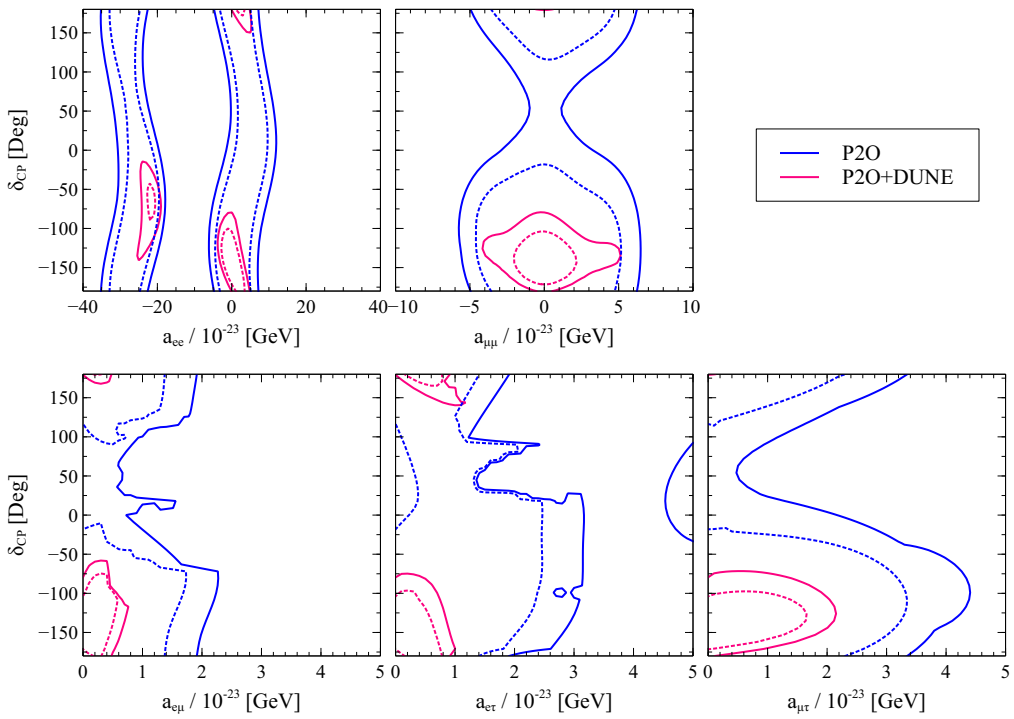

Figure 5.6: Reconstruction of the LIV parameters in correlation to the CP phase δ_{CP} at 2σ and 3σ (2 D.O.F.) C.L at P2O (blue) and P2O+DUNE (magenta). The *true* value of δ_{CP} has been taken to be -0.8π.

Parameter	Existing bounds $(\times 10^{-23})$ [GeV]	Bounds from this work $(\times 10^{-23})$ [GeV]
a_{ee}	$[-25 < a_{ee} < -20] \cup [-2.5 < a_{ee} < 3.2]$	$-2.093 < a_{ee} < 2.728$
$a_{\mu\mu}$	$-3.7 < a_{\mu\mu} < 4.8$	$-1.504 < a_{\mu\mu} < 1.660$
$\lvert a_{e\mu}\rvert$	0.7	0.467
$\lvert a_{e\tau}\rvert$	1.0	0.599
$\lvert a_{\mu\tau}\rvert$	1.7	1.370

Table 5.1: Bounds on the LIV parameters as obtained from the projected LBL data (P2O and DUNE combined) at 95% C.L. in comparison to the bounds shown in [214].

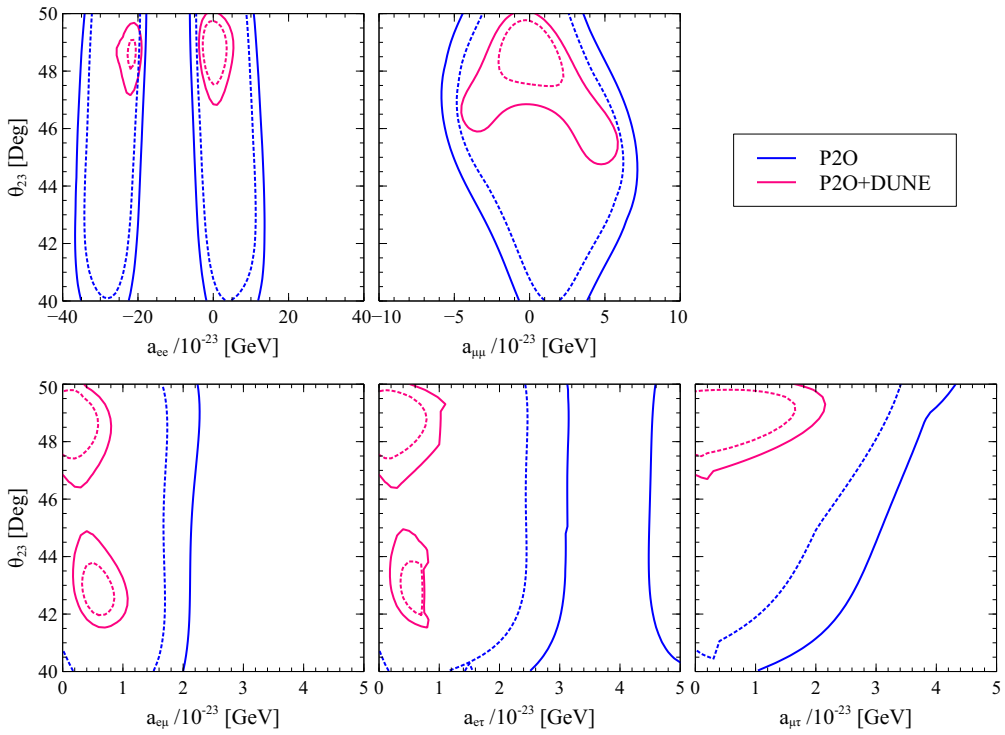

Figure 5.7: Reconstruction of the LIV parameters in correlation to the mixing angle θ_{23} at 2σ and 3σ (2 D.O.F.) C.L at P2O (blue) and P2O+DUNE (magenta). The *true* value of θ_{23} has been taken to be $48.8°$.

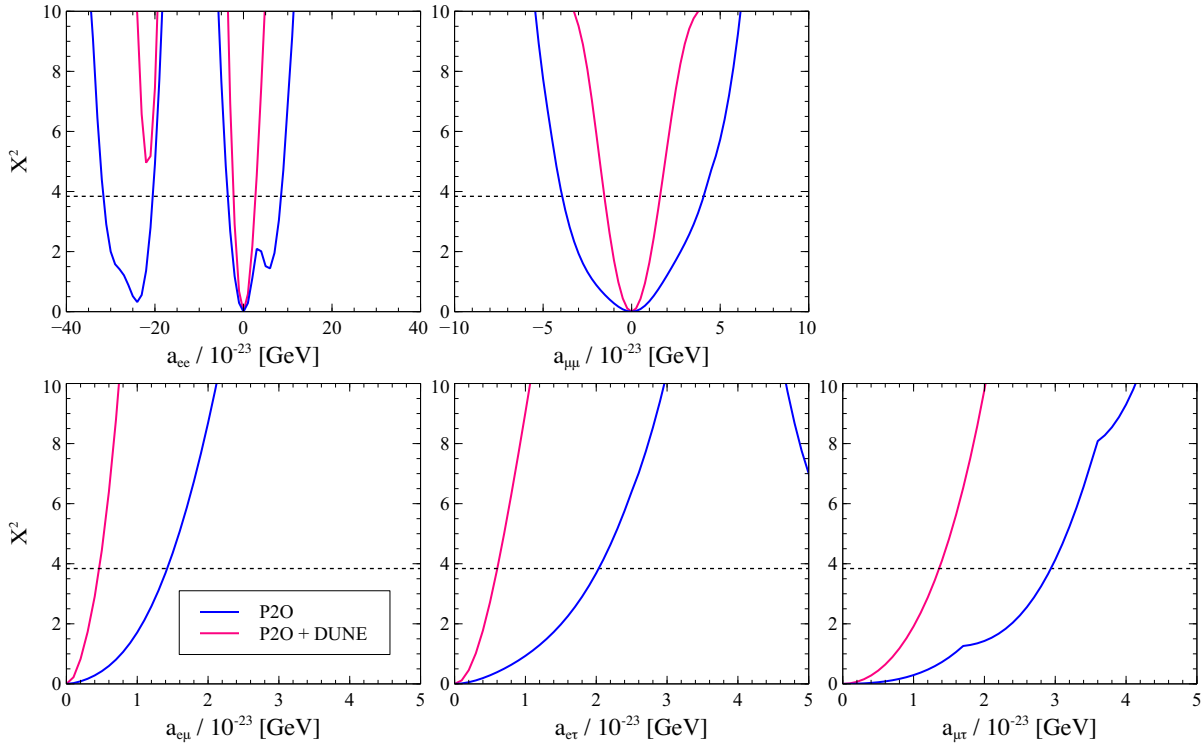

Figure 5.8: Expected sensitivity of DUNE and P2O experiment to the LIV parameters at 1σ level. The black dotted line indicates the 95% C.L.

5.5 Summary

In this chapter, we have discussed the effect of Lorentz violation on neutrinos. We start with the Hamiltonian for the neutrino propagation in the matter in presence of the LIV terms. We check how the non-zero values of LIV parameters $a_{\alpha\beta}$ alter the probability in LBL experiment P2O in different channels in the observable range of energy. We chose the relevant signals, namely, the ν_μ disappearance channel and the ν_e appearance channel for our work. Next, we proceeded to do a $\Delta\chi^2$ analysis to estimate the capability of the future LBL experiments DUNE and P2O to probe the LIV parameters in correlation to each other, pairwise. We have followed the constraints on the LIV parameters from global analyses. We have also studied the potential of the mentioned future experiments to probe the poorly measured oscillation parameters θ_{23} and δ_{CP} in correlation to the LIV parameters. We have concluded that when projected data from DUNE and P2O are combined the bounds on δ_{CP} favors the result from recent global analyses. Also, in correlation to the diagonal terms in $a_{\alpha\beta}$ matrix, the value of θ_{23} favors the higher octant. Finally, we have evaluated how future LBL experiments can probe the LIV parameters individually. We observe a steeper $\Delta\chi^2$ distribution with larger statistics and tabulated the bounds on the parameters at 95% C.L.

Chapter 6

Michel study for medium energy π^+ production

6.1 Introduction:

Currently, a prime focus of neutrino experiments is to answer the open questions in neutrino oscillation. New experimental facilities are being developed to study new physics through the phenomenon of neutrino oscillation. To get better precision in the measurement of the observables, one needs to understand how the neutrinos interact with the detectors, *i.e.*, with the nuclei. A better understanding can lead to the reduction of systematic uncertainty. MINERvA (Main INjector ExpeRiment for v-A) experiment provides crucial information about neutrino-nuclei interaction by using Neutrinos at the Main Injector (NuMI) beam [233] on both heavy and light nuclei.

At different energies of neutrinos the nature of the interaction changes. In the low energy region (< 2 GeV) quasi-elastic (QE) interactions are dominant where the neutrino gets scattered by the entire nucleus instead of its constituent partons and ejects one or more nucleons.

$$\nu_\mu n \rightarrow \mu^- p$$

At a slightly higher energy neutrinos can interact with the nucleons and excite them into a baryon resonance which eventually decays into final state hadrons:

$$\nu_\mu N \rightarrow \mu^- N^*$$

$$N^* \rightarrow \pi N'$$

This process is typically known as resonance production (RES). At energy ($E_\nu \gtrsim 4$ GeV) deep-inelastic scattering (DIS) is the dominant process. In this process, the neutrino scat-

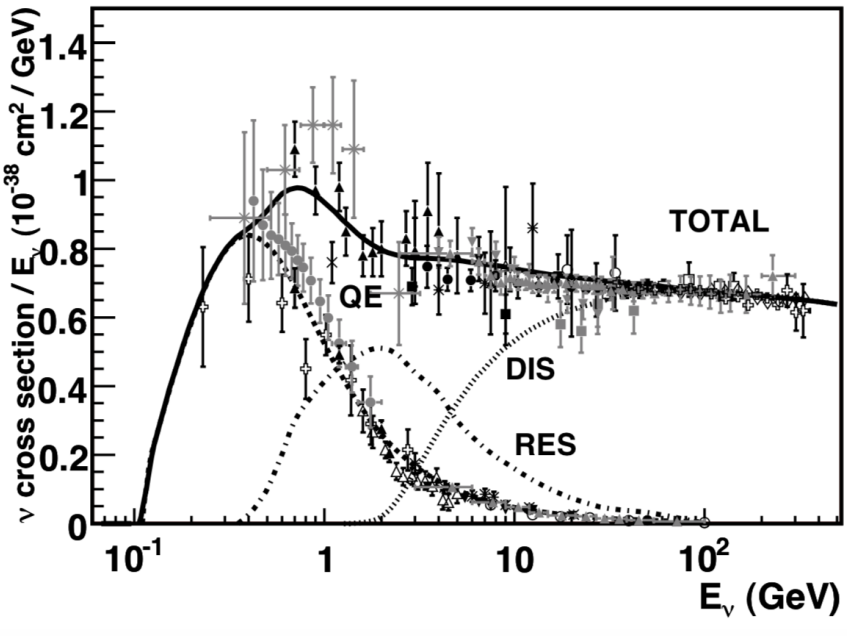

Figure 6.1: Total cross-section for neutrino per nucleon CC interaction with an isoscalar target divided by neutrino energy is plotted as a function of energy. The contribution from different processes is marked [234].

ters off a quark in the nucleon via W or Z boson exchange and produces a lepton and a hadronic system in the final state.

$$\nu_\mu N \rightarrow \mu^- X$$

$$\nu_\mu N \rightarrow \nu_\mu X$$

where X denotes a jet of hadrons. Both charged current (CC) and neutral current (NC) interactions are possible in DIS. The aim of MINERvA experiment is to study these interactions in terms of precise cross-sections. Before going into the details of our study we will briefly discuss the NuMI beam and the MINERvA experiment.

6.1.1 NuMI beam

We will briefly discuss the NuMI beam facility in Fermilab. This beam facility provides neutrino for a number of experiments like Muon g-2, DUNE, NOvA, SBN (which includes the experiments SBND, MicroBooNE, and ICARUS), Mu2e, LArIAT, MINERvA. In this thesis, a number of these experimental data have been used to explore the new physics in the neutrino sector. We emphasize the discussion of the NuMI beam as one of the important neutrino sources used in ongoing and future experiments.

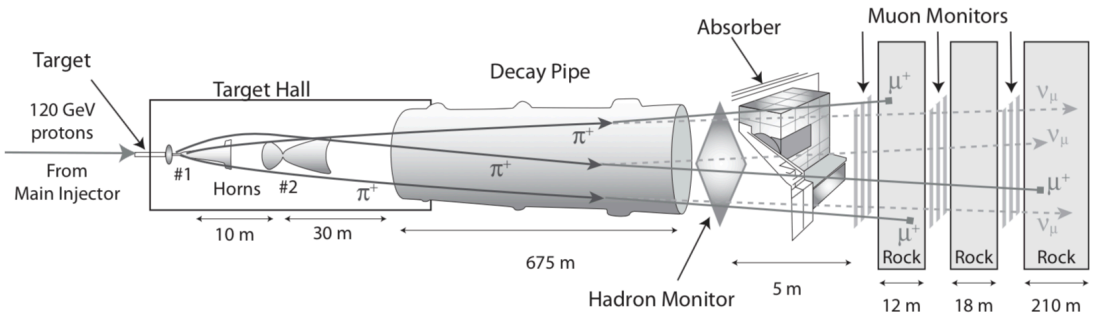

Figure 6.2: Basic elements employed for NuMI beam (not to scale).

The beam is designed such that it can produce neutrinos in the 1-10 GeV range. The Main Injector at Fermilab accelerates the protons at 120 GeV. The proton beam then strikes the Graphite target over an 8.1 or 9.72 μs spill every 2.2 seconds. Incident protons produce charged pions and kaons which are then collimated by a system of a pair of magnetic horns. The stream of the mesons is then passed through a 675 m long He decay pipe. Here, most of the charged particles decay to produce neutrinos and tertiary muons. A total of 240 m of rock downstream obstructs the majority of muons from entering the detectors. The small number of muons that escape are called "rock muons" The magnetic horns can have their polarity changed. For neutrino (anti-neutrino) mode, the horns are in a forward (reverse) horn current setup. The position of the graphite target with respect to the horn and the separation between the two horns can be changed to vary the neutrino peak energy.

6.1.2 MINERvA experiment:

The MINERvA experiment extensively studies the nature of the interaction between the neutrinos generated by the NuMI beam and different nuclear targets (He, C, Pb, Fe, H_2O). Figure 6.3 gives a schematic view of the MINERvA detector. The left panel is a transverse view of a single detector module. The right panel shows the side view of the complete detector which consists of the active tracking region, the nuclear targets, and the electromagnetic and hadronic calorimeters. The "veto wall" upstream blocks the lower energy hadrons from the rock. The horizontal axis of the detector has a 3.4° inclination with respect to the beam direction. In the detector volume, each module is a hexagonal plane where an array of triangular polystyrene scintillator strips with a $1.7cm$ strip-to-strip pitch are arranged. These hexagonal modules have three different orientations (at 0° and $\pm 60^\circ$ relative to the vertical axis) for an efficient 3D reconstruction of the neutrino interaction point and the charged particle track. The scintillator strips have a wavelength-shifting fibre that is read out by a multi-anode PMT. The readout electronics have a time resolution of 3.0 ns to distinguish between different interactions for a single beam spill.

In this work, we have extensively used MINERvA offline framework to do the calculations and also used *Arachne*[1].

[1]Arachne is a web-based tool. The data from the neutrino interaction events in MINERvA are fetched via AJAX from a central server. The client-side JAVA script is then used to draw on the browser window with the help of the draft HTML5 standard. This entire exercise helps the user to visualize an interaction event in MINERvA detector very easily on a web browser [235].

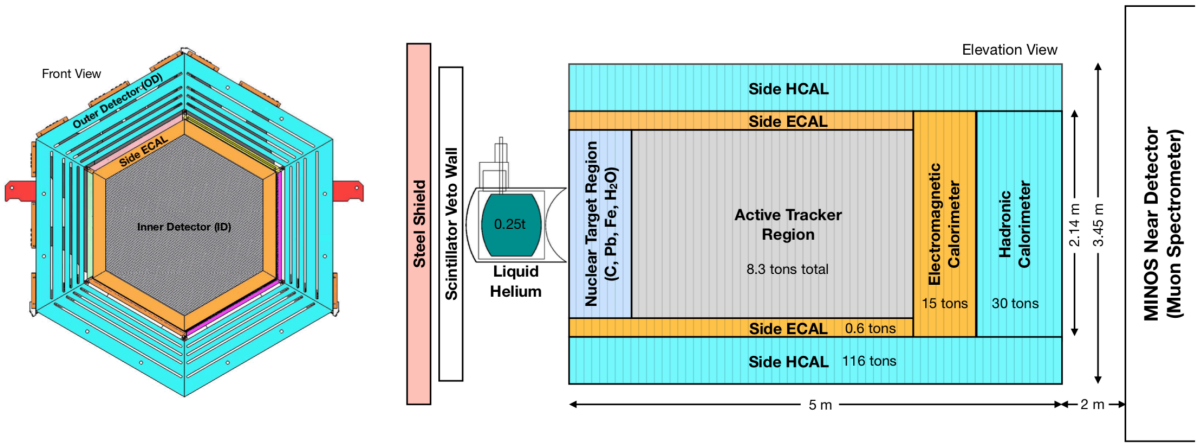

Figure 6.3: A simplified pictorial representation of the detector at rock upstream of the detector hall at Fermilab along the NuMI beamline [73].

6.2 Pion energy reconstruction:

Charged current pion production by neutrinos having energy $\mathcal{O}(GeV)$ is an important signal for current and future long-baseline neutrino oscillation experiments. A correlation between pion kinetic energy and differential cross-section $\frac{d\sigma}{dT_\pi}$ has been estimated by different models. But at pion KE < 50 MeV MINERvA couldn't find any data point to support or discard that model [236]. The pion reconstruction at this energy range becomes extremely complex at MINERvA. We aim to reconstruct these lower energy pions to improve the pion energy resolution. Now, if we focus on non-resonant pion production, we can observe that the low-energy pions decay into muons and further decay into Michel electrons[2].

[2]The muon decay into one electron and a pair of neutrinos with a branching fraction of $\sim 100\%$. The shape of the daughter electron spectrum was first calculated by Louis Michel in 1950, and hence, the electron is named after him [237]

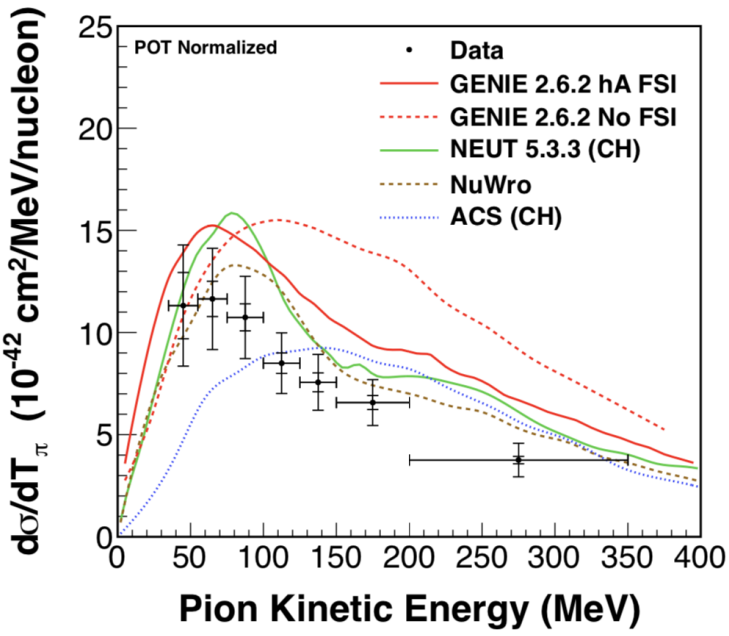

Figure 6.4: The $\frac{d\sigma}{dT_\pi}$ for charged current pion production is plotted as a function of pion kinetic energy. A comparison is done with GENIE, ACS, NEUT, and NuWro models. The inner and outer error bars in data signify the statistical and total uncertainties respectively [236].

Interestingly enough, these Michel electrons leave tracks of energy hits in the detector. The interactions go through the following steps:

- NuMI beam enters the MINERvA detector, interacts with the nucleon, and produces a μ^-, a π^+, and a bunch of Baryons (these may contain interaction neutron or proton and remnant nucleons from the breakup of the target nucleus).

$$\nu_\mu + A \rightarrow \mu^- + A' + \pi^+ + \text{any number of Baryons}$$

- The pions decay into muons.

$$\pi^+ \rightarrow \mu^+ \nu_\mu$$

- The muons further decay into Michel electrons.

$$\mu^+ \rightarrow e^+ \nu_e \overline{\nu_\mu}$$

A schematic diagram of the interaction is given in figure 6.5. Our approach towards improving the pion energy resolution was by studying the Michel tracks.

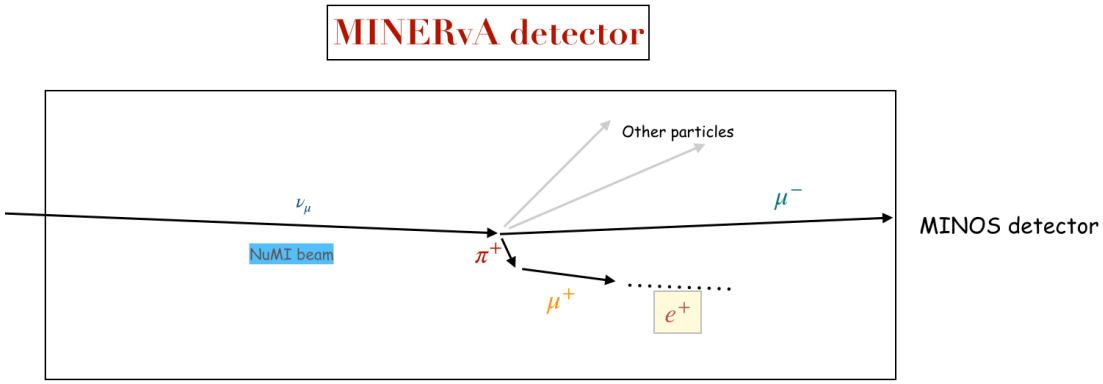

Figure 6.5: Schematic diagram for the interactions leading to Michel electron production.

6.3 Results

To begin with, we tried to find out the correlation between true pion KE and the reconstructed distance between the neutrino interaction vertex and the starting point of the Michel track. The correlation was not well-defined at the lower energy of the pions. A possible explanation could be found in the reconstruction algorithm that calculates the distance. We started by plotting a histogram to get a pictorial representation of the *true* and *reconstructed* distances between the neutrino interaction vertex and the starting point of the Michel track, as can be seen from figure 6.5.

In Fig. 6.6 the x-axis denotes the *true* distance and the y-axis denotes the *reconstructed* distance. Each cell denotes the number of events. The efficiency of the reconstruction algorithm is generally projected as more population along the diagonal of such a plot. But since we can see that there is a significant number of events that are not reconstructed properly, we proceeded to look into the algorithm itself. One should note that only the

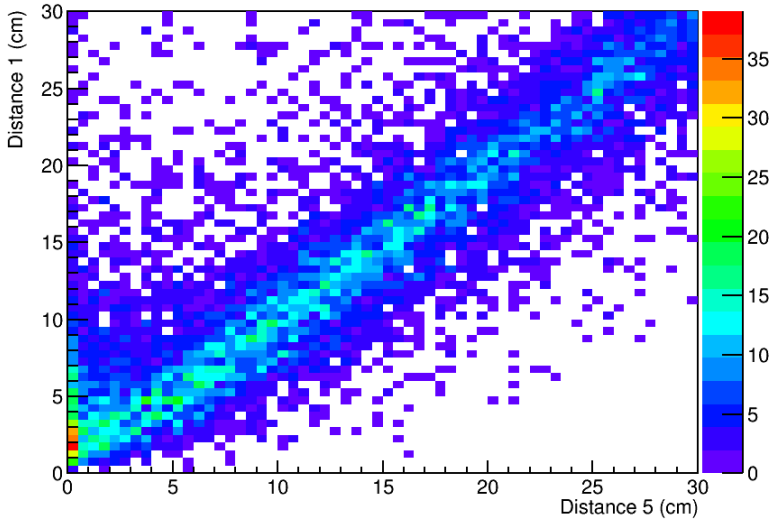

Figure 6.6: A comparison between the *true* and *reconstructed* distances between the neutrino interaction vertex and the starting point of the Michel track. *Distance 5* is the true parameter and *Distance 1* is the reconstructed parameter.

non-resonant pion production events have been considered where the Michel track is closer(<30 cm) to the neutrino interaction vertex to focus on the lower energy pions.

Investigating the reconstruction parameters we observed that the reconstructed transverse position of the Michel electron track is the most responsible factor. To get a clearer understanding the poorly reconstructed events were scanned in *Arachne* and the reasons for mis-reconstruction were explored elaborately. We found the following factors to be responsible for the algorithm to go wrong:

- **Neutrino interaction vertex mis-reconstruction: (24.4%)**

  When a muon neutrino hits the nuclear target in the detector, it emits a muon and a bunch of other particles. The muon track is traced back and the interaction vertex is reconstructed. But there are events where the muon track can't be traced back properly and the vertex is mis-reconstructed. Hence, the distance between the neutrino interaction vertex and the starting point of the Michel electron track is calculated wrongly in 24.4% of cases.

- **Choosing the wrong Michel track end: (17.5%)**

  In Arachne, if we look at an event of pion production at energy less than 50MeV,

we can only see the neutrino interaction vertex and the Michel electron track. Any of the two ends of the track can be the point where the muon has decayed into the Michel electron. The existing algorithm chooses the track end which is nearer to the neutrino interaction vertex. But it happens to be the other end for 17.5% of events.

- **Wrong transverse position due to cross-talks: (22.2%)**

  If the Michel electron has lower energy, the hits on the detectors may have the same order of energy as the background noise. Due to this noise, the algorithm fails to calculate the transverse position of the Michel electron correctly in 22.2% of cases.

- **Wrong Z-position: (11.4%)**

  The reason for the determination of the wrong perpendicular position of the Michel track is as same as the above.

- **High Michel angle: (15.3%)**

  If the Michel track makes a large angle with the Z-axis of the detector, the algorithm tends to fail.

- **Others: (9.2%)**

  In this category, there are events where we were unable to find a reason at all for the bad reconstruction or are a combination of two or more reasons for poor reconstruction mentioned above.

Since none of the factors contributed majorly, we were unable to probe a particular aspect of the reconstruction algorithm. Another alternative approach was taken next. We studied the efficiency and purity of the reconstruction in terms of the parameters corresponding to the above-mentioned factors for mis-reconstruction. Had there been a drastic change, one could cut or discard certain events to improve the signal and make a defined correlation between the pion KE and the distance between the neutrino interaction vertex and the starting point of the Michel track. To make the task more difficult, the efficiency and purity plots turned out to be smooth.

At the end of this exercise, we took a simplistic approach. We plotted the average pion KE for each distance bin and tried to fit a polynomial that will express the pion KE as a function of the distance.

The black curve is a quadratic polynomial function of the form: $y = a_0 + a_1 x + a_2 x^2$. The values of the coefficients are: $a_0 = 25.1562 \pm 4.217, a_1 = 4.0055 \pm 0.1623, a_2 = -0.0132 \pm 0.0013$

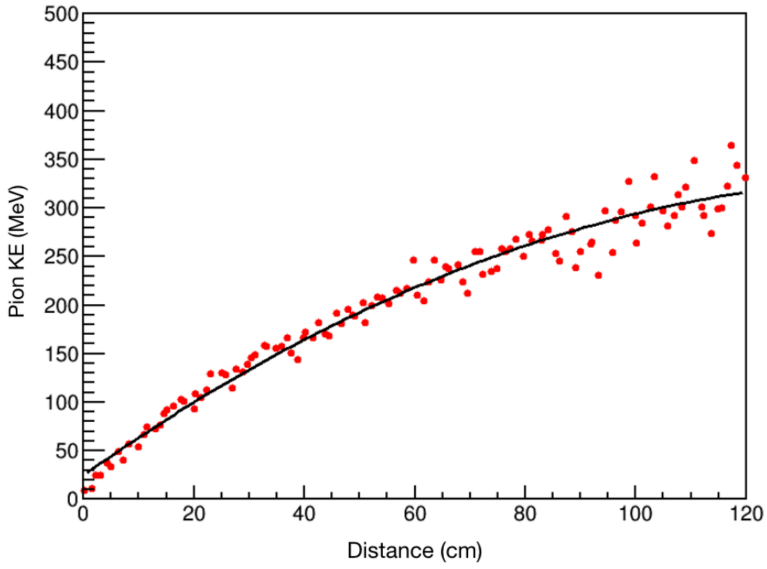

Figure 6.7: Average pion KE plotted for each distance bin and a polynomial is fitted through the data points.

In conclusion, it can be said that the distance reconstruction algorithm fails to reconstruct a significant number of events for lower energy pions. The responsible factors have been probed. But improving any one of those could not make a significant difference in the study. A naive approach could be implemented which is stated in figure 6.7.

6.4 Summary

In this chapter, we briefly discuss about the MINERvA experiment and its physics goals. We particularly focus on the charged pion production in the area of neutrino-nucleus interaction in MINERvA. The efficient reconstruction of lower energy pions in MINERvA becomes complicated. We have proceeded to look into the interactions and found out that there are several reasons why the reconstruction algorithm didn't have more accuracy. We have pinpointed six distinct reasons. But we have been unable to distinguish a single reason for the mis-reconstruction that can improve the algorithm significantly. Finally, we have plotted the average KE of pions for each distance (distance between the neutrino interaction vertex and the pion decay vertex) bin and fitted a polynomial that can give a functional dependence of these two parameters. This study may be extended in the case of anti-neutrino mode, in case of charged current single π^- production and the

event selection can be done in such a manner that bypasses the less efficient event reconstruction. Also, in the case of the π^- production study, to eliminate the background more efficiently, one can put a cut on the lower energy π^+ production events accompanied by Michel electron candidates.

Chapter 7

Conclusion

The research and development in the domain of neutrino experiments have given us an opportunity to study the physics of neutrinos with more precision. In this thesis, we have studied the capabilities of long baseline experiments to study the BSM physics signatures like: the presence of light sterile neutrino, left-right symmetric mass model, and Lorentz invariance violation. We also have studied the neutrino-nucleus interaction in terms of charged pion production in MINERvA. The main conclusion from the various studies is summarised as follows.

7.1 Exploring the new physics phases in $3+1$ scenario in neutrino oscillation experiments

In Chapter 3, we have considered the presence of an eV-scale sterile neutrino (the so-called 3+1 scenario which might turn out to be a possible resolution of the short baseline neutrino oscillation anomalies) and have analyzed how the present and future long baseline experiments T2K, NOvA, DUNE, and T2HK can potentially probe the additional CP phases. We discuss how the three CP phases, namely δ_{13}, δ_{24} and δ_{34} can individually affect the oscillation channels under consideration and appear in the probability expression. In light of the constraints on the active-sterile mixing from the global analysis, we estimate how the LBL experiments can probe the parameter spaces associated to the CP phases, by taking a pair of CP phases at a time. Though $\nu_\mu \to \nu_e$ oscillation channel contributes the most in probing these parameter-spaces, $\nu_\mu \to \nu_\mu$ and to a lesser extent $\nu_\mu \to \nu_\tau$ channel also help in exploring the $\delta_{24} - \delta_{34}$ parameter space in particular. By marginalizing over all other parameters we then show how the three individual CP phases can be reconstructed for all possible true values in the whole range of $[-\pi, \pi]$. We

find that δ_{24} and δ_{34} cannot be reconstructed very efficiently by DUNE and also even after adding data from NOvA and T2K. But adding T2HK data removes much of the degeneracies and the uncertainties in reconstruction become much less. We found that if the active-sterile mixing angles turn out to be lying close to their current upper limits, the enhanced sensitivities to the associated phases make the reconstructions of δ_{24} and δ_{34} much better. In contrast, the reconstruction of the standard CP phase δ_{13} is much better even in presence of a light sterile neutrino and this conclusion is almost independent of the size of active-sterile mixing. We then analyze how efficiently the experiments can probe all the parameter spaces associated with one CP phase and one active-sterile mixing angle. It turns out that the parameter regions connected to the angle θ_{14} can be probed relatively better than those related to the other two mixing angles. Finally, we briefly show how the relevant parameter spaces in $0\nu\beta\beta$ get modified in light of the active-sterile constraints used in this analysis. We have seen that the $3+1$ scenario has better agreement with the GERDA prediction for the effective mass of the $0\nu\beta\beta$ process, in contrast with the $3+0$ scenario.

The recent data published by MicroBooNE experiment [238] does not support the existence of light sterile neutrinos conclusively. It opens aspects of new phenomenology such as the decay of heavy sterile neutrinos or new resonance matter effects in neutrinos. Such possibilities can be explored in future experiments like SBN, ICARUS, and DUNE.

7.2 Probing the Left-Right Symmetric Model in neutrino oscillation data

In Chapter 4, we have briefly discussed about the Left-Right symmetric model, one of the popular neutrino mass models that naturally incorporates the seesaw mechanism. We have identified the relevant LRSM parameters M_ξ (mass of the triplet scalar) and the Higgs-triplet coupling λ_ϕ and discussed how they are related to the couplings in NC NSI interactions realized by the dimension-6 operators in a low energy effective field theory approach. We have extracted the available NOvA and T2K data and have used the GLoBES framework to estimate the LRSM parameters by probing the NSI couplings. We illustrated how the allowed regions for the LRSM parameter ratio $((M_\xi/\lambda_\phi)^2)$ vary as functions of the poorly measured standard oscillation parameters θ_{23} and the Dirac CP phase $\delta_{\rm CP}$. We pointed out how NOvA is much more constraining for θ_{23} and how the two experiments are actually complementary for $\delta_{\rm CP}$. Depending on the physics capabilities of the two experiments, we are able to estimate restrictive upper limits on the LRSM

parameter. We report this constraint as a function of the lightest neutrino mass (m_1) too. We have seen that the parameter $M_\xi/|\lambda_\phi|$ is steeply constrained when $m_1 \lesssim 50$ meV and at $m_1 \gtrsim 50$ meV the upper limit varies less (around $M_\xi/|\lambda_\phi| \sim 3.5 \times 10^{12}$).
In this study, we take M_ξ to be the relevant parameter for the phenomenon of LRSM. The mass of the scalar triplet can also be measured in the multi-lepton searches in the upcoming collider experiments. The constraint on the scalar triplet mass will be able to shed more light on LRSM.

7.3 Investigating the new physics scenario in P2O experiment

We study Lorentz Invariance Violation (LIV) through Planck suppression in long baseline experiments in Chapter 5. Initially we discuss how LIV affects the Hamiltonian associated with neutrino oscillation. Then we further proceed to check the effects of the relevant LIV parameters in terms of oscillation probability (both appearance and disappearance channels). We have used simulated data for P2O and DUNE experiments to do the relevant calculations. The main aim of this project was to check that if LIV is true in nature can we put a bound on the relevant parameter space using the long baseline experiment data. We have illustrated how the LIV parameter space can be reconstructed using P2O data. We observe a degeneracy in the value of a_{ee} consistently in correlation to other LIV parameters. Adding DUNE data does not lift the degeneracy, but shrinks the bounds on the parameter space significantly. We have also illustrated the reconstruction of the LIV parameters in correlation to the poorly measured oscillation parameter (θ_{23} and δ_{CP}). We note that the artificial degeneracy in θ_{23} is lifted when the reconstruction is done with correlation to $a_{ee}, a_{\mu\mu}$ and $a_{\mu\tau}$ combining DUNE and P2O data and our analysis favors the higher octant space for θ_{23}. Finally, we investigate the sensitivity of DUNE and P2O experiments to the LIV parameters individually and get an idea of the bounds of these parameters at 95% C.L. The bounds on a_{ee} are found to be $-2.093 < a_{ee} < 2.728$ which eliminates the degenerate region extracted from previous similar analyses. We also found improvement in the values of the bounds on other LIV parameters.

7.4 Michel study for medium energy π^+ production

MINERvA is a dedicated neutrino-nucleus interaction experiment that can provide crucial information for the oscillation experiments in terms of the physics involved in the

interaction with the detector as well as with matter. In Chapter 6, we mainly focus on the π^+ production which is widely used as a signal for the oscillation experiments. The MINERvA detector fails to reconstruct the lower energy pions efficiently. We study these lower energy pions through Michel electrons and study the interactions event-by-event to find out the reason for poor reconstructions: the neutrino interaction vertex position mis-reconstruction, choosing wrong Michel track end, mis-reconstruction in transverse and longitudinal position of Michel electron are to name a few. We have further studied the efficiency and purity of relevant parameters to look for a sharp change in them which could guide us to improve the reconstruction algorithm. Failing to pin-point a particular parameter we did an average pion KE vs distance (between the neutrino interaction vertex and Michel track end) plot and tried to fit a polynomial which can give us a more accurate pion KE if we know the relevant distance through event reconstruction. One can look further into the reconstruction algorithm itself to improve the lower energy pion reconstruction in MINERvA. A more precise reconstruction algorithm may help in the study of the kinematics of the nuclear effects on the neutrino-nucleus interactions directly.

Bibliography

[1] W. Pauli, Cambridge Monogr.Part.Phys.Nucl.Phys.Cosmol.,14,1 (2000).

[2] Solvay Conference, (1933).

[3] E. Fermi, Z. Phys. **88**, 161 (1934).

[4] E. Fermi, Nuovo Cim. **11**, 1 (1934), [,535(1934)].

[5] G. Gamow and E. Teller, Phys. Rev. **49**, 895 (1936).

[6] B. Pontecorvo, Phys. Rev. **72**, 246 (1947).

[7] H. Bethe and R. Peierls, Nature **133**, 532 (1934).

[8] F. Reines, C. L. Cowan, F. B. Harrison, A. D. McGuire, and H. W. Kruse, Phys. Rev. **117**, 159 (1960).

[9] T. D. Lee and C.-N. Yang, Phys. Rev. **104**, 254 (1956).

[10] C. S. Wu, E. Ambler, R. W. Hayward, D. D. Hoppes, and R. P. Hudson, Phys. Rev. **105**, 1413 (1957).

[11] R. P. Feynman and M. Gell-Mann, Phys. Rev. **109**, 193 (1958).

[12] E. C. G. Sudarshan and R. e. Marshak, Phys. Rev. **109**, 1860 (1958).

[13] J. J. Sakurai, Nuovo Cim. **7**, 649 (1958).

[14] L. D. Landau, Nucl. Phys. **3**, 127 (1957).

[15] T. D. Lee and C.-N. Yang, Phys. Rev. **105**, 1671 (1957).

[16] A. Salam, Nuovo Cim. **5**, 299 (1957).

[17] M. Goldhaber, L. Grodzins, and A. W. Sunyar, Phys. Rev. **109**, 1015 (1958).

[18] G. Danby, J. M. Gaillard, K. A. Goulianos, L. M. Lederman, N. B. Mistry, M. Schwartz, and J. Steinberger, Phys. Rev. Lett. **9**, 36 (1962).

[19] B. Pontecorvo, Sov. Phys. JETP **6**, 429 (1957), [Zh. Eksp. Teor. Fiz.33,549(1957)].

[20] B. Pontecorvo, Sov. Phys. JETP **10**, 1236 (1960), [Zh. Eksp. Teor. Fiz.37,1751(1959)].

[21] Z. Maki, M. Nakagawa, and S. Sakata, Progress of Theoretical Physics **28**(5), 870 (1962).

[22] B. Pontecorvo, Sov. Phys. JETP **26**, 984 (1968), [Zh. Eksp. Teor. Fiz.53,1717(1967)].

[23] V. N. Gribov and B. Pontecorvo, Phys. Lett. **B28**, 493 (1969).

[24] S. Eliezer and A. R. Swift, Nucl. Phys. B **105**, 45 (1976).

[25] H. Fritzsch and P. Minkowski, Phys. Lett. B **62**, 72 (1976).

[26] S. M. Bilenky and B. Pontecorvo, Phys. Rept. **41**, 225 (1978).

[27] K. Kodama *et al.* (DONUT), Phys. Lett. **B504**, 218 (2001), hep-ex/0012035.

[28] T. J. Haines *et al.*, Phys. Rev. Lett. **57**, 1986 (1986).

[29] M. Ambrosio *et al.* (MACRO), Phys. Lett. **B434**, 451 (1998), hep-ex/9807005.

[30] K. S. Hirata *et al.* (Kamiokande-II), Phys. Lett. **B205**, 416 (1988), [,447(1988)].

[31] Y. Ashie *et al.* (Super-Kamiokande), Phys. Rev. **D71**, 112005 (2005), hep-ex/0501064.

[32] Y. Fukuda *et al.* (Super-Kamiokande), Phys. Rev. Lett. **81**, 1562 (1998), hep-ex/9807003.

[33] B. Aharmim *et al.* (SNO), Phys. Rev. **C72**, 055502 (2005), nucl-ex/0502021.

[34] L. Wolfenstein, Phys. Rev. **D17**, 2369 (1978).

[35] S. P. Mikheev and A. Y. Smirnov, Sov. Phys. Usp. **30**, 759 (1987).

[36] T. Kajita and A. B. McDonald, *For the discovery of neutrino oscillations, which shows that neutrinos have mass*, the Nobel Prize in Physics 2015.

[37] S. Schael *et al.* (SLD Electroweak Group, DELPHI, ALEPH, SLD, SLD Heavy Flavour Group, OPAL, LEP Electroweak Working Group, L3), Phys. Rept. **427**, 257 (2006), hep-ex/0509008.

[38] P. Minkowski, Phys. Lett. **B67**, 421 (1977).

[39] R. N. Mohapatra and G. Senjanovic, Phys. Rev. Lett. **44**, 912 (1980).

[40] A. D. Sakharov, Pisma Zh. Eksp. Teor. Fiz. **5**, 32 (1967), [Usp. Fiz. Nauk161,61(1991)].

[41] M. Fukugita and T. Yanagida, Phys. Lett. **B174**, 45 (1986).

[42] M. Flanz, E. A. Paschos, and U. Sarkar, Phys. Lett. B **345**, 248 (1995), [Erratum: Phys.Lett.B 384, 487–487 (1996), Erratum: Phys.Lett.B 382, 447–447 (1996)], hep-ph/9411366.

[43] J. A. Harvey and M. S. Turner, Phys. Rev. D **42**, 3344 (1990).

[44] J. N. Bahcall, M. H. Pinsonneault, and S. Basu, Astrophys. J. **555**, 990 (2001), astro-ph/0010346.

[45] J. N. Bahcall and A. M. Serenelli, Astrophys. J. **626**, 530 (2005), astro-ph/0412096.

[46] J. N. Bahcall, A. M. Serenelli, and S. Basu, Astrophys. J. **621**, L85 (2005), astro-ph/0412440.

[47] C. Giunti and C. W. Kim, *Fundamentals of Neutrino Physics and Astrophysics* (2007).

[48] J. N. Bahcall and R. K. Ulrich, Rev. Mod. Phys. **60**, 297 (1988).

[49] K. Nakamura *et al.* (Particle Data Group), J. Phys. G **37**, 075021 (2010).

[50] J. P. Cravens *et al.* (Super-Kamiokande), Phys. Rev. D **78**, 032002 (2008), 0803.4312.

[51] Q. R. Ahmad *et al.* (SNO), Phys. Rev. Lett. **89**, 011301 (2002), nucl-ex/0204008.

[52] B. T. Cleveland, T. Daily, R. Davis, Jr., J. R. Distel, K. Lande, C. K. Lee, P. S. Wildenhain, and J. Ullman, Astrophys. J. **496**, 505 (1998).

[53] J. N. Abdurashitov *et al.* (SAGE), J. Exp. Theor. Phys. **95**, 181 (2002), astro-ph/0204245.

[54] W. Hampel *et al.* (GALLEX), Phys. Lett. B **447**, 127 (1999).

[55] M. Altmann *et al.* (GNO), Phys. Lett. B **490**, 16 (2000), hep-ex/0006034.

[56] M. Agostini *et al.* (BOREXINO), Nature **587**, 577 (2020), 2006.15115.

[57] V. Barger, D. Marfatia, and K. Whisnant, Int. J. Mod. Phys. **E12**, 569 (2003), hep-ph/0308123.

[58] T. K. Gaisser and M. Honda, Ann. Rev. Nucl. Part. Sci. **52**, 153 (2002), hep-ph/0203272.

[59] V. Barger, D. Marfatia, and K. Whisnant, *The physics of neutrinos* (Princeton Univ. Pr., Princeton, USA, 2012), ISBN 9780691128535, URL http://press.princeton.edu/titles/9913.html.

[60] K. S. Hirata *et al.* (Kamiokande-II), Phys. Lett. B **205**, 416 (1988).

[61] M. C. Sanchez *et al.* (Soudan 2), Phys. Rev. D **68**, 113004 (2003), hep-ex/0307069.

[62] W. W. M. Allison *et al.* (Soudan-2), Phys. Lett. B **449**, 137 (1999), hep-ex/9901024.

[63] M. Ambrosio *et al.* (MACRO), Phys. Lett. B **478**, 5 (2000), hep-ex/0001044.

[64] M. Ambrosio *et al.* (MACRO), Eur. Phys. J. C **36**, 323 (2004).

[65] V. D. Barger, A. M. Gago, D. Marfatia, W. J. C. Teves, B. P. Wood, and R. Zukanovich Funchal, Phys. Rev. D **65**, 053016 (2002), hep-ph/0110393.

[66] M. Apollonio *et al.* (CHOOZ), Phys. Lett. B **466**, 415 (1999), hep-ex/9907037.

[67] M. Apollonio *et al.* (CHOOZ), Eur. Phys. J. C **27**, 331 (2003), hep-ex/0301017.

[68] S. Ahmed *et al.* (ICAL), Pramana **88**(5), 79 (2017), 1505.07380.

[69] A. Blanchet, Phys. At. Nucl. **84**(4), 519 (2021).

[70] K. Abe *et al.* (T2K), Nucl. Instrum. Meth. A **659**, 106 (2011), 1106.1238.

[71] Y. Fukuda *et al.* (Super-Kamiokande), Nucl. Instrum. Meth. A **501**, 418 (2003).

[72] R. Acciarri *et al.* (MicroBooNE), JINST **12**(02), P02017 (2017), 1612.05824.

[73] L. Aliaga *et al.* (MINERvA), Nucl. Instrum. Meth. A **743**, 130 (2014), 1305.5199.

[74] S. Amerio *et al.* (ICARUS), Nucl. Instrum. Meth. A **527**, 329 (2004).

[75] P. A. Machado, O. Palamara, and D. W. Schmitz, Ann. Rev. Nucl. Part. Sci. **69**, 363 (2019), 1903.04608.

[76] P. Adamson *et al.*, Nucl. Instrum. Meth. A **806**, 279 (2016), 1507.06690.

[77] L. A. Mikaelyan, Phys. Atom. Nucl. **65**, 1173 (2002), [Yad. Fiz.65,1206(2002)], hep-ph/0210047.

[78] C. Bemporad, G. Gratta, and P. Vogel, Rev. Mod. Phys. **74**, 297 (2002), hep-ph/0107277.

[79] F. Ardellier *et al.* (Double Chooz) (2006), hep-ex/0606025.

[80] X. Guo *et al.* (Daya Bay) (2007), hep-ex/0701029.

[81] J. K. Ahn *et al.* (RENO) (2010), 1003.1391.

[82] K. Hirata *et al.* (Kamiokande-II), Phys. Rev. Lett. **58**, 1490 (1987).

[83] R. M. Bionta *et al.*, Phys. Rev. Lett. **58**, 1494 (1987).

[84] H. Yuksel, S. Ando, and J. F. Beacom, Phys. Rev. C **74**, 015803 (2006), astro-ph/0509297.

[85] J. F. Beacom and L. E. Strigari, Phys. Rev. C **73**, 035807 (2006), hep-ph/0508202.

[86] P. Anselmann *et al.* (GALLEX), Phys. Lett. B **357**, 237 (1995), [Erratum: Phys.Lett.B 361, 235–236 (1995)].

[87] M. G. Aartsen *et al.* (IceCube), JINST **12**(03), P03012 (2017), 1612.05093.

[88] S. Adrian-Martinez *et al.* (KM3Net), J. Phys. G **43**(8), 084001 (2016), 1601.07459.

[89] M. Ageron *et al.* (ANTARES), Nucl. Instrum. Meth. A **656**, 11 (2011), 1104.1607.

[90] B. Pontecorvo, Zh. Eksp. Teor. Fiz. **34**, 247 (1957).

[91] Z. Maki, M. Nakagawa, and S. Sakata, Prog. Theor. Phys. **28**, 870 (1962).

[92] Y. Fukuda *et al.* (Super-Kamiokande), Phys. Rev. Lett. **81**, 1562 (1998), hep-ex/9807003.

[93] A. Aguilar-Arevalo *et al.* (LSND), Phys.Rev. **D64**, 112007 (2001), hep-ex/0104049.

[94] C. Hati, S. Patra, P. Pritimita, and U. Sarkar, Frontiers in Physics **6**, 19 (2018), ISSN 2296-424X, URL https://www.frontiersin.org/article/10.3389/fphy.2018.00019.

[95] S. Nussinov, Phys. Lett. **B63**, 201 (1976).

[96] B. Kayser, Phys. Rev. **D24**, 110 (1981).

[97] K. Kiers, S. Nussinov, and N. Weiss, Phys. Rev. **D53**, 537 (1996), hep-ph/9506271.

[98] C. Giunti, C. W. Kim, and U. W. Lee, Phys. Rev. **D44**, 3635 (1991).

[99] C. Giunti and C. W. Kim, Phys. Rev. **D58**, 017301 (1998), hep-ph/9711363.

[100] J. Schechter and J. W. F. Valle, Phys. Rev. **D22**, 2227 (1980).

[101] C. Giunti, C. W. Kim, and M. Monteno, Nucl. Phys. B **521**, 3 (1998), hep-ph/9709439.

[102] E. K. Akhmedov, R. Johansson, M. Lindner, T. Ohlsson, and T. Schwetz, JHEP **0404**, 078 (2004), hep-ph/0402175.

[103] T. Araki *et al.* (KamLAND), Phys. Rev. Lett. **94**, 081801 (2005), hep-ex/0406035.

[104] A. Gago, M. Guzzo, P. de Holanda, H. Nunokawa, O. Peres, *et al.*, Phys.Rev. **D65**, 073012 (2002), hep-ph/0112060.

[105] P. Adamson *et al.* (MINOS), Phys.Rev.Lett. **112**, 191801 (2014), 1403.0867.

[106] F. P. An *et al.* (Daya Bay), Phys. Rev. Lett. **108**, 171803 (2012), 1203.1669.

[107] J. K. Ahn *et al.* (RENO), Phys. Rev. Lett. **108**, 191802 (2012), 1204.0626.

[108] Y. Abe *et al.* (Double Chooz Collaboration), JHEP **1410**, 086 (2014), 1406.7763.

[109] Y. Itow *et al.* (T2K), in *Neutrino oscillations and their origin. Proceedings, 3rd International Workshop, NOON 2001, Kashiwa, Tokyo, Japan, December 508, 2001* (2001), pp. 239–248, hep-ex/0106019, URL http://alice.cern.ch/format/showfull?sysnb=2258620.

[110] D. S. Ayres *et al.* (NOvA) (2004), hep-ex/0503053.

[111] P. Adamson *et al.* (NOvA) (2016), 1601.05022.

[112] T. Akiri *et al.* (LBNE) (2011), 1110.6249.

[113] R. Acciarri *et al.* (DUNE) (2015), 1512.06148.

[114] K. Abe *et al.* (Hyper-Kamiokande Proto-Collaboration), PTEP **2015**, 053C02 (2015), 1502.05199.

[115] P. de Salas, D. Forero, S. Gariazzo, P. Martínez-Miravé, O. Mena, C. Ternes, M. Tórtola, and J. Valle (2020), 2006.11237.

[116] B. Abi *et al.* (DUNE) (2020), 2002.03005.

[117] M. Dentler, I. Esteban, J. Kopp, and P. Machado, Phys. Rev. D **101**(11), 115013 (2020), 1911.01427.

[118] J. Asaadi, E. Church, R. Guenette, B. J. P. Jones, and A. M. Szelc, Phys. Rev. D **97**(7), 075021 (2018), 1712.08019.

[119] C.-H. V. Chang, C.-R. Chen, S.-Y. Ho, and S.-Y. Tseng, Phys. Rev. D **104**(1), 015030 (2021), 2102.05012.

[120] S. Vergani, N. W. Kamp, A. Diaz, C. A. Argüelles, J. M. Conrad, M. H. Shaevitz, and M. A. Uchida, Phys. Rev. D **104**(9), 095005 (2021), 2105.06470.

[121] A. Diaz, C. A. Argüelles, G. H. Collin, J. M. Conrad, and M. H. Shaevitz, Phys. Rept. **884**, 1 (2020), 1906.00045.

[122] M. G. Aartsen *et al.* (IceCube), Phys. Rev. D **102**(5), 052009 (2020), 2005.12943.

[123] A. Osipowicz *et al.* (KATRIN) (2001), hep-ex/0109033.

[124] M. Antonello *et al.* (LAr1-ND, ICARUS-WA104, MicroBooNE) (2015), 1503.01520.

[125] Y. J. Ko *et al.* (NEOS), Phys. Rev. Lett. **118**(12), 121802 (2017), 1610.05134.

[126] Y. Abreu *et al.* (SoLid), JINST **12**(04), P04024 (2017), 1703.01683.

[127] A. P. Serebrov *et al.* (NEUTRINO-4), Pisma Zh. Eksp. Teor. Fiz. **109**(4), 209 (2019), 1809.10561.

[128] J. Ashenfelter *et al.* (PROSPECT), Phys. Rev. Lett. **121**(25), 251802 (2018), 1806.02784.

[129] N. Allemandou *et al.* (STEREO), JINST **13**(07), P07009 (2018), 1804.09052.

[130] H. Almazán *et al.* (STEREO), Phys. Rev. D **102**(5), 052002 (2020), 1912.06582.

[131] I. Alekseev *et al.* (DANSS), Phys. Lett. B **787**, 56 (2018), 1804.04046.

[132] C. Rott (JSNS2), J. Phys. Conf. Ser. **1468**(1), 012176 (2020).

[133] T. Maruyama (JSNS2), *JSNS^2 Experiment*, talk at Neutrino2020, June, 2020. "https://indico.fnal.gov/event/43209/contributions/187854/attachments/129166/159526/Neutrino2020_JSNS2_v3.pdf" (2020).

[134] N. Klop and A. Palazzo, Phys. Rev. **D91**(7), 073017 (2015), 1412.7524.

[135] J. M. Berryman, A. de Gouvêa, K. J. Kelly, and A. Kobach, Phys. Rev. D **92**(7), 073012 (2015), 1507.03986.

[136] R. Gandhi, B. Kayser, M. Masud, and S. Prakash, JHEP **11**, 039 (2015), 1508.06275.

[137] A. Palazzo, Phys. Lett. B **757**, 142 (2016), 1509.03148.

[138] S. K. Agarwalla, S. S. Chatterjee, A. Dasgupta, and A. Palazzo, JHEP **02**, 111 (2016), 1601.05995.

[139] S. K. Agarwalla, S. S. Chatterjee, and A. Palazzo, JHEP **09**, 016 (2016), 1603.03759.

[140] S. K. Agarwalla, S. S. Chatterjee, and A. Palazzo, Phys. Rev. Lett. **118**(3), 031804 (2017), 1605.04299.

[141] D. Dutta, R. Gandhi, B. Kayser, M. Masud, and S. Prakash (2016), 1607.02152.

[142] J. Rout, M. Masud, and P. Mehta, Phys. Rev. D **95**(7), 075035 (2017), 1702.02163.

[143] K. J. Kelly, Phys. Rev. D **95**(11), 115009 (2017), 1703.00448.

[144] M. Ghosh, S. Gupta, Z. M. Matthews, P. Sharma, and A. G. Williams, Phys. Rev. D **96**(7), 075018 (2017), 1704.04771.

[145] S. Choubey, D. Dutta, and D. Pramanik, Phys. Rev. D **96**(5), 056026 (2017), 1704.07269.

[146] P. Coloma, D. V. Forero, and S. J. Parke, JHEP **07**, 079 (2018), 1707.05348.

[147] J. Tang, Y. Zhang, and Y.-F. Li, Phys. Lett. B **774**, 217 (2017), 1708.04909.

[148] S. Choubey, D. Dutta, and D. Pramanik, Eur. Phys. J. C **78**(4), 339 (2018), 1711.07464.

[149] S. K. Agarwalla, S. S. Chatterjee, and A. Palazzo, JHEP **04**, 091 (2018), 1801.04855.

[150] S. Gupta, Z. M. Matthews, P. Sharma, and A. G. Williams, Phys. Rev. D **98**(3), 035042 (2018), 1804.03361.

[151] S. Choubey, D. Dutta, and D. Pramanik, Eur. Phys. J. C **79**(11), 968 (2019), 1811.08684.

[152] A. De Gouvêa, K. J. Kelly, G. Stenico, and P. Pasquini, Phys. Rev. D **100**(1), 016004 (2019), 1904.07265.

[153] A. Ghoshal, A. Giarnetti, and D. Meloni, JHEP **12**, 126 (2019), 1906.06212.

[154] S. Kumar Agarwalla, S. S. Chatterjee, and A. Palazzo, JHEP **12**, 174 (2019), 1909.13746.

[155] R. Majhi, C. Soumya, and R. Mohanta, J. Phys. G **47**(9), 095002 (2020), 1911.10952.

[156] M. Ghosh, T. Ohlsson, and S. Rosauro-Alcaraz, JHEP **03**, 026 (2020), 1912.10010.

[157] S. S. Chatterjee and A. Palazzo (2020), 2005.10338.

[158] P. Huber, M. Lindner, and W. Winter, Nucl. Phys. **B645**, 3 (2002), hep-ph/0204352.

[159] G. L. Fogli, E. Lisi, A. Marrone, D. Montanino, and A. Palazzo, Phys. Rev. **D66**, 053010 (2002), hep-ph/0206162.

[160] M. Gonzalez-Garcia and M. Maltoni, Phys.Rev. **D70**, 033010 (2004), hep-ph/0404085.

[161] R. Gandhi, P. Ghoshal, S. Goswami, P. Mehta, S. U. Sankar, and S. Shalgar, Phys. Rev. **D76**, 073012 (2007), 0707.1723.

[162] J. Kopp, Int. J. Mod. Phys. **C19**, 523 (2008), physics/0610206.

[163] J. Kopp, M. Lindner, T. Ota, and J. Sato, Phys.Rev. **D77**, 013007 (2008), 0708.0152.

[164] P. Huber, M. Lindner, and W. Winter, Comput. Phys. Commun. **167**, 195 (2005), hep-ph/0407333.

[165] P. Huber, J. Kopp, M. Lindner, M. Rolinec, and W. Winter, Comput. Phys. Commun. **177**, 432 (2007), hep-ph/0701187.

[166] T. Alion *et al.* (DUNE) (2016), 1606.09550.

[167] M. Dentler, A. Hernández-Cabezudo, J. Kopp, P. A. Machado, M. Maltoni, I. Martinez-Soler, and T. Schwetz, JHEP **08**, 010 (2018), 1803.10661.

[168] P. Machado, H. Schulz, and J. Turner, Phys. Rev. D **102**(5), 053010 (2020), 2007.00015.

[169] M. A. Acero *et al.* (NOvA), Phys. Rev. Lett. **123**(15), 151803 (2019), 1906.04907.

[170] K. Abe *et al.* (T2K), Nature **580**(7803), 339 (2020), [Erratum: Nature 583, E16 (2020)], 1910.03887.

[171] K. Abe *et al.* (Hyper-Kamiokande Proto-), PTEP **2015**, 053C02 (2015), 1502.05199.

[172] K. Abe *et al.* (Hyper-Kamiokande) (2018), 1805.04163.

[173] C. Giunti and E. M. Zavanin, JHEP **07**, 171 (2015), 1505.00978.

[174] M. Mitra, G. Senjanovic, and F. Vissani, Nucl. Phys. **B856**, 26 (2012), 1108.0004.

[175] N. Aghanim *et al.* (Planck), Astron. Astrophys. **641**, A6 (2020), [Erratum: Astron.Astrophys. 652, C4 (2021)], 1807.06209.

[176] M. Agostini *et al.* (GERDA), Science **365**, 1445 (2019), 1909.02726.

[177] A. Meroni, S. T. Petcov, and F. Simkovic, JHEP **02**, 025 (2013), 1212.1331.

[178] S. Kovalenko, Z. Lu, and I. Schmidt, Phys. Rev. D **80**, 073014 (2009), 0907.2533.

[179] C. Alduino *et al.* (CUORE), Phys. Rev. Lett. **120**(13), 132501 (2018), 1710.07988.

[180] M. Agostini *et al.* (GERDA), Phys. Rev. Lett. **120**(13), 132503 (2018), 1803.11100.

[181] A. Gando *et al.* (KamLAND-Zen), Phys. Rev. Lett. **117**(8), 082503 (2016), [Addendum: Phys. Rev. Lett.117,no.10,109903(2016)], 1605.02889.

[182] J. T. Penedo and S. T. Petcov, Phys. Lett. **B786**, 410 (2018), 1806.03203.

[183] J. C. Pati and A. Salam, Phys. Rev. D **10**, 275 (1974), [Erratum: Phys.Rev.D 11, 703–703 (1975)].

[184] R. N. Mohapatra and J. C. Pati, Phys. Rev. D **11**, 2558 (1975).

[185] G. Senjanovic and R. N. Mohapatra, Phys. Rev. D **12**, 1502 (1975).

[186] R. N. Mohapatra and G. Senjanovic, Phys. Rev. **D23**, 165 (1981).

[187] M. Malinsky, T. Ohlsson, and H. Zhang, Phys. Rev. D **79**, 011301 (2009), 0811.3346.

[188] K. Huitu, T. J. Kärkkäinen, J. Maalampi, and S. Vihonen, Phys. Rev. D **97**(9), 095037 (2018), 1711.02971.

[189] W. Chao and H. Zhang, Phys. Rev. D **75**, 033003 (2007), hep-ph/0611323.

[190] A. Abada, C. Biggio, F. Bonnet, M. B. Gavela, and T. Hambye, JHEP **12**, 061 (2007), 0707.4058.

[191] M. Gavela, D. Hernandez, T. Ota, and W. Winter, Phys.Rev. **D79**, 013007 (2009), 0809.3451.

[192] Y. Grossman, Phys.Lett. **B359**, 141 (1995), hep-ph/9507344.

[193] T. Ohlsson, Rept. Prog. Phys. **76**, 044201 (2013), 1209.2710.

[194] P. Dunne (T2K), *Latest Neutrino Oscillation Results from T2K*, talk at Neutrino2020, July, 2020. "https://zenodo.org/record/3959558#.Y2nS8C8RppQ" (2020).

[195] K. Abe *et al.* (T2K), Nucl. Instrum. Meth. A **659**, 106 (2011), 1106.1238.

[196] K. Abe *et al.* (T2K), Nature **580**(7803), 339 (2020), [Erratum: Nature 583, E16 (2020)], 1910.03887.

[197] M. A. Acero *et al.* (NOvA), Phys. Rev. Lett. **123**(15), 151803 (2019), 1906.04907.

[198] M. A. Acero *et al.* (NOvA) (2021), 2108.08219.

[199] P. B. Denton, J. Gehrlein, and R. Pestes, Phys. Rev. Lett. **126**(5), 051801 (2021), 2008.01110.

[200] S. S. Chatterjee and A. Palazzo, Phys. Rev. Lett. **126**(5), 051802 (2021), 2008.04161.

[201] P. B. Denton, A. Giarnetti, and D. Meloni (2022), 2210.00109.

[202] B. Abi *et al.* (DUNE) (2021), 2103.04797.

[203] K. Abe *et al.* (Hyper-Kamiokande) (2018), 1805.04163.

[204] K. Abe *et al.* (Hyper-Kamiokande), PTEP **2018**(6), 063C01 (2018), 1611.06118.

[205] I. Esteban, M. C. Gonzalez-Garcia, M. Maltoni, I. Martinez-Soler, and J. Salvado, JHEP **08**, 180 (2018), [Addendum: JHEP 12, 152 (2020)], 1805.04530.

[206] G. Mitsuka *et al.* (Super-Kamiokande), Phys. Rev. D **84**, 113008 (2011), 1109.1889.

[207] K. Abe *et al.* (T2K), Phys. Rev. D **103**(11), 112008 (2021), 2101.03779.

[208] K. Abe *et al.* (Super-Kamiokande), Phys. Rev. D **91**(5), 052003 (2015), 1410.4267.

[209] M. G. Aartsen *et al.* (IceCube), Nature Phys. **14**(9), 961 (2018), 1709.03434.

[210] C. A. Argüelles, G. H. Collin, J. M. Conrad, T. Katori, and A. Kheirandish, in *7th Meeting on CPT and Lorentz Symmetry* (2017), pp. 153–156, 1608.02946.

[211] S. Kumar Agarwalla and M. Masud, Eur. Phys. J. C **80**(8), 716 (2020), 1912.13306.

[212] S. Sahoo, A. Kumar, and S. K. Agarwalla (2021), 2110.13207.

[213] A. Kostelecky and M. Mewes, Phys. Rev. D **85**, 096005 (2012), 1112.6395.

[214] G. Barenboim, M. Masud, C. A. Ternes, and M. Tórtola, Phys. Lett. B **788**, 308 (2019), 1805.11094.

[215] V. A. Kostelecky and N. Russell (2008), 0801.0287.

[216] D. Zaborov, *Scientific Potential of a neutrino beam from Protvino to ORCA (P2O)*, talk at Neutrino GDR Meeting, Paris, November 2017. "https://indico.in2p3.fr/event/16553/contributions/57491/attachments/45237/56246/P2O-zaborov-GDR-neutrino-Nov2017.pdf" (2017).

[217] D. Zaborov (KM3NeT), in *18th Lomonosov Conference on Elementary Particle Physics* (2019), pp. 53–60, 1803.08017.

[218] A. V. Akindinov *et al.*, Eur. Phys. J. C **79**(9), 758 (2019), 1902.06083.

[219] P. Coloma and P. Huber, Phys. Rev. Lett. **111**(22), 221802 (2013), 1307.1243.

[220] U. Mosel, O. Lalakulich, and K. Gallmeister, Phys. Rev. Lett. **112**, 151802 (2014), 1311.7288.

[221] L. Alvarez-Ruso, Y. Hayato, and J. Nieves, New J. Phys. **16**, 075015 (2014), 1403.2673.

[222] O. Benhar, P. Huber, C. Mariani, and D. Meloni, Phys. Rept. **700**, 1 (2017), 1501.06448.

[223] L. Alvarez-Ruso *et al.* (NuSTEC), Prog. Part. Nucl. Phys. **100**, 1 (2018), 1706.03621.

[224] S. Nagu, J. Singh, and J. Singh, Adv. High Energy Phys. **2020**, 5472713 (2020), 1906.02190.

[225] D. K. Singha, M. Ghosh, R. Majhi, and R. Mohanta, JHEP **05**, 117 (2022), 2112.04876.

[226] S. Choubey, M. Ghosh, and D. Pramanik, Eur. Phys. J. C **79**(7), 603 (2019), 1812.02608.

[227] M. Perrin-Terrin, Eur. Phys. J. C **82**(5), 465 (2022), 2112.12848.

[228] D. Kaur, N. R. K. Chowdhury, and U. Rahaman (2021), 2110.02917.

[229] S. Adrian-Martinez *et al.* (KM3Net) (2016), 1601.07459.

[230] A. Margiotta (KM3NeT), in *21st International Symposium on Very High Energy Cosmic Ray Interactions* (2022), 2208.07370.

[231] J. Brunner (P2O), *Neutrino Beam from Protvino to KM3NeT/ORCA*, contribution at European Strategy for Particle Physics (2018-2020). "https://indico.cern.ch/event/765096/contributions/3295791/attachments/1785302/2906340/Addendum_P2O.pdf" (2018).

[232] J. Brunner (P2O), *P2O Status and current results*, talk at P2O longbaseline Project, January, 2021. "https://indico.cern.ch/event/997165/contributions/4189633/attachments/2175114/3672699/Intro_210121.pdf" (2021).

[233] K. Anderson *et al.* (1998).

[234] J. A. Formaggio and G. P. Zeller, Rev. Mod. Phys. **84**, 1307 (2012), 1305.7513.

[235] N. Tagg *et al.* (MINERvA), Nucl. Instrum. Meth. A **676**, 44 (2012), 1111.5315.

[236] B. Eberly *et al.* (MINERvA), Phys. Rev. D **92**(9), 092008 (2015), 1406.6415.

[237] L. Michel, Proceedings of the Physical Society. Section A **63**(5), 514 (1950), URL https://doi.org/10.1088/0370-1298/63/5/311.

[238] P. Abratenko *et al.* (MicroBooNE), Phys. Rev. Lett. **128**(11), 111801 (2022), 2110.00409.